

Monte Carlo modelling of the patient and treatment delivery complexities for high dose rate brachytherapy

Citation for published version (APA):

Paiva Fonseca, G. (2015). *Monte Carlo modelling of the patient and treatment delivery complexities for high dose rate brachytherapy*. [Doctoral Thesis, Maastricht University]. Datawyse / Universitaire Pers Maastricht. <https://doi.org/10.26481/dis.20150924gp>

Document status and date:

Published: 01/01/2015

DOI:

[10.26481/dis.20150924gp](https://doi.org/10.26481/dis.20150924gp)

Document Version:

Publisher's PDF, also known as Version of record

Please check the document version of this publication:

- A submitted manuscript is the version of the article upon submission and before peer-review. There can be important differences between the submitted version and the official published version of record. People interested in the research are advised to contact the author for the final version of the publication, or visit the DOI to the publisher's website.
- The final author version and the galley proof are versions of the publication after peer review.
- The final published version features the final layout of the paper including the volume, issue and page numbers.

[Link to publication](#)

General rights

Copyright and moral rights for the publications made accessible in the public portal are retained by the authors and/or other copyright owners and it is a condition of accessing publications that users recognise and abide by the legal requirements associated with these rights.

- Users may download and print one copy of any publication from the public portal for the purpose of private study or research.
- You may not further distribute the material or use it for any profit-making activity or commercial gain
- You may freely distribute the URL identifying the publication in the public portal.

If the publication is distributed under the terms of Article 25fa of the Dutch Copyright Act, indicated by the "Taverne" license above, please follow below link for the End User Agreement:

www.umlib.nl/taverne-license

Take down policy

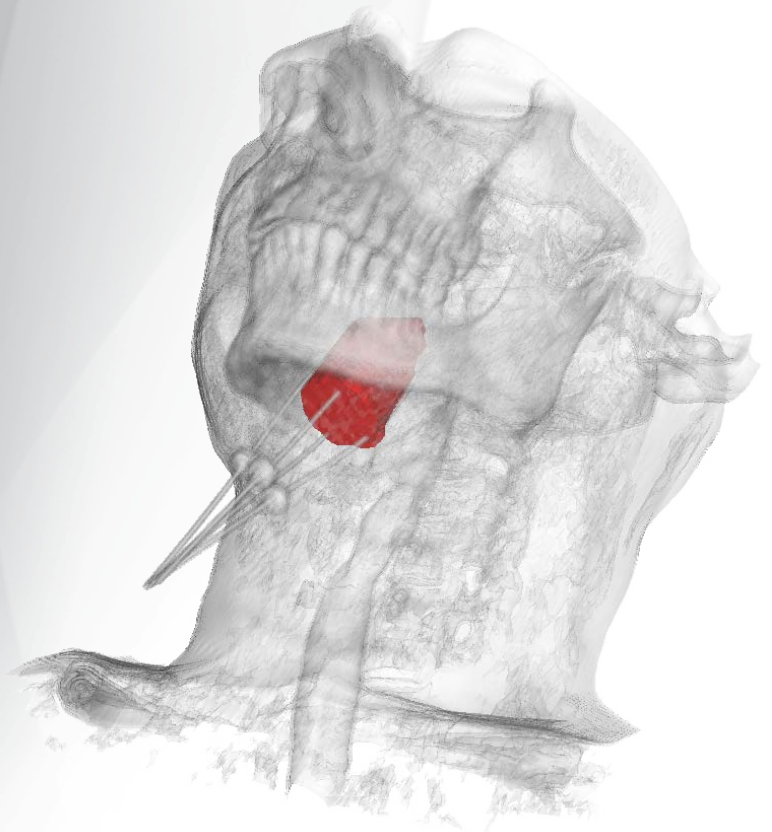
If you believe that this document breaches copyright please contact us at:

repository@maastrichtuniversity.nl

providing details and we will investigate your claim.

Monte Carlo modelling of the patient and treatment delivery complexities for high dose rate brachytherapy

Gabriel Paiva Fonseca



All rights reserved. No part of this book may be reproduced or transmitted in any form or by any means, without permission in writing, from the copyright holder.

Printing: Datawyse | Universitaire Pers Maastricht

ISBN: 978-94-6159-474-7

Monte Carlo modelling of the patient and treatment delivery complexities for high dose rate brachytherapy

Thesis

to obtain the degree of Doctor at Maastricht University,
on the authority of the Rector Magnificus, Prof.dr. L.L.G. Soete
in accordance with the decision of Board of Deans,
and the degree of Doctor at the University of São Paulo,
on the authority of the Rector Magnificus, Prof.dr. Marco Antonio Zago,
to be defended in public
on Thursday 24th of September 2015 at 10:00 hours, in Maastricht,
and on Thursday 15th of October 2015 at 14:00 hours, in São Paulo

by

Gabriel Paiva Fonseca



Supervisors

Prof. Dr. Frank Verhaegen

Prof. Dr. Hélio Yoriyaz

Co-supervisor

Dr. Brigitte Reniers

Assessment Committee – the Netherlands

Prof. Dr. Philip Lambin (chairman), Maastricht University

Prof. Dr. Dietmar Georg, Medical University Vienna

Prof. Dr. Luc Beaulieu, University Laval, Quebec City, Canada

Dr. Ans Swinnen, Maastricht Clinic

Dr. Ludy Lutgens, Maastricht Clinic

Assessment Committee – Brazil

Prof. Dr. Hélio Yoriyaz (chairman), Instituto de Pesquisas Energéticas e Nucleares

Prof. Dr. Laura Natal Rodrigues, Universidade de São Paulo

Prof. Dr. Marcelo Baptista de Freitas, Universidade Federal de São Paulo

Prof. Dr. Elisabeth Mateus Yoshimura, Universidade de São Paulo

These studies were funded by a PhD Scholarship from Fundação de Amparo a Pesquisa do Estado de São Paulo (FAPESP, SP, Brazil).

This thesis is dedicated to my beloved wife, Louise, for her support during the most difficult moments, for being part of my happiest memories and for everything that we are going to experience together.

Acknowledgments

Foremost, I would like to acknowledge my supervisors Prof. Dr. Hélio Yoriyaz, Prof. Dr. Frank Verhaegen and Dr. Brigitte Reniers for the opportunity, patience and dedication that without doubts were essential for this thesis and very important for my personal life.

Hélio, thank you for accept me as your student back in 2004, during my master and Ph.D. This experience greatly improved my formation and guided me into the scientific career. Thanks for teach and work with me (even during your holidays) and for many pleasant moments.

Frank, thank you for providing me the opportunity to study in Europe and be part of your research team. I cannot describe how fortunate I was for being so well received and how it changed my perception of the world. Many thanks for the uncountable times you had to read my papers and for always (even being the busiest person I know) find time to teach and guide me.

Brigitte, thank you for find time to contribute with this thesis, for the innumerable and productive discussions and for being available even to visit different hospitals seeking for data that were very important.

This Ph.D would not be possible without a person who was part of my professional life only for a short period, but made very important contributions suggesting the subject of my master thesis and introducing me to Frank. Thank you Dr. Esmeralda Poli.

Guillaume, Mark and Shane, work with you was very important and I owe you a lot for it.

I had a terrific experience in the Netherlands and I owe it to you guys: Shane, Mark, Aniek, Ruud, Guillaume, Sean, Patrick, Raghu, Skadi, Karen, Sara, Ralph, Stefan, Davide, Daniela, Lucas, Evelyn, Emmanuel, Isabel, Lotte, Pedro, Ruben, Jurgen and Timo. Thanks for the laughs, runs, dinner, squash games (sorry for the bruises and scars) and for all the help.

Thanks to the whole radiotherapy team in Brazil, in particular to Gabriela, Rodrigo and Camila, for the discussions and experiments late night or during the weekends. Your contribution was very important and I hope we can keep working together.

I would like to thank my colleagues and friends in Brazil for the support, laughs, barbecues and especially for all the time you kept me out of the office. It did not contribute

much with my work, but gave me a lot of pleasant moments and good memories. Thank you guys; Paula, Gregório, Arthur, Cesar, Henrique, Carlos, Tassio, Rodrigo, Felipe, Talita, Yan, Michele, Murillo.

Thank you Louise for being with me all the time since 2002 and for your importance in my life. Your determination kept me on track and helped me to pursue my goals.

Finally, I would like to thank my beloved parents, Carlos e Madalena, my brother Rodrigo and my sisters Roberta e Juliana. I am thankful for being part of this family. The distance was tough, but your strength and love allowed me to keep going.

*AMIGOBachy uses icons downloaded from www.flaticon.com and www.freepik.com (free license with attribution) and made by: Sarfraz Shoukat, Nice and serious, FreePic, Yannick, SimpleIcon, PICOL, Situ-Herrera, Vectorgraphit, Catalin Fertu, Anton Saputro, Icon Works, Pavel Kozlov and Fermam Aziz. More information are available in the software user guide.

Abstract

Brachytherapy treatments are commonly performed using the American Association of Physicists in Medicine (AAPM) Task Group report TG-43U1 absorbed dose to water formalism, which neglects human tissue densities, material compositions, body interfaces, body shape and dose perturbations from applicators. The significance of these effects has been described by the AAPM Task Group report TG-186 in published guidelines towards the implementation of Treatment Planning Systems (TPS) which can take into account the above mentioned complexities. This departure from the water kernel based dose calculation approach requires relevant scientific efforts in several fields. This thesis aims to improve brachytherapy treatment planning accuracy following TG-186 recommendations and going beyond it. A software has been developed to integrate clinical treatment plans with Monte Carlo (MC) simulations; high fidelity CAD-Mesh geometry was employed to improve brachytherapy applicators modelling; different dose report quantities, $D_{w,m}$ (dose to water in medium) and $D_{m,m}$ (dose to medium in medium), were obtained for a head and neck case using small cavity theory (SCT) and large cavity theory (LCT); the dose component due to the source moving within the patient was evaluated for gynecological and prostate clinical cases using speed profiles from the literature. Moreover, source speed measurements were performed using a high speed camera. Dose calculations using MC showed overdosing around 5% within the target volume for a gynecological case comparing results obtained including tissue, air and applicator effects against a homogeneous water phantom. On the other hand, the same comparison showed underdosing around 5% when including tissue and air composition for an interstitial arm case. A hollow cylinder applicator was responsible for the overdosing observed for the gynecological case highlighting the importance of accurate applicator modelling. The evaluated CAD-Mesh applicators models included a Fletcher-Williamson shielded applicator and a deformable balloon used for accelerated partial breast irradiation. Results obtained were equivalent to ones obtained with conventional constructive solid geometry and may be convenient for complex applicators and/or when manufacturer CAD models are available. Differences between $D_{m,m}$ and $D_{w,m}$ (SCT or LCT) are up to 14% for bone in a evaluated head and neck case. The approach (SCT or LCT) leads to differences up to 28% for bone and 36% for teeth. Differences can also be significant due to the source movement since some speed profiles from literature show low source speeds or uniform accelerated movements. Considering the worst case scenario and without include any dwell time correction, the transit dose can reach 3% of the prescribed dose in a gynecological case with 4 catheters and up to 11.1% when comparing the average prostate dose for a case with 16 catheters. The transit dose for a high speed (measured with a video camera) source is not uniformly distributed leading to over and underdosing, which is within 1.4% for commonly prescribed doses (3–10 Gy). The main subjects evaluated in this thesis are relevant for brachytherapy treatment planning and can improve treatment accuracy. Many of the issues described in here can be assessed with the software, coupled with a MC code, developed in this work.

Key words: Brachytherapy, Monte Carlo, HDR ^{192}Ir , MBDCA

Resumo

Tratamentos braquiterápicos são comumente realizados conforme o relatório da *American Association of Physicists in Medicine (AAPM), Task Group report TG-43U1*, o qual define o formalismo para cálculo de dose absorvida na água e não considera a composição dos materiais, densidades, dimensões do paciente e o efeito dos aplicadores. Estes efeitos podem ser significantes, conforme descrito pelo recente relatório da AAPM, *Task Group report TG-186*, que define diretrizes para que sistemas de planejamento modernos, capazes de considerar as complexidades descritas acima, sejam implementados. Esta tese tem como objetivo contribuir para o aumento da exatidão dos planejamentos de tratamento braquiterápicos, seguindo as recomendações do TG-186 e indo além do mesmo. Um software foi desenvolvido para integrar planejamentos de tratamento e simulações pelo método de Monte Carlo (MC); modelos acurados, CAD-Mesh, foram utilizados para representar aplicadores braquiterápicos; Grandezas utilizadas para reportar dose absorvida, $D_{w,m}$ (dose para água no meio) e $D_{m,m}$ (dose para o meio no meio), foram calculadas para um tratamento de cabeça e pescoço, considerando a teoria para pequenas (SCT – *small cavity theory*) e grandes cavidades (LCT – *large cavity theory*); a componente da dose em razão do movimento da fonte foi avaliada para tratamentos de próstata e ginecológicos. Perfis de velocidade obtidos na literatura foram utilizados; medidas de velocidade de uma fonte braquiterápica foram realizadas com uma câmera de alta taxa de aquisição. Cálculos de dose obtidos usando MC (incluindo a composição e densidade dos tecidos, ar e o aplicador) mostram sobredoses de aproximadamente 5% dentro do volume alvo, em um tratamento ginecológico, quando comparados aos resultados obtidos com um meio homogêneo de água. Por sua vez, subdoses de aproximadamente 5% foram observadas ao considerar a composição dos tecidos e regiões com ar em um tratamento intersticial de braço. Um aplicador cilíndrico oco resultou na sobredose observada no caso ginecológico, ressaltando a necessidade de modelos acurados para representar os aplicadores. Os modelos CAD-Mesh utilizados incluem um aplicador Fletcher-Williamson, com blindagem, e um balão deformável para irradiação de mama. Os resultados obtidos com estes modelos são equivalentes aos obtidos com modelos geométricos convencionais. Este recurso pode ser conveniente para aplicadores complexos e/ou quando o projeto dos aplicadores for disponibilizado pelo fabricante. Cálculos de dose, com a composição real dos tecidos humanos, podem apresentar diferenças significativas em razão da grandeza adotada. Diferenças entre $D_{m,m}$ e $D_{w,m}$ (SCT ou LCT) chegam a 14% em razão da composição do osso. A metodologia adotada (SCT ou LCT) resulta em diferenças de até 28% para o osso e 36% para os dentes. A componente de dose de trânsito também pode levar a diferenças significativas, uma vez que baixas velocidades ou movimentos uniformemente acelerados foram descritos na literatura. Considerando a pior condição e sem incluir nenhuma correção no tempo de parada, a dose de trânsito pode chegar a 3% da dose prescrita para um caso ginecológico, com 4 cateteres, e até 11.1% da dose prescrita para um tratamento de próstata, com 16 cateteres. A dose de trânsito para a fonte avaliada (velocidade obtida experimentalmente) não é uniformemente distribuída e pode levar a sub ou sobredoses de até 1.4% das doses comumente prescritas (3–10 Gy). Os tópicos estudados são relevantes para tratamentos braquiterápicos e podem contribuir para o aumento de sua acurácia. Os efeitos estudados podem ser avaliados com o uso do software, associado a um código MC, desenvolvido.

Palavras chave: Braquiterapia, Monte Carlo, HDR ^{192}Ir , MBDC

Summary

1	INTRODUCTION	3
1.1	AMIGOBrachy	4
1.2	CAD-Mesh.....	4
1.3	Dose specification	5
1.4	Transit dose.....	7
1.5	Speed Measurements.....	9
2	OBJECTIVES.....	13
3	LITERATURE REVIEW	17
3.1	Brachytherapy history and current practice	17
3.2	MC methods in brachytherapy	24
4	MATERIALS AND METHODS	29
4.1	Monte Carlo codes.....	29
4.2	AMIGOBrachy	31
4.3	CAD-Mesh.....	36
4.4	Dose specification ($D_{w,m}$ and $D_{m,m}$).....	43
4.5	Transit dose.....	45
4.6	Speed measurements	52
5	RESULTS AND DISCUSSIONS.....	57
5.1	AMIGOBrachy	57
5.2	CAD-Mesh.....	61
5.3	Dose specification	68
5.4	Transit dose.....	78
5.5	Speed measurements	85
6	CONCLUSIONS	93
7	FUTURE PERSPECTIVES.....	97

8	LIST OF PUBLICATIONS	101
8.1	Published articles.....	101
8.2	Conferences.....	102
9	CURRICULUM VITAE	105
10	REFERENCES.....	109
11	VALORIZATION ADDENDUM.....	121
11.1	Innovation	121
11.2	Clinical relevance	123
11.3	Societal relevance	123
11.4	Commercial relevance.....	124

Figure List

Figure 1. a) mass energy absorption coefficients (μ_{en}/ρ) of various human tissues relative to water coefficients. Values for elemental media obtained from NIST ³⁹ and combined into human tissues using the mass-fraction of each element. b) Unrestricted mass collision stopping power (S_{col}/ρ) ratios of various human tissues relative to those for water. Values obtained using ESTAR database considering the mass-fraction of each element. ⁴⁰	7
Figure 2. Remote afterloaders from two manufacturers: Left – microSelectron HDR (Nucletron, an Elekta company, Stockholm, Sweden); Right – GammaMed Plus iX (Varian Medical Systems, Inc., Palo Alto, CA).....	18
Figure 3. a) TRUS image of a prostate patient; b) CT image of a head and neck patient; c) MRI image of a gynecological patient; d) 3D reconstruction from CT images including the clinical target volume (CTV) in red.....	21
Figure 4. CT slices of a head and neck patient showing metal artifacts	22
Figure 5. Ratio between dose distributions obtained with MC with and without including the Fletcher Williamson applicator. The dark blue region represents the applicator.	24
Figure 6. Number of papers per year including the term ‘Monte Carlo’. Results of a PubMed search (20 January 2015).	25
Figure 7. Flowchart with AMIGOBraChy’s main functionalities, which are described in the user-guide. The process starts with importing or creating a DICOM sequence of images, followed by defining the simulation parameters and initiating MCNP6, and finishes by importing and analyzing the simulated dose distributions.....	32
Figure 8. A 180° tungsten shielded applicator modeled using: a) analytical geometry; b) (1x1x1) mm ³ voxels; c) mesh structures created with Abaqus TM . The dimensions are based on the GM11004380 applicator (Varian Medical Systems) and on the ACUROS TM applicator database.....	33
Figure 9. A sequence of images used by AMIGOBraChy: a) importing the DICOM patient CT image; b) defining structures by importing DICOM contours (e.g. the highlighted bone contours); c) defining the material map (using HU numbers or drawing tools), which consists of air (black region), adipose tissue (blue region), muscle (green region) and bone (yellow region); d) defining the voxel phantom region (external rectangle) and the dose scoring region (internal rectangle).....	35
Figure 10. Example MG for the idealized APBI applicator showing the external surface and an inner section using a cutaway plane. The wall material is barium loaded polymer.....	38

Figure 11. a) Axial CT image of an APBI balloon applicator inserted in a post surgical breast cavity. The wall is clearly visible due to barium loading. The EBS channel is occupied by a dummy insert to identify dwell positions. The balloon is filled with a saline solution. The high intensity pixels correspond to the end cap. Neither saline solution nor end cap are modeled in this thesis. b) MG for the APBI applicator showing the external surface.	39
Figure 12. Schematic representation of the shielded cylindrical vaginal applicator.	40
Figure 13. CAD representation of the Fletcher Williamson applicator (from Abaqus TM).	41
Figure 14. Axial and sagittal view of the evaluated head and neck clinical case. The numbers indicate voxels positions where the photon spectrum was scored. Green arrows and squares were added to show the catheter positions (five of the six catheters can be visualized).	43
Figure 15. a) Source moving between three dwell positions with inter-dwell distance of 0.5 cm. b) Source speed profile for a uniform accelerated movement. c) Contribution of each source position to transit dose at the reference point due the source traveling between the dwell positions and returning to the safe.	48
Figure 16. Experimental setup for source speed measurements. The insert (top-right) was obtained from one of the acquired slow motion videos. The source guide was positioned to be clinically relevant avoiding excessive bending during the experiments.	52
Figure 17. AMIGOBrachy screenshots of a) AMIGOBrachy ImageView module; b) 3D rendering of lungs; c) dose distribution of a single source dwell position with dose profiles; d) dose distribution obtained using a titanium fletcher applicator and a sequence of source dwell positions.	57
Figure 18. Results for the two patient geometries: the intracavitary gynecological case (left panels) and the interstitial arm case (right panels). a) 3D view indicating the assigned materials. b) Isodoses and dose ratio ACUROS TM /MCNP6. c) Isodoses and dose ratio MCNP6(homogeneous water)/MCNP6(heterogeneous geometry).	60
Figure 19. Calculation times in seconds for simulating 10^7 primary photons from an ^{192}Ir source in a water cube represented by a MG with varying number of volume elements.	62
Figure 20. (a) Inside the balloon wall there appears to be a lack of backscatter from the balloon wall and the water beyond it in the MG case. (b) However, the photon spectra directly outside the balloon agree between MG and CSG.	62
Figure 21. a) Dose ratio in an axial slice intersecting the origin from dose distributions obtained with MG and CSG representations of the idealized APBI balloon applicator using Geant4 and a 50 kV photon spectrum. Isodose lines are also presented. b) Dose ratio obtained using MG in Geant4 and MCNP6. Dose in the balloon wall was not scored in Geant4 hence	

the low values of the ratio. Isodoses overlap for (a) and (b) due to the small differences obtained. The first two colour maps show a histogram (black) of the distribution of values of the dose ratio over the whole phantom volume.	63
Figure 22. a) The MG of the irregular balloon. b) Axial plot of dose ratios obtained from MCNP6 and Geant4 using the MG of the balloon and a 50 kV photon point source. Isodose lines are also presented. Dose in the balloon wall was not scored in Geant4 hence the low values of the ratio. The color map shows a histogram (extreme right) of the dose ratio distribution over the whole phantom volume.	64
Figure 23. a) APBI balloon applicator wall represented by voxels. b) Axial dose ratio obtained from MCNP6 using the voxel and MG models of the balloon.	64
Figure 24. a) Dose ratio in central axial, coronal and sagittal slices from Geant4 and MCNP calculations of the dose distribution from the shielded HDR vaginal applicator represented with MG containing 16530 elements. b) The dose ratio when representing the applicator with a MG of 16530 elements in MCNP and a CSG representation. Differences are not visible in these figures (b) since most of the results are within 0.5% with maximum difference around 1%. c) Dose ratio between MG and CSG applicator models in MCNP using 129860 elements for the MG. Isodoses inside of the applicator were not shown.....	66
Figure 25. Calculation times in seconds for 10^7 primary photons from an ^{192}Ir source with the W shield from the vaginal applicator represented by a MG with varying number of volume elements.	67
Figure 26. Dose ratios between Geant4 and MCNP6, using MG models. a) Axial slice. b) Sagittal slice of the dose ratio. c) Coronal slice. Isodose lines from both codes are also plotted.	67
Figure 27. a) MG representation of the shielded Fletcher Williamson applicator used for validation purposes. The MG geometry was exported by MCNP6 as an output file ¹¹⁷ . Ratio between MCNP6 (CSG) and Geant4 (MG): b) sagittal slice of the dose ratio; c) axial slice; d) coronal slice.	68
Figure 28. Axial (a) and sagittal (b) spatial distribution of the mean photon energy distribution for the evaluated head and neck case and mean energy–volume histograms (c) for all voxels scored over the whole CT volume, excluding air voxels. Uncertainty <4% for all voxels (Type A $\pm 1\sigma$).	69
Figure 29. Axial and sagittal view of the mean photon energy ratio: a) phantom II over phantom I. This shows the density effect since both phantoms consist of only water; b) phantom III over phantom II. This shows the composition effect since all voxels have the	

same mass densities; c) phantom III over phantom I. This shows the atomic number and density effects that approximately compensate each other. Contours in black represent bone tissue.	69
Figure 30. a) Photon spectrum emitted from the stainless steel capsule (averaged over all angles of a single source) and at two evaluated voxels, P9 and P13. Values were normalized for the total fluence in their respective voxel and grouped using 5 keV energy bins. Most of the photons from the source are concentrated on the peaks of the spectrum that represent the primary photons. Only values between 0 and 600 keV were displayed to highlight differences in this region.	70
Figure 31. Ratio ($D_{m,m} / D_{w,m}(LCT)$) obtained using a track length estimator tally. Uncertainty <1% for all points inside of the CT volume (Type A $\pm 1\sigma$). Regions with air were excluded. .	72
Figure 32. Ratio between $D_{m,m}$ and $D_{w,m}(LCT)$ values presented in table 2. Values obtained using SCT, dotted lines, were added.	74
Figure 33. Contribution of various parts of the photon spectrum to the total dose at two evaluated voxels, P9 and P13. Photons with energies greater than 650 keV contribute less than 0.3% of the total dose. Uncertainty <1% for the total dose (Type A $\pm 1\sigma$).	75
Figure 34. Ratio between conversion coefficients ($D_{w,m}(LCT) / D_{w,m}(SCT)$). Uncertainty <1% for all points inside of the CT volume (Type A $\pm 1\sigma$).	77
Figure 35. a) Source instantaneous speed, derived from the source trajectory and dwell positions, for each discrete source position compared against analytical calculation for the source approaching the first dwell position at 5 cm and moving between the dwell positions (right to left) up to the last dwell position that was defined as the origin; b) instantaneous speed validation for the source coming back to the safe; c) BrachyVision™ ring applicator showing the dwell positions (black boxes) superimposed over a transit dose distribution without the dwell dose component.	79
Figure 36. Gynecological case b (transverse plane): a) isodoses obtained considering the dwell dose and the total dose, which corresponds to the transit dose added to the dwell dose distribution; b) transit dose component as a percentage of the dwell dose without dwell time corrections. The dose inside of the applicator (black circle) was not scored.	80
Figure 37. Prostate case c (transverse plane): a) isodoses in a CT slice with source catheters indicated as black holes and with the prostate contour approximately equal to the innermost isodose contour; b) the ratio in percentage between the transit dose and the dwell dose; c) the ratio in percentage between the corrected transit dose and the dwell dose. Figures b and c are shown using different scales.	81

Figure 38. Prostate case d (transverse plane): a) Isodoses over a CT slice with the catheters corresponding to the boundaries of the prostate contour; b) transit dose percentage compared against the dwell dose. c) corrected transit dose percentage compared against the dwell dose. Figures b and c are shown using different scales.82

Figure 39. **a)** Source speed profile for the source arriving at the first dwell position (0 cm) and returning to the safe. Uncertainties Type A and Type B are almost equivalent so only Type B component is shown. **b)** $v_{0.2}$ values were obtained for six dwell positions equally spaced between 0 and 5 cm (vertical dotted lines). **c)** $v_{0.2}$ values were obtained for the source movement between two dwell positions, at 0 cm and 5 cm. Figures **b** and **c** use the same notation with Type A and Type B uncertainty components indicated. The source speeds at the dwell positions were not considered, therefore figures do not show speed values equal to zero.87

Figure 40. Transit dose components (**top**) for a case with six dwell positions equally spaced between 0 and 5 cm (**a**) and for a case with two dwell positions (**b**), at 0 cm and 5 cm. The dose reduction (dwell dose correction) applied to compensate the transit dose and the corrected dose are shown for both cases (**bottom**). Dwell positions are indicated with vertical dotted lines.88

Table List

Table 1. Average source speed between dwell positions for various inter-dwell distances (<i>did</i>) reported in the literature for afterloaders from Nucletron (microSelectron), Varian (GammaMed Plus) and for Eckert & Ziegler BEBIG GmbH MultiSource (^{192}Ir HDR).....	8
Table 2. Material properties of the steel channel and tungsten shield of the shielded vaginal applicator (see Figure 12). Elemental composition expressed in percentage of weight (%w). 40	
Table 3. The conversion coefficients from $D_{m,m}$ to $D_{w,m}$ (SCT) obtained using average mass stopping power ratios for some materials evaluated in this study.	72
Table 4. Ratio between $D_{m,m}$ and $D_{w,m}$ (LCT) obtained with the photon spectrum and with the mean photon energy scored (phantom III) for the 25 evaluated voxels (Figure 14). The minimum and the maximum values of each column are underscored. Mandible corresponds to mandible spongiosa from ICRP Report 110 ¹²⁹ . Uncertainty is <1% for all dose ratios (Type A $\pm 1\sigma$). $D_{m/w}$ indicates $D_{m,m}/D_{w,m}$ -LCT.	73
Table 5. Transit dose for a reference point orthogonal to the catheter's longitudinal axis and positioned at 0.5 cm from its center (Figure 15.a). The values were calculated analytically (An) and simulated (MC) extracting the information from a treatment plan created with BrachyVision TM . The underlined speeds were obtained considering a uniform accelerated movement for an acceleration of 113 cm/s^2 (Nucletron) and 55 cm/s^2 (Varian).....	79
Table 6. Transit dose component for the studied cases considering speed profiles based on literature data in absolute dose and in percentage of the dwell dose. The average speed of 2.7 cm/s (gynecological cases) and 3.8 cm/s (prostate cases) were obtained with an acceleration of 113 cm/s^2 for an inter-dwell distance of 2.5 mm (gynecological cases) and 5 mm (prostate cases).....	83
Table 7. Transit time for the studied cases considering a uniform acceleration of $ a = 77 \text{ cm/s}^2$ including the time correction applied. The mean transit dose was obtained considering the whole CT volume.....	83
Table 8. Average source speed over the inter-dwell length for inter-dwell distances of 0.25, 0.50, 1.00, 2.50 and 5.00 cm. Uncertainty values were not available for all the references. All the values were obtained for a Nucletron afterloader (Elekta Brachytherapy, Veenendaal, the Netherlands), however, the model may change.	86

LIST OF ABBREVIATIONS

ACE	Advanced Calculation Engine
AMIGOBBrachy	A Medical Image-based Graphical platfOrm - Brachytherapy module
APBI	Accelerated Partial Breast Irradiation
AAPM	American Association of Physicists in Medicine
CAD	Computer-Aided Design
CSG	Constructive Solid Geometry
CT	Computed Tomography
CPE	Charged Particle Equilibrium
$D_{w,w}$	Dose to water in water
$D_{m,m}$	Dose to medium in medium
$D_{w,m}$	Dose to water in medium
$D_{n,m}$	Dose to a cell nuclei in medium
DE/DF	Dose Energy/Dose Function MCNP cards used to define mass-energy absorption coefficients
EBRT	External Beam Radiotherapy
EBS	Electronic Brachytherapy Source
EGS	Electron Gamma Shower
F4/F6	MCNP cards to define a track length tally
GATE	Geant4 Application for Tomographic Emission
GEANT	GEometry ANd Tracking
HDR	High dose rate
LBTE	Linear Boltzmann Transport Equation
LCT	Large Cavity Theory
LDR	Low Dose Rate

MBDCA	Model-Based Dose Calculation Algorithms
MC	Monte Carlo
MCNP	Monte Carlo N-Particle
MG	Mesh Geometry
MOSFET	Metal Oxide Semiconductor Field Effect Transistor
MRI	Magnetic Resonance Imaging
PENELOPE	Penetration and ENergy LOss of Positrons and Electrons
QA	Quality Assurance
SCT	Small cavity theory
SPDTL	MCNP card to use lattice speed tally enhancement
TG	Task Group
TLD	Thermoluminescent Dosimeter
TPS	Treatment Planning System
TRUS	TransRectal UltraSound

INTRODUCTION

Chapter 1

1 INTRODUCTION

Brachytherapy treatments are commonly performed using the American Association of Physicists in Medicine (AAPM) Task Group report TG-43U1^{1, 2} absorbed dose to water formalism, which neglects human tissue densities, material compositions, body interfaces, body shape and dose perturbations from applicators. These effects can be significant^{3, 4} in the brachytherapy photon energy range and can be included in modern treatment planning systems (TPS) for brachytherapy by using model-based dose calculation algorithms (MBDCA). This new approach is needed to replace the TG-43U1 absorbed dose to water formalism with a more accurate dose estimation procedure.

The AAPM Task Group report TG-186⁵ recently issued guidelines towards implementing TPS, which can take the above mentioned complexities into account. The report recommends performing model based dose calculations such as the ones based on Monte Carlo (MC) simulations,⁶⁻⁸ finite element modelling⁹⁻¹¹ or collapsed cone convolution.¹²⁻¹⁵ This departure from the water kernel based dose calculation approach entails adequate modelling of applicators employed in source delivery for brachytherapy for both low energy (<50 keV) and high energy (>50 keV) photon sources.

TG-186 describes several areas where relevant scientific efforts are necessary to move towards MBDCA. This thesis comprehends some of these subjects and other issues relevant for brachytherapy. ¹⁹²Ir High Dose Rate (HDR) treatments are the most relevant, but not exclusive, subject of this study, which comprehends five main approaches: a) development of a MBDCA algorithm as an auxiliary software to process treatment planning data, AMIGOBachy (A Medical Image-based Graphical platfOrm - Brachytherapy module);⁶ b) the use of high fidelity CAD (Computer Aided Design)-Mesh geometry to improve brachytherapy applicators modeling;¹⁶ c) study of different dose report quantities;⁵ d) evaluation of the transit dose component for gynecological and prostate clinical cases using speed profiles from the literature;¹⁷ e) measurement of the source speed using a high speed camera since potentially relevant transit dose components were obtained using speed profiles from literature.

The subjects mentioned above are part of an effort to improve brachytherapy treatment planning accuracy following TG-186 guidelines and going beyond it since CAD-Mesh geometry and transit dose components were not discussed in TG-186. A brief introduction on each subject was written separately in the following items for clarity.

1.1 AMIGOBrachy

Several MBDCA software packages have been developed; two commercial TPS, ACUROS™ (Transpire Inc., Gig Harbor, WA)^{10, 11, 18} and the Advanced Calculation Engine (ACE) (Nucletron – an Elekta Company, Veenendaal, the Netherlands),^{12, 14, 15, 19} and several in-house MC based algorithms.^{6, 20, 21} Some MBDCA employ MC simulation codes, which offer a high accuracy for dose calculations. However, most MC codes lack a user-friendly interface to process the input and output data of brachytherapy dose calculations. This may involve several medical images, imaging artifact corrections, up to hundreds of dwell positions, and source and applicator geometries.

AMIGOBrachy⁶ is a software module developed using MATLAB version 8.0 (Mathworks Inc., Natick, MA) to create an efficient and powerful user-friendly graphical interface, needed to integrate clinical treatment plans with MC simulations. It does this by providing the main resources required to process and edit images, import and edit treatment plans, set MC simulation parameters, run MC simulations and analyze the results. In the current implementation, the MCNP6 (Monte Carlo N-Particle version 6)²² MC code is used for the simulations. AMIGOBrachy's design, main functionalities and the validation process were described including two clinical cases; one intracavitary gynecological case and one interstitial arm sarcoma case, both treated with an ¹⁹²Ir source.

1.2 CAD-Mesh

The modelling of complex brachytherapy applicators can be suboptimal when using a voxel based geometry due to the sub-voxel dimensions of specific components. This may lead to volume averaging of the details of the geometry in coarse voxels, and may therefore lead to dose calculation errors propagating in the whole geometry. The combination of a voxelized Cartesian grid (representing the Computed Tomography (CT) derived patient geometry) and constructive solid geometry (CSG) describing the applicator allows applicator modelling. However, applicator modelling using CSG can be tedious, may not allow complete fidelity or may be highly impractical, as in the case of deformable balloon applicators employed in accelerated partial breast irradiation (APBI).

The use of tessellated surfaces, defined by a collection of 2D tiles (e.g. triangular) of varying dimensions, or tessellated volumes defined by a collection of varying 3D elements (polyhedrons) can be used to describe complex geometrical shapes and offers an alternative to CSG modelling. This is especially attractive when manufacturer CAD designs are

available. This methodology has been employed by commercial deterministic particle transport software capable of handling mesh geometries (MG).^{9, 11} Recent versions of general purpose MC codes have the ability to simulate radiation transport in tessellated or MG, thus potentially facilitating the modelling of complex brachytherapy applicators.

MG modelling was evaluated by comparison to CSG modelling of a selection of brachytherapy applicators: the Fletcher Williamson gynecological ¹⁹²Ir HDR brachytherapy applicator, successfully modelled using CSG techniques by several groups,^{18, 23-27} a shielded vaginal HDR applicator and an accelerated partial breast irradiation (APBI) balloon applicator used with a 50 kV electronic brachytherapy source (EBS). Dose distributions were obtained using the Geant4²⁸ and MCNP6²⁹ general purpose MC codes.

1.3 Dose specification

TG186⁵ provides guidelines to take patient and applicator non-water materials into account and also describes the different dose reporting quantities possible; dose to medium in medium ($D_{m,m}$), and dose to water in medium ($D_{w,m}$). Differences between dose reporting in terms of $D_{m,m}$ and $D_{w,m}$ have been discussed in the literature^{5, 30, 31} with arguments in favor and against both quantities.

The way to define $D_{w,m}$ depends on assumptions in the employed cavity theory regarding the cavity dimensions compared to the ranges of secondary electrons. Absorbed dose can be calculated to a small water cavity of cellular dimensions or to a large water cavity of dimensions similar to the CT defined voxels used in MBDC treatment planning. Large Cavity Theory (LCT) uses the ratio of mass-energy absorption coefficients (water/medium), $(\mu_{en}/\rho)_w^m$, assuming charged particle equilibrium (CPE) for the cavity of interest^{32, 33}. Small Cavity Theory (SCT) uses the ratio between mass stopping power (water/medium), $(S/\rho)_w^m$, for Bragg-Gray cavities with dimensions much smaller than the secondary electron ranges.^{5, 34}

In external beam radiotherapy (EBRT), where ranges of secondary electrons are substantially longer than in brachytherapy, the cavity has been assumed to be small and conversion between $D_{m,m}$ and $D_{w,m}$ is made through ratios of unrestricted mass collision stopping power, water to medium^{30, 31, 35}. To define a cavity as small, large or even intermediate sized becomes complex in brachytherapy as ranges of secondary electrons from low energy photons (< 50 keV) are comparable to the cellular dimensions (few μm).⁵

Carlsson Tedgren and Alm Carlsson evaluated, using the Burlin theory, when cavity dimensions ranging from 1 nm to 10 μm could be assumed large, small or intermediate at various photon energies of relevance to brachytherapy. Assumed dimensions water cavity could be of interest to evaluate the correlation between dose reporting quantities and biological effects.^{34, 36} Lindborg et al. recently found the clinical radiobiological effect (RBE) for radiotherapy modalities ranging from kV x-rays to protons and heavier ions to correlate with the microdosimetric quantity mean linear energy when the latter was evaluated in volumes of nm dimensions.³⁷ The reporting dose quantities for a cell nucleus ($D_{n,m}$) of μm dimension, $D_{w,m}$ and $D_{m,m}$ were evaluated by Enger et al. for different cell nucleus compositions.³⁸

TG-186 recommends that $D_{m,m}$ should always be reported and states that more studies are necessary on how to calculate $D_{w,m}$ before any definitive recommendation can be made as to which quantity is optimal. Differences between the quantities $D_{m,m}$ and $D_{w,m}$ (LCT) are considerably smaller for the ^{192}Ir spectrum than for low photon energy (<50 keV) isotopes due to its relatively high photon energies (initial mean energy \approx 355 keV). Figure 1.a shows how ratios of mass-energy absorption coefficients (μ_{en}/ρ) between tissues and water increase at lower photon energies. However, as the photon spectrum changes away from the implanted sources due to the combined effect of attenuation of primary- and buildup of scattered-photons, larger differences between $D_{m,m}$ and $D_{w,m}$ (LCT) should occur also around an ^{192}Ir implant. Differences between $D_{m,m}$ and $D_{w,m}$ (SCT) are likely to be much less relevant since ratios of mass collision stopping powers $(S_{col}/\rho)_w^m$ are approximately independent of the energy (see Figure 1.b).

The study evaluates $D_{w,m}$ values obtained using SCT and LCT in a head and neck patient treated with HDR (high dose rate) ^{192}Ir . The head and neck case was selected due to the presence of air, soft tissues and bone interfaces. The photon spectrum and dose reporting approaches in various locations in and outside of the brachytherapy implant was studied in detail.

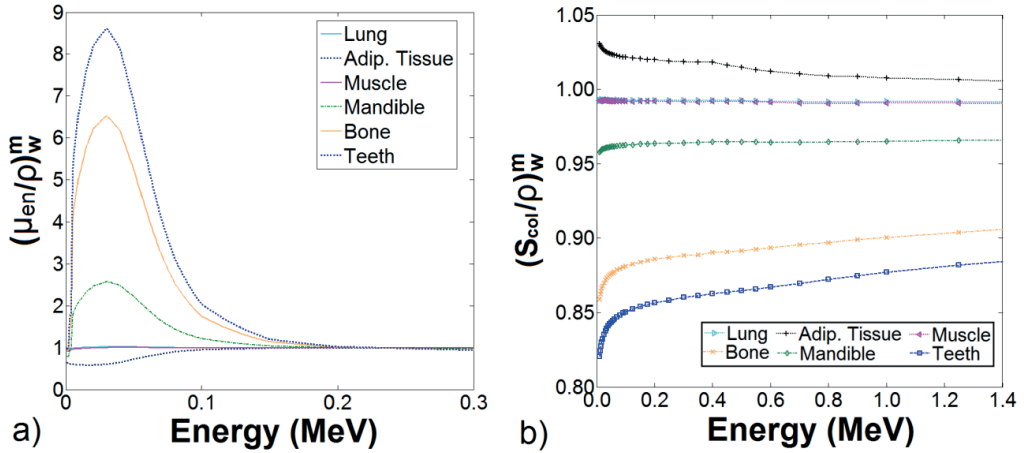


Figure 1. a) mass energy absorption coefficients (μ_{en}/ρ) of various human tissues relative to water coefficients. Values for elemental media obtained from NIST³⁹ and combined into human tissues using the mass-fraction of each element. b) Unrestricted mass collision stopping power (S_{col}/ρ) ratios of various human tissues relative to those for water. Values obtained using ESTAR database considering the mass-fraction of each element.⁴⁰

1.4 Transit dose

The transit dose component can be relevant due to the source slowing down near the dwell positions and should be considered, especially for sources with high air-kerma strengths where transit times are relatively long when compared to dwell times, and for treatments with several dwell positions and catheters where the source spends a significant amount of time in transit.⁴¹

The adopted methodology uses the information extracted from the treatment plan to define the source trajectory creating a continuous source distribution where the sampling probability at each position was weighted by the source speed extracted from the literature.^{41,42,17,43}

The instantaneous or even the average source speed measurement is a relevant issue since this parameter is not well known with reported differences up to a factor 10 depending on the measurement methodology. Table 1 presents an overview of the literature data with results obtained using a video camera,^{44,42} ionization chamber,⁴⁵ optical fibers to detect Cerenkov induced effect,⁴⁶ film analysis,⁴³ and also manufacturer information without describing the adopted methodology.⁴⁷ Three of those studies found that the source follows a

uniformly accelerated movement for the Nucletron afterloader with different accelerations reported $|a| = 113 \text{ cm/s}^2$ (Ref. 8) and $|a| = 78 \text{ cm/s}^2$ (Ref. 43); for the Varian afterloader $|a| = 55 \text{ cm/s}^2$ (Ref. 43), and for the Eckert & Ziegler BEBIG GmbH MultiSource (^{192}Ir HDR) afterloader $|a| = 77 \text{ cm/s}^2$ (Ref. 42).

Table 1. Average source speed between dwell positions for various inter-dwell distances (d_{id}) reported in the literature for afterloaders from Nucletron (microSelectron), Varian (GammaMed Plus) and for Eckert & Ziegler BEBIG GmbH MultiSource (^{192}Ir HDR).

d_{id} (cm)	Average Source speed (cm/s)							
	Nucletron – microSelectron						Varian GammaMed Plus	BEBIG ^{192}Ir HDR
	Wong ⁴⁴	Sahoo ⁴⁵	Bastin ⁴⁷	Houdek ¹⁴⁵	*Minamisawa ⁴⁶	*Wojcicka ⁴³	Wojcicka*	Palmer*
0.25	5.4	-	23.0	22.7	2.7	2.2	1.9	2.2
0.50	7.2	33.3	25.5	27.1	3.8	3.1	2.6	3.1
1.00	23.3	50.0	30.5	30.3	5.3	4.4	3.7	4.4
2.00	-	80.0	-	-	7.5	6.2	5.2	6.2
3.00	-	60.0	-	-	9.2	7.6	6.4	7.6
4.00	-	42.1	-	-	10.6	8.8	7.4	8.8

*values calculated using the uniform acceleration approach.

Most of the measured results do not agree with the manufacturer's specifications since most of the data provided by the manufacturers refers to the source moving from the afterloader to the first dwell position and returning back to it from the last dwell position, which may not represent the source speed between the dwell positions. Nucletron, Varian and BEBIG quote average speeds of 50 cm/s, 60 cm/s and 30 cm/s, respectively.⁴⁸ Differences in the speed profile can lead to significant differences in the transit dose component, which were evaluated for four clinical cases from three different centers simulated using a general multipurpose MC code, MCNP5 (Monte Carlo N-Particle Transport code, version 5).⁴⁹ Two prostate and two gynecological cases were evaluated to provide a general overview.

Although MBDCAs have a more accurate dose calculation engine than the currently available water-based TG43-U1 based TPS they do not include the transit dose component due to the source travel.

1.5 Speed Measurements

As mentioned above the transit dose component of a brachytherapy source has been studied previously,⁴¹⁻⁴⁷ reporting differences up to a factor of 10 for the source speed for the same afterloader.⁵⁰ These results indicate the importance of performing more accurate source speed profile measurements. In this work speed profiles were obtained using a high speed video camera capable of record up to 960 fps.⁵¹ Transit dose distributions and dose reductions due to dwell time corrections applied by the afterloader were calculated using MCNP6.²²

OBJECTIVES

Chapter 2

2 OBJECTIVES

The main objective of this study is to improve the accuracy of brachytherapy treatment planning and contribute to the development of this field. It was divided in specific objectives according to the five main subjects mentioned above:

- To create an auxiliary software to process treatments plans and perform MC simulations;
- To evaluate a high fidelity CAD-mesh feature for brachytherapy applicators modelling;
- To study dose report quantities, $D_{w,m}$ and $D_{m,m}$, for brachytherapy treatments;
- To take into account the transit dose component due to the source movement inside the patient using source speed profiles from the literature;
- To perform accurate source speed measurements.

LITERATURE REVIEW

Chapter 3

3 LITERATURE REVIEW

This section briefly describes the development history of brachytherapy and treatment planning status including the current status. HDR ^{192}Ir treatments and MC methods in brachytherapy are the main subjects of this thesis and are described in more detail.

3.1 Brachytherapy history and current practice

The use of radiation for treatment and diagnosis started shortly following two discoveries. X rays, discovered by Wilhelm Röntgen (1885), and radioactivity discovered by Becquerel (1896). The work of Pierre and Marie Curie (1896) identified new radioactive elements isolating radioactive samples 900 times more active than ordinary uranium. The potential for medical applications was noticed from the very beginning. Röntgen introduced his hand between an X ray source and a screen covered with fluorescent material that showed a contrast between opaque bone and translucent tissue. Becquerel also experienced and described the effects of radiation on his own skin after carrying a tube with radium in his pocket.^{13, 52}

The first reported medical experience dates from 1901 and has been followed by several studies.⁵³⁻⁵⁵ Brachytherapy treatments were performed using ^{226}Ra with first uterine cervix irradiation reported in 1903.^{54, 56, 57} The first reported cure with a patient alive and well after 8 years was published in 1913.⁵⁸ Although successfully adopted for some patients, complications were common and results depended on medical experience.⁵⁷

Brachytherapy has been under continuous development for more than a century since the first treatment. Considerable improvements were made after the discovery of artificial radioactivity in 1934 allowing the production and use of several new radionuclides like ^{60}Co , ^{137}Cs and ^{198}Au . In addition, the development of remote afterloaders in the 50's and 60's reduced the exposure of medical staff to radiation, gave more flexibility to the treatments and allowed the use of radionuclides with relative short half-life. ^{60}Co has a half-life of 5.26 years and was used for temporary implants adjusting the exposure to compensate for the radioactivity decay. Low dose rate (LDR) ^{192}Ir sources were probably introduced in 1956 by Henschke^{59, 60} as previous reports did not mention it.^{61, 62} The high specific activity of ^{192}Ir led to the development of sources with diameter of 1.1 mm or less allowing interstitial treatments and leading to the first single-step remote afterloader (1977) with a HDR ^{192}Ir source.⁶² Therefore afterloaders that were capable of only introducing and removing the

source incorporated the capability of control dwell positions and dwell times allowing patient specific dose optimization, which still is a relevant scientific topic today.⁶³⁻⁶⁵

Technical and scientific improvements reduced the treatment cost, time (for HDR treatments) and protected medical staff from radiation exposure. These reasons contributed to more positive outcome and have led to a continuously increasing number of brachytherapy treatments including cervix, lung, prostate, head and neck and other types of cancer.⁶⁶ Most of the HDR treatments nowadays are performed using ^{192}Ir sources, although new ^{69}Yb and ^{60}Co are commercially available.^{67, 68} Two modern HDR ^{192}Ir afterloaders are shown in Figure 2.



Figure 2. Remote afterloaders from two manufacturers: **Left** – microSelectron HDR (Nucletron, an Elekta company, Stockholm, Sweden); **Right** – GammaMed Plus iX (Varian Medical Systems, Inc., Palo Alto, CA).

3.1.1 Treatment planning and dosimetry

Several methods have been developed to calculate treatment doses. Intracavitary gynecological treatments used radium equivalent dosimetry (mg.Ra.h) as standard for decades.^{13, 57} Interstitial treatments were performed using few methods; Patterson–Parker dosimetry system (Manchester) defined a uniform dose, within $\pm 10\%$ of the prescribed dose, over the tumor obtained with higher concentration of source strength in the periphery.^{69, 70} The Quimby system used a uniform distribution of source strength obtaining a non-uniform dose distribution.⁶⁹⁻⁷¹ The Paris system was developed for single and double plane implants for which sources must be linear, implants should be parallel, source centers within the same plane and other geometric requirements.⁷⁰ Application time and treatment data were obtained from tables calculated for standard implants, which could differ from actual patient implants.¹³ Dose calculation formalisms from ²²⁶Ra equivalent dosimetry, point source approximations, Sieverts integration and the current formalism were summarized by Rivard et al.¹³ and described in detail elsewhere.^{1, 2, 72, 73} For brevity, only the current approach defined by the APPM TG-43U1 is described here.^{1,2}

TG-43¹ was released in 1995 and its update² in 2004; this formalism is used by commercial TPSs to calculate dose distributions through the superposition of a single dose distribution obtained for one source. The TG-43U1 dose to water formalism requires point sources or sources with cylindrical symmetry. Therefore, dose rate can be obtained $\dot{D}(r)$ with the general (2D) formalism:

$$\dot{D}(r) = S_K \cdot \Lambda \cdot \left(\frac{G_L(r, \theta)}{G_L(r_0, \theta_0)} \right)^2 \cdot g_L(r) \cdot F(r, \theta) \quad 1$$

The polar coordinate system (r and θ) was adopted along the source longitudinal axis with the origin of the coordinate system at the center of the active core. S_K is the air kerma strength (m.Gy.m².h⁻¹ (U)) of each source defined as the air kerma rate multiplied by the square of the distance.⁷⁴ The dose ratio constant, Λ , is defined as the ratio between dose rate at the reference point ($\dot{D}(r_0, \theta_0)$; $r_0 = 1$ cm and $\theta_0 = 90^\circ$) and S_K . The geometry function, $G_L(r, \theta)$, corrects the square-law based on approximate models of the source active core (point and linear sources). The radial function, $g_L(r)$, accounts for dose fall-off on the transverse-plane due to photon scattering and attenuation. The anisotropy function, $F(r, \theta)$, describes the variation in dose as a function of polar angle relative to the transverse plane.

TG-43U1 parameters have been extensively described in the literature for several brachytherapy sources.⁷⁵⁻⁷⁷ The simplistic approach and tabulated parameters allow short calculation times leading to a successful clinical implementation. Although largely employed, the dose to water formalism fails to consider the body dimensions, lack of backscattering, applicator effects and inter-seed attenuation.^{5, 13}

3.1.1.1 *TG-43U1 limitations and TG-186*

Some of TG-43U1 limitations are well known, however the scientific and technical challenges to move towards approaches that are more accurate, as MBDCAs, are significant. TG-186 describes some of TG-43U1 limitations, the status of scientific development and areas where efforts are necessary. The recent protocol was released during a period when a commercial MBDCAs was available, ACUROSTM.^{10, 11, 18} Currently, Advanced Calculation Engine (ACE) (Nucletron – an Elekta Company, Veenendaal, the Netherlands),^{12, 14, 15, 19, 78} is also available. Therefore, issues such as tissue segmentation, CT scanner calibration, dose report quantities, applicator models and other issues related to MBDCAs, which can affect brachytherapy treatments, became relevant for the medical staff and can affect brachytherapy treatments.

A discussion about some of TG-186 main subjects is included below. Dose report quantities ($D_{w,m}$ and $D_{m,m}$), widely described in TG-186, are discussed in section 1.3 (Dose specification) as it is one of the main topics of this thesis. Transit dose component (section 1.4 - Transit dose) and mesh geometries (section 1.2 - CAD-Mesh) are discussed in a different section for the same reason.

3.1.1.1.1 *Medical images and segmentation*

Brachytherapy treatments involved palpation or visualization of the structures with implant reconstruction obtained using orthogonal x rays, which did not allow anatomy based treatment planning. Therefore, treatments were performed using the applicator as reference and not the patient.^{13, 66, 79} 3D image guided implants and post implant dose calculation started with pioneering studies during 80's and 90's. The first reported use of a transrectal ultrasound (TRUS) dates from 1983 followed by several studies that consolidated this methodology.⁷⁹⁻⁸² Nowadays, TRUS, CT and magnetic resonance imaging (MRI) are commonly used for real time imaging (TRUS) and treatment planning. Medical images obtained with TRUS, CT and MRI and a 3D reconstruction are shown in Figure 3.

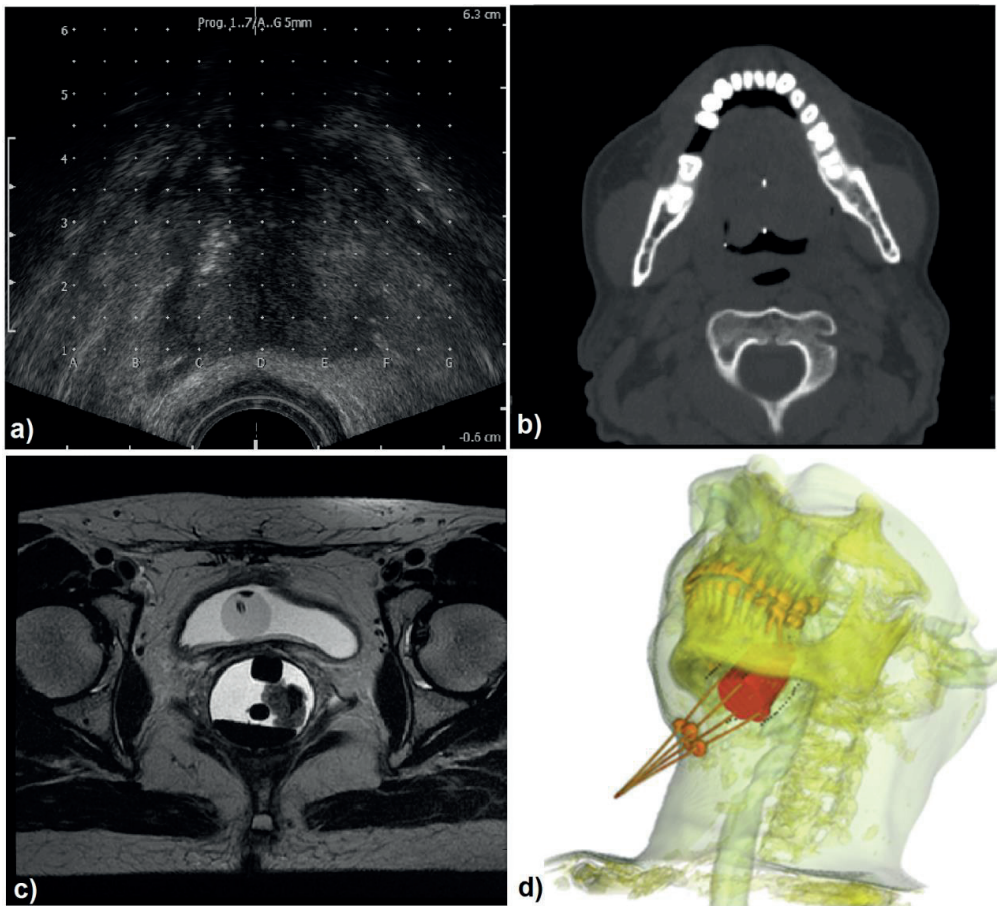


Figure 3. **a)** TRUS image of a prostate patient; **b)** CT image of a head and neck patient; **c)** MRI image of a gynecological patient; **d)** 3D reconstruction from CT images including the clinical target volume (CTV) in red.

CT images provide information about the atomic number and mass (or electronic) density, which can be employed for tissue segmentation.⁸³ Dual energy CT scanners that acquire images using two different x-ray energy spectra may allow a more accurate extraction of tissue characteristics.⁸⁴⁻⁸⁶ These characteristics are highly important for low energy brachytherapy sources for which photoelectric effect is dominant. Therefore, energy deposition is highly dependent on tissue composition as can be seen by the mass absorption coefficients (μ_{en}/ρ) of various human tissues relative to water (Figure 1).^{3,8,33} Other modalities such as MRI and US do not provide electronic densities, but may provide excellent visualization of soft tissue (MRI - Figure 3.c) and real time visualization to outline organs as prostate and urethra (US - Figure 3.a). All imaging techniques are greatly aided by image registration between

either CT and MRI or CT and US for which CT based speed of sound correction, due to different tissues densities, are being evaluated to improve US images.⁸⁷

Although highly relevant for low energy sources, tissue segmentation may not be necessary for ¹⁹²Ir energies. Rivard et al.¹³ discussed which commonly treated anatomic sites (prostate, breast, gynecological, skin, lung, penis and eye) may show significant differences between the actual calculation formalism (TG43-U1 homogeneous water phantom) and more accurate models (MBDCA). None of the evaluated sites are expected to show significant differences, for ¹⁹²Ir photon spectrum, due to tissue composition or attenuation. Differences are expected only due to shielding (gynecological, skin and eye) or scattering (breast, skin, lung penis and eye) due to interfaces with air.¹³ Therefore, a homogeneous phantom with image-defined boundaries may provide accurate dose calculations for high-energy brachytherapy sources.

Proper tissue segmentation may not be possible even using CT images since image artifacts may not allow it as shown in Figure 4. Image artifacts that degrade image quality are due to the image reconstruction algorithm⁸⁸ processing transit images with high atomic number and density and may lead to wrong tissue and density assignment. Several methods have been employed to correct image artifacts, from manual contouring to sophisticated interactive algorithms, filtered images and sinograms.⁸⁸⁻⁹¹ Currently, efficient and robust methods are not commonly available and the potential of these algorithms to improve dose calculation accuracy needs to be studied (see section 4.4 Dose specification ($D_{w,m}$ and $D_{m,m}$) for more information about material misassignment).⁵

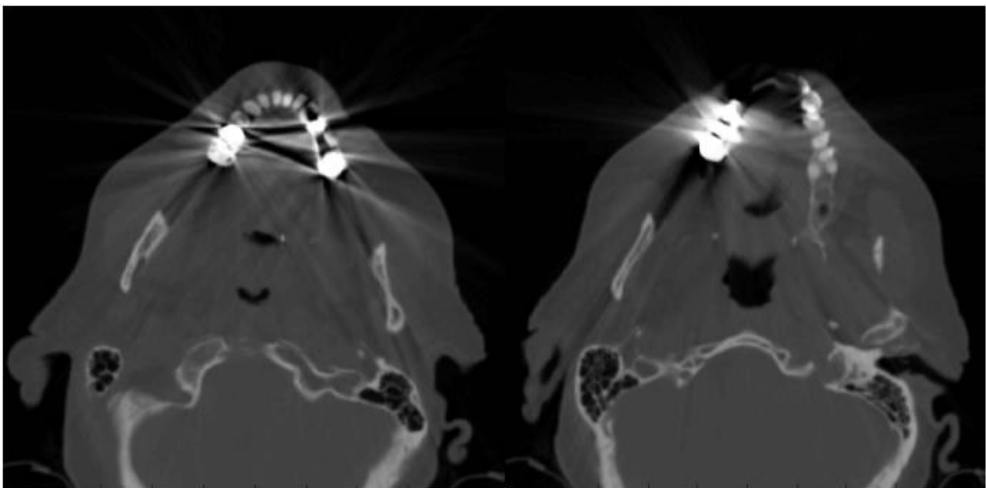


Figure 4. CT slices of a head and neck patient showing metal artifacts.

3.1.2 Brachytherapy applicators and shielding effects

Brachytherapy treatments may employ plastic or metal needles⁹² and a wide variety of applicators, from single channel cylinders to more complex applicators with several channels and shielding.^{10, 16, 26, 93} Moreover, some applicators such as balloons used for APBI may assume patient cavity shapes as discussed in section 4.3 (CAD-Mesh) and evaluated by White et al.⁸ for clinical cases.

Petrokokkinos et al. evaluated a shielded cylinder applicator (GM11004380 – a similar model was represented in section 4.3.1.4 - Shielded HDR vaginal applicator) with measurements and simulations using three dose calculation engines: ACUROSTM, a MC code and a commercial TPS (TG-43U1). Results showed differences of up to 90% between MC and TG-43U1 in the shielded side and up to 10% for clinically relevant points close to the applicator in the unshielded side as scatter reduction due to the partial shield was not taken into account by the TPS (TG-43U1).¹⁰ Results obtained using ACUROSTM and MC are almost equivalent except for differences between 2% and 10% in the penumbra of the shield.¹⁰

The Fletcher Williamson shielded applicator for HDR ¹⁹²Ir sources was extensively studied by several groups.^{18, 23-27} A MG model of this applicator was evaluated in this thesis and described in section 4.3.1.5 (Shielded HDR Fletcher Williamson applicator). This applicator was developed to reduce doses in organs at risk (bladder and rectum). A ratio between dose distributions obtained using a MC with and without the applicator is shown in Figure 5 for illustrative purposes. Results with and without the applicator are almost equivalent in the unshielded region (near the tip) though significant differences are visible in other regions. Applicator effects are considerable and may allow dose escalation as healthy structures can be preserved.

Dosimetric perturbations of a lead shield was studied by Candela-Juan et al. for ⁶⁰Co, ¹⁹²Ir and ¹⁶⁹Yb sources used for surface and interstitial HDR brachytherapy. An overdose near the shield, mainly due to backscattered electrons, can reach a factor of 3 at 0.1 mm from the shield for a ¹⁹²Ir source. Tissues can be preserved by adding 3 mm and 1 mm of bolus around the shield for ⁶⁰Co and ¹⁹²Ir, respectively.

Although shielded applicators show the most significant differences from TG-43U1 dose to water formalism, differences up to 5% within the target volume were observed for a gynecological case due to a hollow applicator (see sections 4.2.4.1 and 5.1.2).⁶

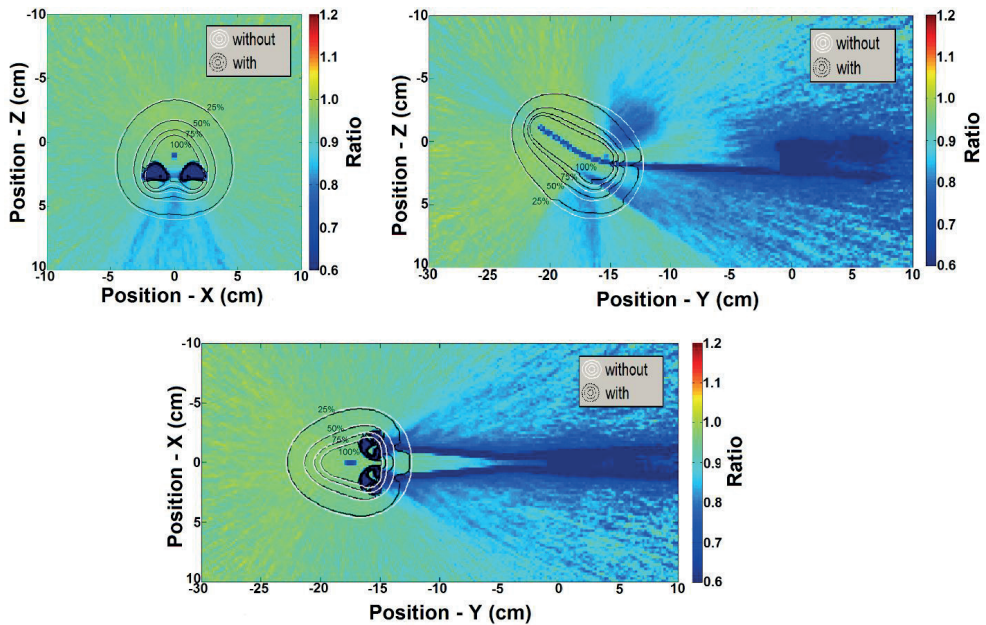


Figure 5. Ratio between dose distributions obtained with MC with and without including the Fletcher Williamson applicator. The dark blue region represents the applicator.

3.2 MC methods in brachytherapy

MC method is widely employed in several fields as astronomy, meteorology, traffic prediction and medical physics. In medical physics MC has been employed to simulate linear accelerators,⁹⁴ patients,⁹⁵ brachytherapy sources,⁷⁶ energy dependence of dosimeters,⁹⁶ neutron stimulated emission computed tomography,⁹⁷ to calculate ion chamber correction factors due to wall attenuation and scatter⁹⁸⁻¹⁰⁰, and for several other applications. Rogers published a review about MC simulations for medical physics.¹⁰¹ He searched for the term ‘Monte Carlo’ on PubMed[†] getting 14452 hits as of January 2006 whilst the same search performed 9 years later (January 2015) showed 38901 hits. The number of papers per year including the term ‘Monte Carlo’ is shown in Figure 6. The increase use of MC codes is related to the increase in computing power that allows shorter simulation times.

Several MC codes are available comprising a wide variety of applications. MCNP was originally developed to transport neutrons and photons. Currently, MCNP can transport several particles as photons, neutrons, electrons, protons, heavy ions and others.^{22, 49}

[†] <http://www.ncbi.nlm.nih.gov/pubmed/>

PENELOPE (Penetration and ENERGY Loss of Positrons and Electrons)¹⁰² transports electrons, positrons and photons. GEANT4 (GEometry ANd Tracking) transports a wide variety of particles and is the basis of GATE (Geant4 Application for Tomographic Emission).^{28, 103} EGS (Electron Gamma Shower) is a photon-electron coupled code considered the most used general purpose MC code in medical physics.¹⁰¹ Recent data about MC codes usage were not found. However, a refined search within papers with the term ‘Monte Carlo’ shows 637 papers with at least one of the expressions ‘MCNP’, ‘MCNP4’, ‘MCNP5’ or ‘MCNP6’; 643 with at least one of the terms ‘GEANT’, ‘GEANT4’, ‘G4’ or ‘GATE’; 218 papers with the term ‘PENELOPE’; 809 papers with at least one of the terms ‘EGS’, ‘EGSnrc’, ‘EGS3’, ‘EGS4’, or ‘BrachyDose’. Results indicated that EGS, and its versions, is still the most used code. However, other codes are almost equally used.

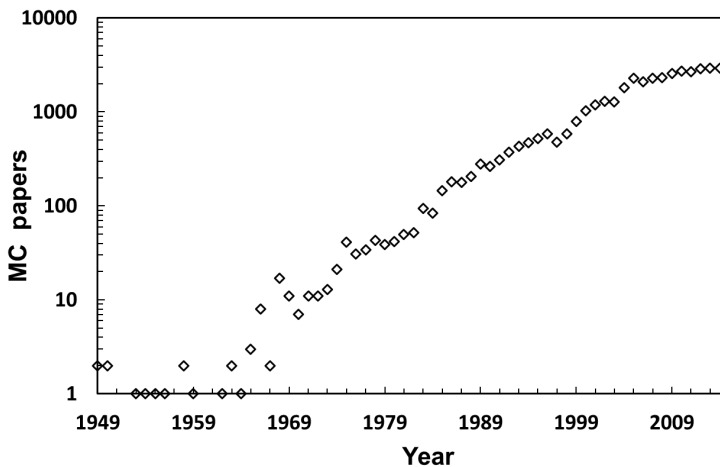


Figure 6. Number of papers per year including the term ‘Monte Carlo’. Results of a PubMed search (20 January 2015).

MC plays a key role in brachytherapy for clinical practice and research. The first computational efforts to obtain dose distributions around brachytherapy sources date from the 60’s, with 3D models used as early as 1971.^{7, 104, 105} Landry et al. summarized some results obtained during the 90’s comparing MC dose distributions against experimental data using thermoluminescent dosimeters (TLD) and diodes.⁷ Agreement within 5% for ¹²⁵I and 3% for ¹⁹²Ir sources validated MC calculations.¹⁰⁶⁻¹¹¹ TG-43 recommends that at least one experimental and one MC calculation of dosimetry parameters should be published before using a source clinically.^{1, 2} This recommendation consolidated MC as a standard for

brachytherapy. Moreover, experimental measurements are complex due to the sharp dose gradient in the brachytherapy energy range. However, MC should not be trusted blindly as pointed out by Williamson et al.¹⁰⁸

MC code is a gold standard MBDCAs whose importance goes beyond source models as patient specific dose calculations can be performed. Despite its well-known accuracy, MC has not been implemented in clinical practice due to its calculation time.¹¹² Significant computational requirements are inherent of a stochastic method for radiation transport that must simulate a large number of particles to produce statistically relevant results. This may no longer be a problem due to the computational power available nowadays.¹¹² Currently, the simulation time necessary to obtain an average dose uncertainty of 2% for an intracavitary case with 6.6×10^6 voxels is 27 min using an Intel Xeon X5650 processor with twelve cores of 2.67GHz and 32 Gb of RAM. This is reduced to 5 min on a SGI C2112 server (Silicon Graphics International Corporation, Chippewa Falls, USA) consisting of 16 processors with eight cores of 2.4 GHz each.⁶ Landry et al. obtained calculation time about 6 and 12 min for 2% uncertainty for a breast and a prostate implant, respectively.⁷ Literature reported MC results obtained within seconds for low-energy sources and few minutes for ^{192}Ir .¹¹² Such simulation times may be suitable for a future clinical implementation.

Other issues related to MC are described within this thesis according with the studied subject, e.g. Track length estimators (section 4.1.1.2), dose report quantities (sections 1.3, 4.4 and 5.3), applicator modelling (sections 4.2.1 and 4.3 and 5.2).

MATERIALS AND METHODS

Chapter 4

4 MATERIALS AND METHODS

4.1 Monte Carlo codes

This section includes general information about the MC codes used in this thesis whilst specific simulation parameters were described in each section.

4.1.1 MCNP

MCNP version 5 and 6 were used in this thesis since only version 5 was available by the time some results were obtained. No differences were observed between the versions, except for MCNP6 new features as CAD-Mesh. MCNP is a multipurpose radiation MC transport code^{22, 113} widely employed in medical physics,^{8, 93} which can involve high-resolution voxel phantoms. Therefore, MC codes must handle a large amount of data requiring a large RAM memory and long CPU times. To increase simulation efficiency the Harvard/MIT Boron Neutron Capture Therapy clinical trials team developed lattice speed tally enhancement (LSTE) for simulations with large number of voxels.²⁹

The LSTE function can be employed under specific situations such as: a) a hexagonal lattice must be present in the geometry; b) all F4 (MCNP6 tally) tallies contain a hexahedral lattice; c) all F4 tallies have associated DE/DF cards; d) nested lattices are scored together. However, this function is not compatible with all tallies. Simulations with F4 tallies can be faster by a factor of 100 or more than simulations with F6 (MCNP6 tally) tallies since LSTE does not work for F6 tallies even though both tallies are track length based estimators. When the SPDTL card is active, tracking is more efficient since it considers only lattice geometries enclosed in a parallelepiped, removes general surface checks, removes extraneous energy bins and tally modifiers. LSTE retains only the tally multipliers (DE/DF cards) necessary to convert average photon energy fluence to kerma²⁹.

MCNP6 calculations were performed using a track length estimator tally, using the MCPLIB84 photon cross-section library in Mode P which means secondary electrons were not transported (therefore, kerma was scored), except for one simulation described in item 4.1.1.3 (Pulse height tallies). Results were converted to collision kerma using mass-energy absorption coefficients from NIST.¹¹⁴ All cases were simulated using the ¹⁹²Ir photon spectrum available from the National Nuclear Data Center (NNDC)¹¹⁵. Photons were transported down to an energy cut-off of 1 keV.

4.1.1.1 MCNP6 mesh capability

The capability of handling mesh geometries was recently included in the MCNP6 beta 2 release, which can handle first and second order tetrahedral, pentahedral and hexahedral elements defined through text files directly generated by two commercial programs, AbaqusTM (Dessault Systèmes, France) and ATTLA (Transpire Inc., Gig Harbor, WA) or by converting the volume elements generated by other programs, such as ENGRID or GMSH.¹¹⁶ We opted for tetrahedral meshes defined using the .ele/.node files used for Geant4 simulations converted to the MCNP6 format.¹¹⁷

4.1.1.2 Track length estimator tallies

Track length estimator tallies can be used under CPE conditions, which is achieved for the ¹⁹²Ir spectrum for distances greater than 2 mm from the source.^{118, 119} Under CPE conditions dose values are approximate by collision kerma (and even kerma in low atomic number materials where bremsstrahlung is negligible) and can be obtained by multiplying the energy fluence ($E \cdot \Phi_E$) by $\mu_{en/\rho}$ as described in equation 2. Fluence values were scored for N energy bins (i) with 1 keV resolution using MCNP6. This methodology is efficient since the number of tracks crossing a voxel is much higher than the number of interactions in it and leads to accurate results within the brachytherapy energy range for mm-sized voxels.^{8, 76, 120} This approach is followed in the first MC simulation (track length) mentioned above.

$$D \approx \sum_{i=1}^N \left[\Phi_{E_i(m)} \cdot E_i \cdot \left(\frac{\mu_{en}}{\rho} \right)_{(w \text{ or } m)} \right] \quad 2$$

4.1.1.3 Pulse height tallies

Pulse height tallies are analogous estimators¹²¹ (like a physical detector) scoring the energy deposited per interaction inside of the scoring volume. It is an accurate method, even without CPE, with the penalty of being statistically less efficient than track length tallies. This approach does not introduce significant uncertainties since electrons with 50 keV energy have a mean residual range of 0.04 mm in water that is almost ten times shorter than the smallest voxel dimension,¹²² and bremsstrahlung production below 50 keV in water and low atomic number material is completely negligible.¹²³ Only one simulation was performed using this tally to quantify possible differences due to the absence of CPE that may occur for

small scoring volumes and near material interfaces (see section 4.4 - Dose specification ($D_{w,m}$ and $D_{m,m}$) for more information).^{13, 34} $D_{m,m}$ values including effects of electron transport were obtained simulating the whole CT geometry. However, dose values were scored only for one sagittal slice to reduce the simulation time since it increases with the number of scoring volumes, which can make simulations impractical.

4.1.2 Geant4

The MC toolkit Geant4.9.5.p02 was used in this thesis, using the G4EmLivermorePhysics class for low energy electromagnetic physics and the layered mass geometry method.¹²⁴ The code was used to validate MCNP6 calculations with mesh geometries (section 4.3 - CAD-Mesh). A voxel grid was used to represent the patient geometry derived from CT imaging and a parallel world contains the model of a brachytherapy source and applicator. In locations where voxels and applicator model overlapped, photons were transported in the latter.

To perform MG modelling we installed the Geant4 library CADMesh version 0.6.2 (Ref. 125) which enables the import of tessellated surfaces or volumes. It has been reported¹²⁶ that the use of tessellated surfaces based on the G4TessellatedSolid class requires longer simulation times than tessellated volumes based on an assembly of G4Tet (Geant4 class for modelling tetrahedra). This was confirmed in our work; therefore the latter approach was used. Several file formats are supported by CADMesh; An .ele and .node description of volume meshes composed of a collection of tetrahedrons was adopted.[‡] The .node file contains a list of vertices which are grouped in the .ele file to describe volume elements. Volumes represented by a collection of tetrahedrons will be referred as MG. Upon import via CADMesh in Geant4 the .ele/.node tetrahedral mesh yields a G4Assembly volume (a class allowing to group a number of volumes such as G4Tet) to which a position in the parallel world and a material can be assigned.¹²⁶

4.2 AMIGOBrachy

AMIGOBrachy has been developed using MATLAB version 8.0 with the aim of providing tools such as: a) medical image processing, b) dwell position identification, c) needle detection, d) phantom creation using DICOM images, e) MCNP6 code input file

[‡] <http://tetgen.berlios.de/fformats.ele.html>

creation and f) dose analyses. All functionality of AMIGOBrachy is achieved through a user-friendly interface. The software is compatible with the TPS Oncentra™ (Nucletron, an Elekta company, Stockholm, Sweden) and BrachyVision™ (Varian Medical Systems, Inc., Palo Alto, CA) offering the capability to import treatment plans created on both TPS and perform simulations using the MCNP6 code. Currently, CT and MRI images can be imported, but automatic segmentation and density calibration curves are not available for MRI images, which should be segmented using contours or thresholds defined by the user. Figure 7 shows a diagram of the main functionalities of the software describing the entire process.

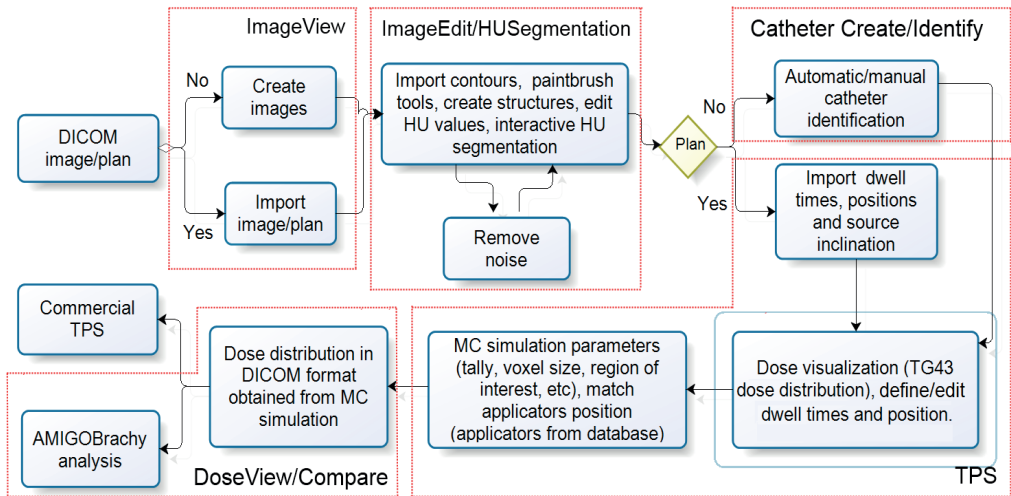


Figure 7. Flowchart with AMIGOBrachy's main functionalities, which are described in the user-guide. The process starts with importing or creating a DICOM sequence of images, followed by defining the simulation parameters and initiating MCNP6, and finishes by importing and analyzing the simulated dose distributions.

The software creates a MCNP6 input file by initiating several simulation parameters, e.g. the energy cutoff, detailed or simple physics, the selection of tallies and regions of interest. In addition, one can choose between the following transport/scoring schemes: photon transport in water and dose scoring in water ($D_{w,w}$), photon transport in the medium and dose scoring in water ($D_{m,w}$) or photon transport in the medium and dose scoring in the medium ($D_{m,m}$)⁵. AMIGOBrachy can be readily adapted to prepare MC input files for other MC codes. Although simulations are performed with MCNP6, the user has no need to interact with the code since AMIGOBrachy starts the simulation and automatically imports the results.

MCNP6 can generate photon energy distributions in all voxels, which can be used for energy response correction of radiation detectors.¹²⁷ This also allows studying the effect of non-water heterogeneities on the photon spectrum. This capability was built into the current implementation of AMIGOBBrachy.

AMIGOBBrachy can import the trajectory of the source and simulate the source movement using source speed profiles defined by the user. The methodology to derive transit dose component¹⁷ for brachytherapy treatments was described in section 4.5 (Transit dose).

4.2.1 Brachytherapy applicators

Commercial or in-house made brachytherapy applicators have a wide range of geometries and compositions. Some applicators may affect the dose distribution significantly due to the geometry and the material used. AMIGOBBrachy can handle applicators in three different ways:

- using a database of applicators defined through an analytical geometry (Figure 8.a) combined with voxel phantoms. In this first version two plastic applicators and one metal needle are available;
- converting applicator contours to voxels (Figure 8.b);
- using mesh geometries (Figure 8.c) created by CAD/CAE (Computer Aided Design and Computer Aided Engineering) to perform simulations using MCNP6.¹¹⁷

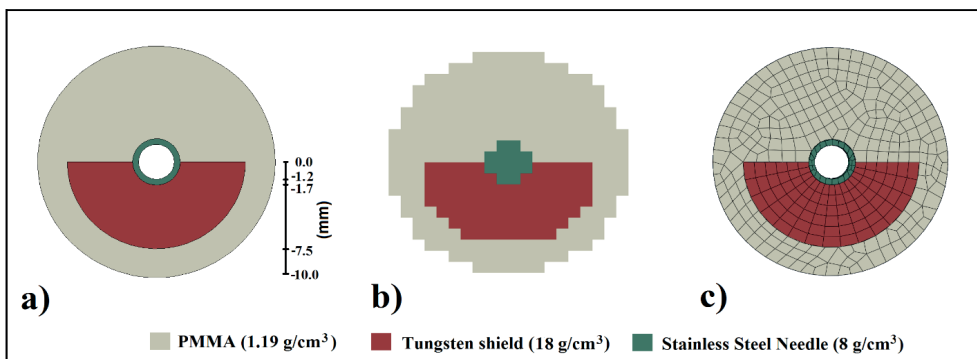


Figure 8. A 180° tungsten shielded applicator modeled using: **a)** analytical geometry; **b)** $(1 \times 1 \times 1) \text{ mm}^3$ voxels; **c)** mesh structures created with AbaqusTM. The dimensions are based on the GM11004380 applicator (Varian Medical Systems) and on the ACUROSTM applicator database.

The applicator's position can be obtained from DICOM file headers, when available, or defined by the user through two or more points depending on the applicator geometry. Moreover, applicators can consist of one or more small and/or thin structures, which cannot be accurately represented by regular voxels (i.e. the hollow needle in Figure 8.b).

4.2.2 Validation

Dose distributions obtained with AMIGOBBrachy/MCNP6 were compared against dose distributions exported from BrachyVision™ version 10.0 employing a Linear Boltzmann Transport Equation (LBTE) solver, ACUROS™, which can handle non-water heterogeneities.^{10, 11, 18, 128}

4.2.3 Uniform phantoms

The validation process involved several steps going from source parameter validation up to clinical case comparisons against a commercial TPS. AMIGOBBrachy currently models two HDR ¹⁹²Ir sources; microSelectron⁷⁷ (Nucletron), and GammaMed Plus⁷⁶ (Varian), and an electronic brachytherapy X-ray source (Axxent; Xoft, San Jose, CA).¹²⁰ The sources were validated by comparing TG43-U1^{1, 2} parameters such as anisotropy function, radial function and air kerma strength against values from the literature (data not show). Dwell times and dwell positions were validated by comparing the MC input generated with AMIGOBBrachy against DICOM header information and reports from TPS.

Material compositions and dose grid effects were verified by comparing dose distributions obtained with a DICOM object of 200x200x200 voxels, with a 1 mm resolution, consisting of a cubic phantom (10x10x10 cm³) positioned in the middle of the image and surrounded by air was created for validation purposes. Simulations were performed for 9 dwell positions within homogeneous phantoms consisting of all tissues available in the ACUROS™ library (lung, adipose tissue, water, muscle, cartilage and bone)¹²⁹ using dose scoring grids of 1 mm slice thickness and a width/height of 0.50, 1, 2.50 and 5.0 mm.

4.2.4 Clinical cases

Two treatment plans were created for a GammaMed Plus ¹⁹²Ir source using DICOM patient images from one interstitial and one intracavitary case. The dose distributions were calculated considering the material compositions and densities provided in the ACUROS™

user guide. The dose grid resolution was the same as the image resolution used in each case, while the dose grid sizes (i.e. the number of voxels) were defined interactively considering the ACUROSTM memory requirements. The distance between the isodoses and the dose values per voxel were compared.

The treatment plans were then imported in AMIGOBBrachy to generate MCNP6 input files by reproducing the TPS configuration. This includes tissue contours, materials, dwell positions, applicator, dose grid and voxel size. Dose calculations were reported as $D_{w,w}$ (as adopted by TG-43U1) and $D_{w,m}$, with the type A ($k=1$) simulation uncertainty component less than 1% within the region covered by the 30% isodose.

A sequence of images illustrating the steps necessary to perform a simulation using a treatment plan imported by AMIGOBBrachy is shown in Figure 9.

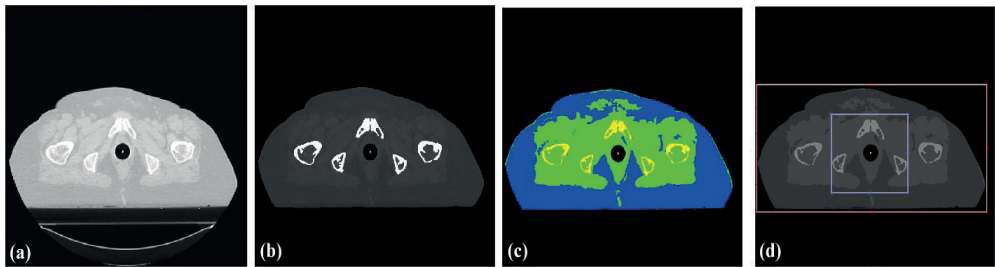


Figure 9. A sequence of images used by AMIGOBBrachy: **a)** importing the DICOM patient CT image; **b)** defining structures by importing DICOM contours (e.g. the highlighted bone contours); **c)** defining the material map (using HU numbers or drawing tools), which consists of air (black region), adipose tissue (blue region), muscle (green region) and bone (yellow region); **d)** defining the voxel phantom region (external rectangle) and the dose scoring region (internal rectangle).

4.2.4.1 Intracavitary case

The treatment plan for an intracavitary gynecological case was made with a DICOM CT image set consisting of 63 slices with 512x512 voxels, 3 mm slice thickness and voxel size of 0.98 mm. Dose distributions were calculated for a single guidance needle in the middle of a hollow plastic cylinder applicator (external diameter of 3.5 cm and 0.4 cm wall thickness). The applicator is placed in a phantom representing the patient with all voxels

assigned to one of six materials (polyphenylsulfone (modelling the applicator), water, bone, muscle, adipose tissue and air) from the ACUROS™ database. There are 17 dwell positions and the prescribed dose is 7.5 Gy per fraction at 0.5 cm from the applicator's outer wall. The following situations were considered: a) "infinite" homogeneous water phantom with at least 20 cm of water between the scoring voxels and the closest boundary with air¹³⁰; b) body boundaries defined using CT images with all materials assigned as water, including the applicator; c) CT based geometry where tissues are assigned as water and the applicator assigned with its real composition; d) CT based geometry with tissues and applicator assigned with their proper composition. Air was assigned to the regions outside the body except for case a.

4.2.4.2 Interstitial case

The treatment plan for an interstitial arm sarcoma case was made with a DICOM CT image set consisting of 253 slices with (512 x 512) voxels, 1.25 mm slice thickness and pixel spacing of 0.59 mm. Dose distributions were calculated considering 9 channels, 106 dwell positions and a total dwell time of 336.6 s. The following situations were considered: a) "infinite" homogeneous water phantom, as defined in the previous validation case; b) all tissues assigned as water; c) all tissues assigned as muscle; d) tissues assigned as muscle and bone. Plastic catheters were not modeled and air was assigned to the regions outside the body except for case a.

4.3 CAD-Mesh

4.3.1 Geometries of interest

Three types of applicators were considered in this thesis; two gynecological applicators used with an ¹⁹²Ir HDR source and a balloon applicator used with an EBS operated at 50 kVp. The ¹⁹²Ir spectrum was taken from National Nuclear Data Center¹¹⁵ and the 50 kV spectrum from Liu *et al.*¹³¹ using a Geant4 model based on the work of Rivard *et al.*¹³². Additionally, simpler geometries such as a water cube and a spherical APBI applicator were employed for estimation of calculation efficiency and validation. All geometries were simulated with both MC codes using the same MG. Although there are differences between the input formats, both codes use the same information, which are nodes (defined using cartesian coordinates) and faces (defined through node connections).

4.3.1.1 Water cube

A water cube of $(20\text{cm})^3$ was modelled as a MG with a number of tetrahedrons varying between 12 and 191514. In Geant4 this cube was treated as an applicator and placed in the parallel world. In Geant4 no voxels were used in the main world to compare calculation times fairly against MCNP6, where it is not currently possible to combine voxels and MG. Again a point source with an ^{192}Ir spectrum was positioned at the origin and the time to transport 10^7 photons was recorded for Geant4 and MCNP6 using a single core on the same computer. The simplistic model was used to measure the speed of both codes while dose distributions were compared to verify the consistency between the codes. For the latter 1 billion photons were simulated.

4.3.1.2 Idealized APBI applicator

A spherical shell of thickness 0.4 mm and outer radius 2.5 cm was modeled using two MeshLab (Visual Computing Lab, ISTI, CNR) generated tessellated spherical surfaces. A python script (tetnest.py[§]) was then used to convert the two surfaces into a MG (.ele and .node files). Three levels of detail were investigated with MG containing 4472, 17824 and 69408 tetrahedrons. Figure 10 shows an example of MG. It was necessary for the G4Tet class of Geant4 to disable a G4Exception caused by degenerate polyhedrons having volumes smaller than a set threshold. These MG were used for direct comparison with simulations performed with CSG representation of the same geometry.

The material used is a polymer loaded with barium for x-ray imaging purposes. The composition and percentage by weight are as follows: H - 4.640%; C - 30.970%; N - 7.230%; O - 1.096%; Si - 16.540%; Cl - 36.570%; S - 0.549%; Ba - 2.350% and the mass density is 1.2 g/cm^3 . For this case, a photon point source was located at the center of the spherical shell. In addition to the 50 kV and ^{192}Ir spectra, monoenergetic photons with energies 20, 30, 40, 50 and 100 keV were used to verify the agreement for different energies.

Using the 50 kV spectrum, the time to transport 10^7 photons was recorded for Geant4 using the MG of different elements as well as the CSG.

[§] <https://github.com/christopherpoole/tetnest>

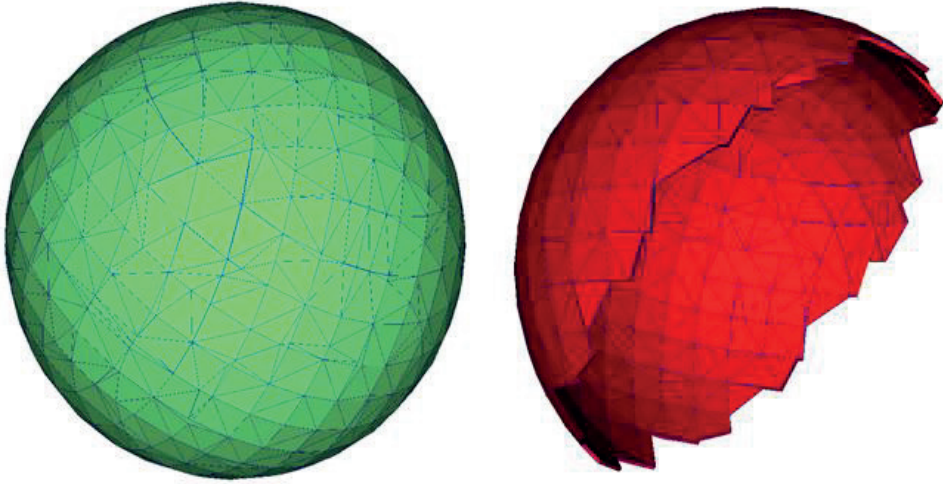


Figure 10. Example MG for the idealized APBI applicator showing the external surface and an inner section using a cutaway plane. The wall material is barium loaded polymer.

4.3.1.3 APBI balloon applicator

An APBI breast balloon applicator (Xoft Inc, an iCad subsidiary, San Jose, CA,) consists of a polymer balloon with the same composition and mass density as in the previous section. Figure 11.a shows the enhanced visibility on CT images due to the presence of barium in the balloon wall as well as the shape of the applicator. The inserted balloon's inner contour was manually outlined on each CT slice of an APBI patient,⁸ forming a cloud of points. A second set of points was generated by expanding the initial set by 0.4 mm about the centre of mass of the initial set. Each set was imported in MeshLab where a tessellated surface was generated using the convex hull function for each cloud of points (inner and outer surfaces of balloons with normal facing inwards and outwards respectively) and exported in .ply format. A convex hull is the minimum geometrical volume that contains all of the contour points such that the vector between any two of the contour points does not lie outside of the volume. An example MG is presented in Figure 11.b. A photon point source with a 50 kV photon spectrum was positioned at the center of mass of the cloud of points used to generate the balloon. The contour points were also used to create a water phantom with the balloon wall represented by voxels with the same resolution as the reference patient CT images $0.82 \times 0.82 \times 2.00 \text{ mm}^3$, evaluated using the same simulation parameters as the MG

simulations. As can be seen in Figure 11 the APBI applicator also includes a high density source channel end cap which is used to compensate for the lack of attenuation resulting from the air channel. This end cap and the catheter were evaluated in a separate study⁸ since they can be modelled using CSG and the goal of this study is MG modelling of the balloon.

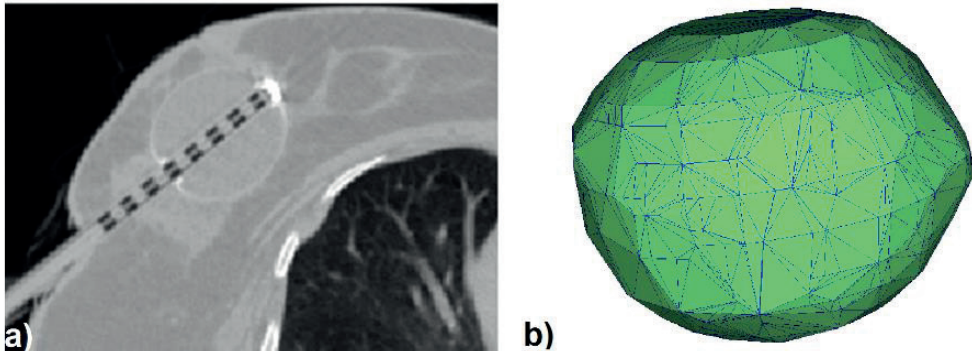


Figure 11. **a)** Axial CT image of an APBI balloon applicator inserted in a post surgical breast cavity. The wall is clearly visible due to barium loading. The EBS channel is occupied by a dummy insert to identify dwell positions. The balloon is filled with a saline solution. The high intensity pixels correspond to the end cap. Neither saline solution nor end cap are modeled in this thesis. **b)** MG for the APBI applicator showing the external surface.

4.3.1.4 Shielded HDR vaginal applicator

A shielded cylindrical vaginal applicator consisting of a PMMA ($\text{H}_8\text{C}_5\text{O}_2$, density 1.19 g/cm^3) cylinder containing a tungsten half cylinder shield and a central stainless steel channel (see Table 2 for the composition of the channel and the shield) for an ^{192}Ir source and a steel drive cable was modelled (Figure 12). The applicator was also modelled by CSG for validation. The geometry for this applicator was based on a published model.¹³³ The mesh geometry was created using AbaqusTM to first create a surface mesh. The surface mesh was then exported in the STereoLithography (STL) file format to Engrid to create the tetrahedral elements forming a volume mesh. Two levels of refinement were investigated (MG with 16530 and 129860 elements). Additionally a treatment plan obtained from a clinical case with 7 dwell positions spaced 0.5 cm apart was also considered.

Table 2. Material properties of the steel channel and tungsten shield of the shielded vaginal applicator (see Figure 12). Elemental composition expressed in percentage of weight (%w).

material	densit ρ (g/cm^3)	%w									
		C	Cr	Fe	Mn	Mo	Ni	P	Si	S	W
Stainless steel	8.00	0.08	17.00	65.00	2.00	2.50	12.00	0.00045	1.00	0.03	0.00
Densimet D180	18.00	0.00	0.00	1.50	0.00	0.00	3.50	0.00	0.00	0.00	95.00

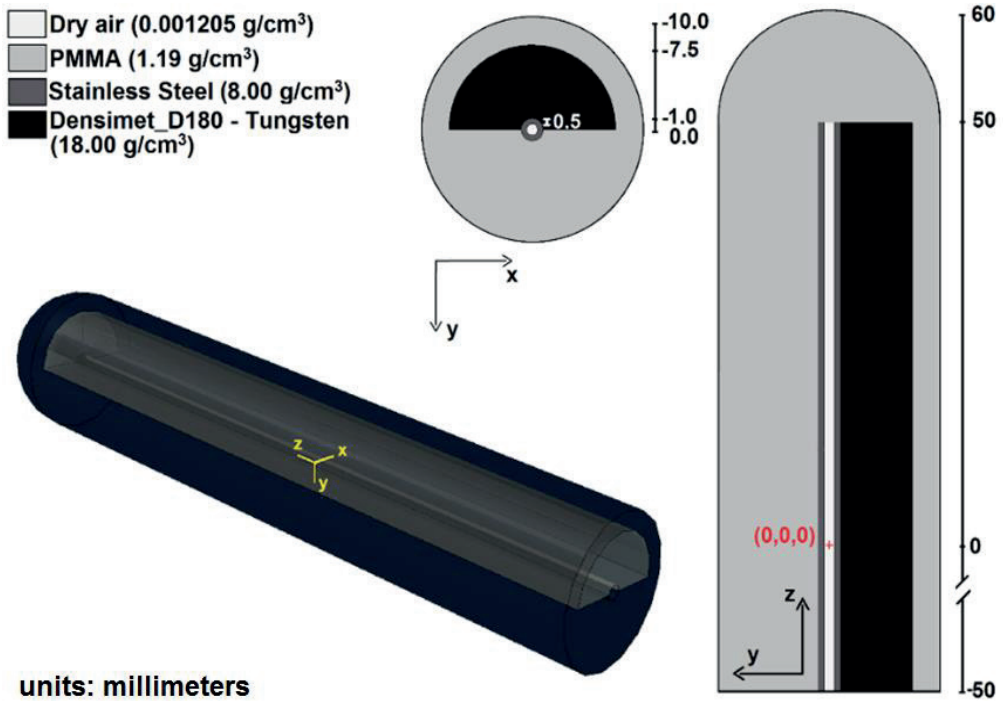


Figure 12. Schematic representation of the shielded cylindrical vaginal applicator.

The shield of the applicator was modelled in a separate simulation to estimate the time required to simulate 10^7 primary photons from the ^{192}Ir source in Geant4 and MCNP6. The number of elements composing the shield was varied from 101 to 59365. In this simulation, as for the MG water cube, the water box present in the main world was not voxelized.

4.3.1.5 Shielded HDR Fletcher Williamson applicator

The shielded HDR Fletcher Williamson applicator consists of three stainless steel channels and two polysulfone (PSU) ovoids with tungsten shields included to reduce the radiation dose to the bladder and the rectum (Figure 13). This figure shows how modelling the applicator using CSG may prove challenging if all components including screws and holders need to be modelled. The compositions were obtained from the vendor under a non-disclosure agreement. The applicator was modelled using a CAD (Computer-Aided Design) file provided by Nucletron to create the mesh surfaces with AbaqusTM.



Figure 13. CAD representation of the Fletcher Williamson applicator (from AbaqusTM).

An ¹⁹²Ir point source was located at 20 dwell positions inside each of the three channels with inter-dwell distance of 0.5 cm and loading 5.5 cm (from the tip) of the central channel and 1.5 cm of each ovoid channel. The source positions and the dwell times were obtained from a treatment plan to create a more realistic dose distribution.

CSG modelling of this applicator proved challenging since MCNP6 requires a torus to be rotationally symmetric around an axis parallel to one axis of the main system (x, y or z). To allow a straightforward CSG representation the lateral channels were aligned with the central channel by a 4.5 degrees rotation. This rotation was also applied to the ovoids and shields. An equivalent MG was generated.

4.3.2 Simulation details

The patient geometry was approximated by a water box of dimensions $(20\text{cm})^3$ with $(2\text{mm})^3$ voxels to represent the patient geometry for both MC codes. Kerma was scored per event using track length estimation 1 billion primary photons were simulated for each case studied, except for the simulations performed for the computation time investigation, which used 10^7 primary photons instead. Energy depositions occurring in applicator model were discarded in this study. The dose in voxels partially covered by the applicator model was not corrected for the fractional voxel mass which received energy depositions, which affects only the response of these voxels.

The Geant4 calculations were divided in 600 jobs and distributed using the HTCondor queuing system¹³⁴ on a heterogeneous cluster of 9 computers comprising a total of 194 cpus and running Ubuntu and OSX operating systems, each having the same version of Geant4 and CADMesh installed. Calculation time estimations were performed on a single core of an Intel Xeon X5650 processor running at 2.67GHz. The MCNP6 calculations were performed using a single Intel i7 (2860QM) with four cpus of 2.5GHz running Windows 7. For calculation time estimations the same machine and setup was used as for the Geant4 calculations.

The use of MG was validated as follows: for cases with the idealized APBI spheres, dose distributions from Geant4/MCNP6 obtained with the mesh representations with different numbers of tetrahedrons and with the CSG representation of Geant4/MCNP6 were compared using dose ratios. The same was done for the gynecological applicators (MG vs. CSG). In this case only an MCNP6 CSG representation was employed.

The balloon case cannot be easily simulated since the balloon has a deformable irregular shape which is patient-dependent. Thus only simulations with mesh geometries in Geant4/MCNP6 were considered.

4.4 Dose specification ($D_{w,m}$ and $D_{m,m}$)

This section describes the evaluated clinical case, simulation parameters and the methodology employed to convert $D_{m,m}$ to $D_{w,m}$ using SCT and LCT.

4.4.1 Clinical case

The treatment plan for an interstitial clinical head and neck case was made with a CT image set consisting of 80 slices with 512x512 voxels ($0.39 \times 0.39 \times 2.00 \text{ mm}^3$). Dose distributions were calculated for a HDR ^{192}Ir microSelectron v.2 (Nucletron) source^{76, 77} and six plastic catheters with a total of 99 dwell positions. 25 CT voxels were visually selected to evaluate the photon spectrum at several regions of the irradiated volume occupied by different materials and at different distances from implanted sources. The patient CT geometry and the location of the 25 voxels for which the photon spectrum was scored (see the next section) are shown in Figure 14.

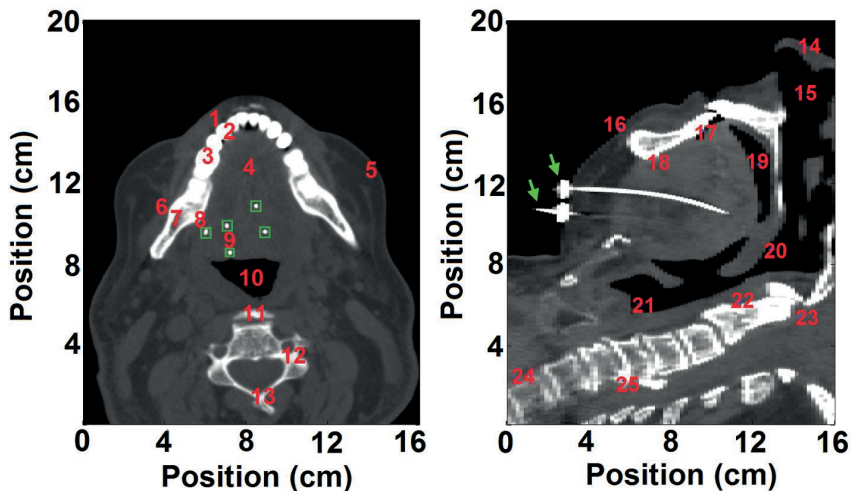


Figure 14. Axial and sagittal view of the evaluated head and neck clinical case. The numbers indicate voxels positions where the photon spectrum was scored. Green arrows and squares were added to show the catheter positions (five of the six catheters can be visualized).

4.4.2 Monte Carlo simulations

The CT images were segmented using auxiliary software¹³⁵ to create three voxel phantoms including: I - a water ($\rho = 1 \text{ g/cm}^3$) and air ($\rho = 0.0012 \text{ g/cm}^3$) phantom; II - a water and air phantom with mass densities obtained from a calibrated CT image; III - a phantom

with proper tissue compositions (adipose tissue, muscle and bone)¹²⁹, with mass densities obtained from a calibrated CT image. The regions with air are the same for all models adopted so henceforward this material will not be mentioned anymore when referring to the described phantoms. These phantoms were employed to evaluate the effect of different approaches/simplifications that can be easily adopted by MC users. Moreover, $D_{w,w}$ values obtained with phantom II were compared (data not shown) against $D_{w,m}$ (LCT) and $D_{m,m}$ values obtained with phantom III since using phantom II is simpler, but may still provide reasonable results. The numbers (I, II and III) were used in the next sections to distinguish the three different approaches.

Simulations were performed with MCNP6 for the three phantoms, scoring in all voxels the mean photon energy per voxel, $D_{w,m}$ (LCT) and $D_{m,m}$ and for the 25 selected voxels the full photon energy spectra with a 1 keV resolution (Figure 14). $D_{w,m}$ (LCT) and $D_{m,m}$ values were obtained using a track length estimator (tally F6) assuming CPE conditions so secondary electrons were not transported (see next section). Mass-energy absorption coefficients ($\mu_{en/\rho}$) from the National Institute of Standards and Technology (NIST)¹¹⁴ for either water or medium were employed to convert photon energy fluence to collision kerma (equal to absorbed dose under CPE). In addition, $D_{m,m}$ values were calculated transporting secondary electrons and using a pulse height tally (F8) to verify $D_{m,m}$ obtained with a track length tally F6 to study the validity of the CPE approximation on the dosimetry (and thus on using a track length estimator for this kind of geometries) on the current dose calculation voxel grid. Earlier investigations confirmed the validity of CPE using even smaller voxels ($0.1 \times 0.1 \times 0.1 \text{ mm}^3$),¹¹⁸ but studied the problem outside a brachytherapy source positioned in pure water to estimate the importance of modelling charged particles emitted in the source decay. CPE conditions are achieved for the ¹⁹²Ir spectrum for distances greater than 2 mm from the source.^{118, 119} However, breakdown of CPE can occur near material boundaries.¹³ The effect of the interfaces between different materials and their influence on the CPE assumption has not been studied before in a CT defined phantom with voxel dimensions as those adopted in this study.

The number of primary photons (N) was set to 1 billion (10^9) for the mean energy simulation, 10 billion for the track length and photon spectrum simulations, and 30 billion for pulse height tally simulation.

4.4.3 $D_{w,m}$ (SCT and LCT) and $D_{m,m}$ values for several tissues

The photon spectrum in the 25 selected voxels was used with materials encountered in the head and neck region, but also with some other materials. $D_{w,m}$ (LCT), $D_{m,m}$ and mean photon energy values were obtained for several human tissues (prostate, lung, adipose tissue, breast, skin, bladder, muscle, cartilage, mandible spongiosa, bone and teeth)¹²⁹ with the full photon spectrum obtained at the 25 evaluated voxels. The contribution of separate parts of the photon spectrum to the total dose in each voxel was obtained by dividing the spectrum in 50 keV bins and calculating the percentage of the total dose from each bin.

$D_{w,m}$ (SCT) were obtained for each material assuming $(S_{col}/\rho)_w^m$ to be independent of the photon spectrum (Figure 1.b). Conversion coefficients were obtained using the ESTAR database⁴⁰ averaging $(S_{col}/\rho)_w^m$ values with energies between 0.010 MeV and 1.5 MeV since electron spectra were not simulated for the evaluated clinical case.

4.5 Transit dose

The dwell positions and the catheter contours can be imported from the BrachyVisionTM and the OncentraTM TPS, consisting of point coordinates related to the treatment plan geometry. These points were used to define the trajectory of the source inside the patient and its inclination. The length of the catheter and the number of contour points depend on the catheter contouring process and the number of segments created to define the source trajectory in the treatment plan, or, alternatively, on the method of defining the applicator in the TPS applicator library. The catheter points and the dwell positions were processed using an algorithm created with MATLAB version 8.0, which provides the trajectory of the source, the speed at each reference position, control points where the acceleration changes direction, the source orientation and the time necessary to travel between two consecutive points for both the source going into the patient and coming back to the safe.

The trajectory depends of the treatment plan and is mainly restricted to the region near to the target volume since the catheters outside of the body, in general, are not defined when planning. However, this is not a limitation for this study since its main interest is the transit dose due to the source travel between dwell positions, with a low speed near the dwell positions as shown in section 4.5.2 Validation.

4.5.1 Transit dose calculation

The transit dose distribution due to the source traveling inside the patient, without considering the dwell time, and the dwell dose distribution were obtained separately for 4 clinical cases using the MCNP5 MC code. The transit dose and the dwell dose was evaluated using a phase space file, which was generated on the surface of the stainless steel capsule encasing the ^{192}Ir isotope considering a 2 mm long cable. Since the goal was to analyze the transit dose component and the effect of several speed profiles, all the cases were simulated under the same conditions using a microSelectron v.2 source that was validated by simulating TG43-U1^{1, 2} parameters in a 30 cm diameter water phantom following the methodology proposed by Daskalov et al.⁷⁷ This approach ensures that differences between the cases are not due to the source model. The simulations were performed with 10^9 photons resulting in a dose uncertainty component type A ($k=1$) of less than 1.5% for points with a dose higher than 10% of the prescribed dose.

The MC transit dose calculations for the clinical cases simulate the source at discrete positions every 10 μm following the source trajectory with a sampling probability defined as the inverse of the instantaneous speed along the trajectory, which is proportional to the time spent by the source to travel within each 10 μm segment for the source going into the patient, traveling between the dwell positions and coming back to the safe. The discrete methodology should be equivalent to a continuous distribution due to the high spatial resolution adopted, which was evaluated using a continuous and a discrete distribution for a point source following a straight trajectory. This methodology was employed in a previous study⁴¹ where simulated data was also validated by comparison against experimental values obtained by Calcina et al.¹³⁶

This study adopted a maximum source instantaneous speed of 52 cm/s (ref. 46) with the instantaneous source speed at each position calculated using reference speeds and accelerations from the literature following the three approaches: a) uniform acceleration; b) an average speed obtained considering the inter-dwell distance and the travel time, which was obtained using the source acceleration; c) the average speed of 30 cm/s and 50 cm/s specified by two manufacturers. The average speed values provided by the manufacturers do not depend on the inter-dwell distance and may not refer to the speed between the dwell positions, depending on the measurement methodology, although these speed values can be used as reference values. Nucletron suggests dwell time corrections using an average speed of

50 cm/s for a 5 mm inter-dwell distance.¹³⁷ This dwell time correction was not considered for the evaluated clinical cases and was described in sections 4.6 and 5.5 (Speed measurements).

4.5.2 Validation

The MC source distribution for the clinical cases simulates the source at each position, which is equivalent to the superposition principle used to validate simulation results for simplified cases. While the studied cases were evaluated accounting for the anisotropy, scattering and other interactions, the validation process was performed using an isotropic point source and the superposition technique which can be verified with simple dose calculation algorithms. The validation process consists of three steps:

- a) speed profile verification by comparing the speed profile calculated using the TPS contour information and obtained analytically;
- b) MC simulation of the transit dose component versus a calculation using MATLAB for a treatment plan created for a point source and a linear 10 cm long catheter with dwell positions distributed uniformly along it for inter-dwell distances of 2.5 mm, 5.0 mm, 10.0 mm and 20 mm. This is illustrated in Figure 15 for a simplified case with 3 dwell positions;
- c) creation of a treatment plan for a ring applicator with 32 mm of diameter defined in the BrachyVision™ applicators library (ref: AL13017000) with inter-dwell distance of 0.5 cm used only to verify the source trajectory. The transit dose distribution was simulated considering the source instantaneous speed, and then exported back to the TPS as DICOM images allowing a visualization of the applicator and the dwell positions superimposed over the transit dose distribution.

The transit dose component for one reference point (Ref-1; Figure 15.a) was estimated considering a trajectory composed by N steps of $10\ \mu\text{m}$ with travel times calculated using a source instantaneous speed profile (Figure 15.b). The contribution of each step along the trajectory to the total transit dose at the reference point (Ref-1/ Figure 15.a) is proportional to the travel time of each step weighted by the square of the distance d' between the position of the center of the $10\ \mu\text{m}$ step and the reference point to take into account the inverse-square law resulting in the distribution presented in Figure 15.c. Finally, the transit dose component (D_{tr}) was obtained by integrating the obtained distribution and multiplying it by the dose rate (\dot{D}) for an arbitrary reference distance (d_{ref}) as described in the following

equation, which was used to validate the MC results obtained and to evaluate a possible correction.

$$D_{tr} = \dot{D} \cdot d_{ref}^2 \sum_{i=1}^N \frac{t_i}{d_i^2}$$

3

This approach considers only the square distance law, although it is a reasonable approach for a simple case validation since a point source was adopted to eliminate anisotropy functions and the scattered photons have a much smaller effect than the square law for positions close to the source.

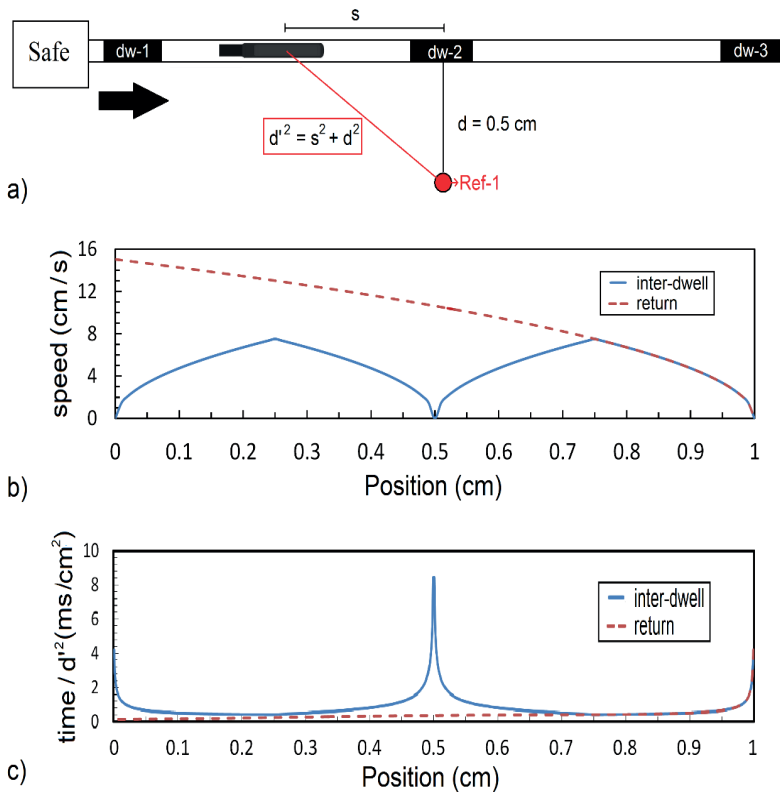


Figure 15. **a)** Source moving between three dwell positions with inter-dwell distance of 0.5 cm. **b)** Source speed profile for a uniform accelerated movement. **c)** Contribution of each source position to transit dose at the reference point due the source traveling between the dwell positions and returning to the safe.

4.5.3 Dwell time correction

The transit dose contribution to the total dose can be compensated by decreasing the dwell time, as currently applied by some manufacturers, using simple approaches that divide the inter-dwell travel distance by the average source speed reducing the dwell time up to 0.1 s per dwell position for the Nucletron afterloader, considering the travel time from the last position up to the current position as part of the dwell time for the GammaMed iX afterloader and using the following equation for the BEBIG afterloader⁴²:

$$pDT = (DT - T_{r(to\ dwell)} - T_{r(from\ dwell)}) \quad T_r = (cd_{id} + 100) \times 10^{-3} \quad 4$$

Where pDT is the corrected dwell time (s), DT (s) is the dwell time without correction and T_r (s) the correction time obtained using the inter dwell distance (d_{id}) in mm, considering the source coming to the dwell position (to dwell) and the source leaving the dwell position (from dwell), multiplied by a constant c (3 s.mm⁻¹ for inter-dwell distance less than or equal to 10 mm and equals 2 s.mm⁻¹ for greater distances) and adding 100 s. Equation 4 was adopted by Palmer et. al.⁴², but the methodology used to obtain this equation has not been described.

To the best of our knowledge there is no algorithm to correct the transit dose based on the instantaneous source speed that takes the acceleration (a) into account. In an attempt to reduce the transit dose effect, the transit dose (D_{tr}) was calculated for several inter-dwell distances (from 0.25 cm up to 10 cm) considering four reference points defined along a line orthogonal to the source longitudinal axis and at distances d (0.25 cm, 0.5 cm, 1cm and 2 cm) as illustrated for one reference point (Ref-1) in Figure 15.a. Finally, the correction time for the nearest dwell position to compensate the transit dose was calculated for each reference point leading to the following empirical equation:

$$T_c = \frac{1}{2} \cdot \sqrt{\frac{113}{a}} \cdot (T_{r'(to\ dwell)} + T_{r'(from\ dwell)} + T'_{return}) \quad 5$$

$$T_{r'} = +0.0261 \cdot \ln(d_{id}/d_{ref}) + 0.1241 \quad \text{for } d_{id} \leq 15 \text{ mm}$$

$$T_{r'} = +0.1355 \quad \text{for } d_{id} > 15 \text{ mm}$$

$$T'_{return} = -0.0011 \cdot (d_{lp}/d_{ref}) + 0.1220$$

where the correction time (T_c) in s, that should be subtracted from the TPS dwell time of the nearest dwell position. T_c depends on the reference distance (d_{ref}), 1 mm, the inter-dwell distances (d_{id}) in mm and the distance between the current and the last position (d_{lp}) in mm.

Equation 5 includes the source coming from the previous position or from the safe to the current dwell position, $T_{r'(to\ dwell)}$ in s. The latter is approximated as an inter-dwell distance of 100 mm, T_c also depends on the source going from the current position to the next dwell position, $T_{r'(from\ dwell)}$ in s, and the source returning to the safe, T'_{return} in s. The factor 1/2 was included since the transit time in one inter-dwell segment will be corrected for two consecutive dwell positions and the factor $(113/a)^{1/2}$ includes the acceleration effect since the time of each discrete step is inversely proportional to the square root of the ratio of the reference acceleration (113 cm/s^2) and the acceleration (a) as obtained from kinematics and evaluated for accelerations (a) between 10 cm/s^2 and 200 cm/s^2 to cover the literature data interval.

The described approach compensates the transit dose effect, includes the acceleration and preserves the simplicity of the manufacturer's approaches. Although our approach includes the acceleration component, as the currently available algorithms it cannot completely correct the transit dose due to the limited number and location of the dwell positions. Moreover, complex transit dose distributions may occur, e.g. due to different inter-dwell distances in the same setup and/or due to the geometry and the number of catheters.

4.5.4 Clinical cases

Two gynecological cases and one prostate case were planned for a microSelectron-HDR ^{192}Ir source⁷⁷ using the TG-43U1 dose while one prostate case was planned for a GamammedPlus source⁷⁶. These cases were selected to provide a general overview of the transit dose component since they differ considerably in the number of catheters, inter-dwell distance and geometry. Regardless of the differences between the source, all the cases were simulated using the microSelectron HDR source with the dwell times of each case scaled to an air-kerma strength of 40700 U in order to evaluate all cases under the same air-kerma strength and also to evaluate the worst case scenario since the transit dose is directly proportional to this parameter. Simulations were performed for two situations: a) an infinite water medium, which was created by adding at least 20 cm of water at each side of the body;¹³⁰ b) a heterogeneous medium composed of five materials, air (mass density $\rho =$

0.0012041 g/cm³), water ($\rho = 1.0$ g/cm³), adipose tissue ($\rho = 0.92$ g/cm³), muscle ($\rho = 1.06$ g/cm³) and cortical bone ($\rho = 1.85$ g/cm³) defined using Hounsfield units (HU) with compositions defined by the International Commission on Radiological Protection (ICRP-1975).¹³⁸ One density was specified for each material to assure that MCNP5 uses the same composition and density specified using ACUROS™, a grid based Boltzmann solver, which was used, in a parallel work, to validate the dose distributions without the transit dose. The cases were compared considering the 3D dose distributions and also by comparing doses at prescription points defined by the physician responsible for the case, since structure contours were not created for all the cases.

$D_{w,m}$ (dose to water in medium) values were obtained for all cases and only the values obtained for an infinite water phantom are presented, except when stated otherwise, since the transit dose component relative to the dwell dose is the same for all the conditions evaluated.

4.5.5 Gynecological cases

Two gynecological cases differing significantly in the number of needles and dwell positions were selected to evaluate the impact of the number of needles and their locations. The evaluated cases were: case a) a treatment performed with a hollow cylindrical vaginal applicator with an external diameter of 35 mm and a polysulfone wall of 4 mm with one 12 cm long needle in the center totaling 17 dwell positions, inter-dwell distance of 2.5 mm and a total dwell time of 405 s. The reference points were defined at a distance of 5 mm from the right hand side of the applicator wall with an average dose of 7 Gy; case b) a treatment performed with the same applicator described in the previous case using the central needle of the applicator and three needles distributed near the lower surface of the applicator totaling 100 dwell positions and a total dwell time of 556 s. Each needle has been defined during the treatment planning with approximately 12 cm of contour length and an inter-dwell distance of 2.5 mm. The reference dose points were defined on the right hand side of the applicator's surface with an average dose of 15 Gy.

4.5.6 Prostate cases

Two prostate cases were selected, which had approximately the same total dwell time and prescribed dose, but a significantly different number and distribution of the needles. The evaluated cases were: case c) a treatment performed using 16 flexible catheters with lengths defined through contours during the planning between 3.8 cm and 6.3 cm, the number of

dwell positions varying from 2 up to 8 depending on the catheter, and distances between active positions from 0.5 up to 2 cm totaling 113 dwell positions with a total dwell time of 200.9 s. The prescribed dose at the surface of the prostate was 10 Gy; case d) a treatment performed using 7 catheters with lengths defined through contours during the planning between 5.3 cm and 9.6 cm, number of dwell positions varying from 6 up to 8 depending on the catheter and inter-dwell distances of 0.5 cm and totaling 50 dwell positions with a total dwell time of 232.2 s. The prescribed dose at the surface of the prostate was also 10 Gy.

4.6 Speed measurements

Dwell times and source speed profiles were measured for a microSelectron v.3 ^{192}Ir source (Nucletron) using a Sony NEX-FS700 (Sony Corporation, Tokyo, Japan) video camera with 960 fps to register the source trajectory. Time resolution was assessed by recording a stopwatch display as (1.04 ± 0.01) ms.

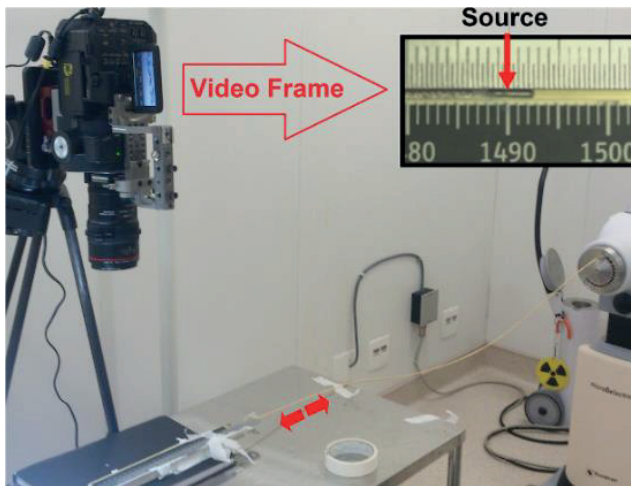


Figure 16. Experimental setup for source speed measurements. The insert (top-right) was obtained from one of the acquired slow motion videos. The source guide was positioned to be clinically relevant avoiding excessive bending during the experiments.

For this study, the trajectory of the source inside of a transparent channel aligned with 0.05/0.10 cm resolution rulers was recorded (Figure 16). The source trajectory was registered using: from 1 up to 18 dwell positions; inter-dwell distances of 0.25, 0.50, 1.00, 1.50, 2.50 and 5.00 cm; and source step sizes from 0.25 to 1.00 cm. The higher resolution ruler was used to calibrate the pixel width, $(3.78 \pm 0.04) \times 10^{-3}$ cm for most of the videos.

Source positions were evaluated frame-by-frame with in-house software developed using MATLAB version 8.0. The region of interest (ROI) that represents the source trajectory was manually assigned and then the pixel intensity profile, without the source, was recorded as the background profile (BG). Source structures (e.g. the tip and the welding) can be easily identified dividing the pixel intensity profile inside the ROI of each frame by the BG profile as illustrated by the top right figure in video 1.** This video shows the software used to track the source, the source movement and intensity profiles including reference lines, with fixed distances between them, associated with source structures. These lines were included to verify possible misdetections. Average speeds were calculated over three measurements.

All speed values were averaged over distance intervals of 0.2 cm ($\bar{v}_{0,2}$), except when otherwise stated. The dwell-time correction applied by the afterloader was measured for all setups by comparing the programmed dwell time against the dwell time recorded using the video footage. Dwell-times were measured after the source comes to rest at the specified dwell position.

The source trajectory between two consecutive dwell positions starts with the source leaving the first dwell position and ends immediately before the source reaching the second dwell position for the first time. We noticed that, after the source reaches a dwell position it overshoots and oscillates around it, an effect that was not considered for the average speed determination. The duration the source spends oscillating around a dwell position was measured.

4.6.1 Experimental uncertainty

Two types of uncertainties were adopted: Type A – standard deviation ($\pm 1\sigma$) of the results obtained repeating the experiments; Type B – defined as two pixels width and half of the time resolution. The uncertainty on the time is 5.2×10^{-4} s while the uncertainty on the source position is 7.56×10^{-3} cm. All speed values obtained over 0.2 cm intervals have an uncertainty component of 3.8% for the distance while the average speed over larger inter-dwell distances has a smaller relative uncertainty component for the distance. The uncertainty component due to the time resolution varies considerably due to the number of frames

** Videos available online: ftp://ftp.aip.org/epaps/med_phys/E-MPHYA6-42-018501

recorded within each interval and reaches up to 21% of the travel time for the highest speed value obtained. A source traveling with high speed therefore appears in fewer frames.

The uncertainty components were added in quadrature for the average speeds between dwell positions and other measured parameters described in the text whilst both components were separately shown in the figures so the reader can visualize the statistical variation and the setup uncertainty separately.

4.6.2 Transit dose calculation

The transit dose distribution due to the source traveling inside the catheter, without considering the dwell time correction, and the dose reduction due to the dwell time correction applied by the manufacturer were obtained separately using the MCNP6 MC code.^{22, 50} All cases were simulated for a microSelectron v.2 source model that was validated by simulating TG43-U1 parameters in a 30 cm diameter water phantom following the methodology proposed by Daskalov et al.⁷⁷ The simulations were performed with an infinite¹³⁰ water phantom to assure dose values equivalent to those obtained with the TG-43U1 dose to water formalism^{1, 2}, which was verified comparing simulated results obtained with one dwell position against dose values obtained with an air-kerma strength of 40800 U using a commercial treatment planning system, OncentraTM.

The dose correction was simulated using the measured dwell time corrections of each position. The source movement was simulated adding virtual dwell positions every 0.01 cm along the source trajectory, for which the dwell times correspond to the time spend by the source to travel through the 0.01 cm interval. The source speed profiles obtained were interpolated to reach the 0.01 cm resolution.

Dose distributions were scored, using a track length estimator tally, within cylindrical shells (0.1 cm thickness/width) concentrically positioned around the source trajectory with 0.5 cm radius. The simulations consider that the source movement starts and ends 15 cm before the first dwell position. Dose values were scored every 0.1 cm and all cases were simulated until an uncertainty component type A ($k=1$) of less than 0.5% was reached for all the evaluated points.

RESULTS AND DISCUSSIONS

Chapter 5

5 RESULTS AND DISCUSSIONS

5.1 AMIGOBrachy

AMIGOBrachy employs a user-friendly user interface, obviating any technical MCNP6 knowledge, thus considerably reducing the time necessary to process the treatment data and to perform a MC simulation. Figure 17 presents a few screenshots of AMIGOBrachy with the ImageView module, 3D images and dose distributions. As an example, a patient CT slice, a rendered organ and a few dose distributions are shown.

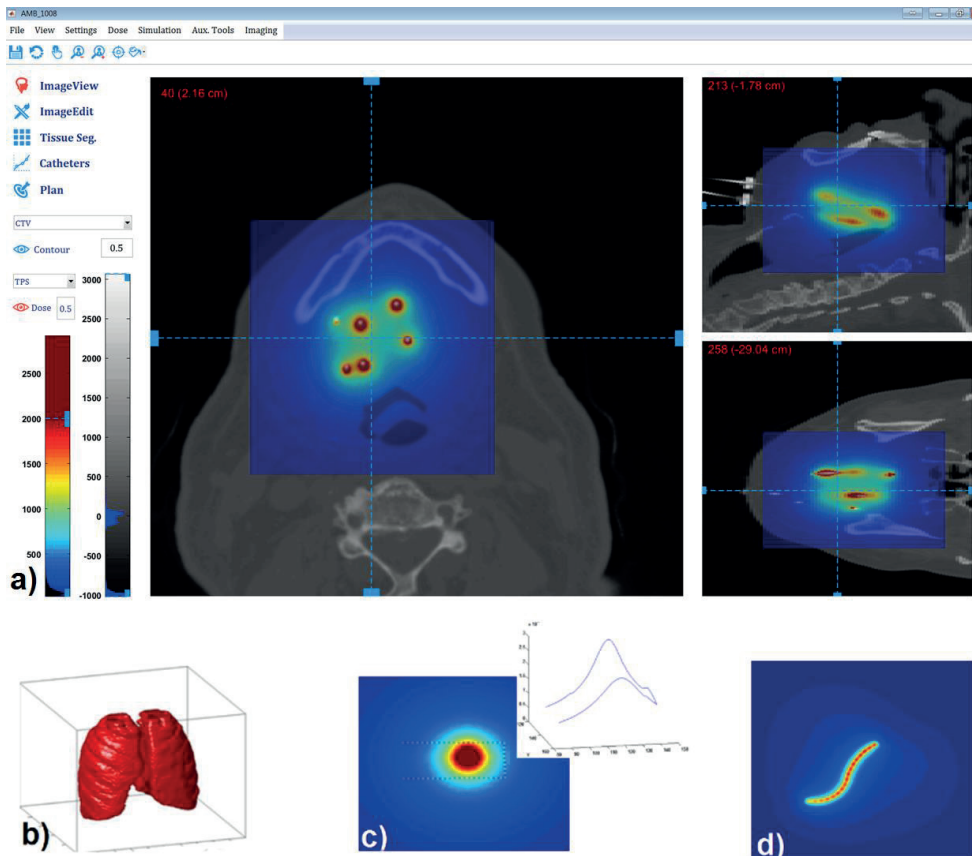


Figure 17. AMIGOBrachy screenshots of a) AMIGOBrachy ImageView module; b) 3D rendering of lungs; c) dose distribution of a single source dwell position with dose profiles; d) dose distribution obtained using a titanium fletcher applicator and a sequence of source dwell positions.

5.1.1 Uniform Phantoms Validation

Dwell positions in AMIGOBBrachy showed no differences from TPS values, indicating AMIGOBBrachy correctly imports the values from the TPS. Errors in the dwell positions were manually introduced, which led to clearly visible differences in the dose ratios even for positioning differences smaller than 0.5 mm. Therefore, source mispositioning problems can be easily detected. Calculated TG43-U1 parameters^{1, 2} for the source are in good agreement with literature parameters with most of the points showing less than a 1% dose difference. For GammaMed Plus more than 90% and 99% of the anisotropy function values show agreement with Taylor et al.⁷⁶ within 1% and 2%, respectively.

Results for the water cube phantom with AMIGOBBrachy/MCNP6 and ACUROSTM are in good agreement for all dose scoring grids. However, the agreement is affected by the scoring grid resolution since 95% of the voxel doses agree within 0.6, 1.0, 2.2 and 3.2% for scoring grid widths and heights of 5.0, 2.5, 1.0 and 0.5 mm. Uncertainty values are larger for smaller water voxel sizes since all simulations were performed with the same number of primary photons. In addition, ACUROSTM solves the Boltzmann transport equation by discretizing its six variables^{11, 18, 128} leading to some discretization artifacts that become visible with higher dose grid resolution. The mean dose per slice, obtained for statistic reasons, for the evaluated grid sizes were compared against the 1 mm³ grid. Differences lower than $\pm 0.2\%$ were observed for all.

Results obtained with phantoms of different materials (data not shown) were also compared using the mean dose per slice. The agreement between AMIGOBBrachy/MCNP6 and ACUROSTM is the same for all tissues with mean differences per slice within $\pm 0.3\%$ when compared against values obtained with a water phantom. The ratio of the mean dose per slice was visually evaluated and no systematic differences were found.

5.1.2 Clinical Cases Validation

The results obtained with AMIGOBBrachy/MCNP6 for both patient cases were in good agreement with the values calculated with ACUROSTM, with differences of less than 2% and 5% for more than 92% and 98% of voxels with doses higher than 10% of the prescribed dose, respectively. Larger differences were observed in regions with a dose below 10% of the prescribed dose, which were due to the statistical uncertainty of the simulation. Figure 18 shows the results obtained including a 3D CT view (top), the dose ratio between ACUROSTM

and MCNP6 (middle) and the dose ratio of MCNP6 for a homogeneous water medium and the proper material compositions (bottom).

The agreement between MCNP6 calculations for the intracavitary case performed using an applicator defined analytically and ACUROS™ is slightly lower than the agreement obtained using voxels for both codes with 87% of the voxels with differences below 2%. This is due to the differences in the gynecological applicator position and model since the analytical model of the applicator (MC) was compared against a voxel model. It was not possible to include the applicator in the ACUROS™ applicator database leading to different models, similar to the illustration in Figure 8 for another applicator.

The intracavitary case shows isodose displacements of about 1 mm and dose differences of around 5% in the region within the 100% isodose, which is mostly due to the hollow applicator effect since no significant difference was observed in the simulations modelling water or the actual tissue composition. The effect of the soft tissue composition and density is less than 1% for soft tissue, with no significant isodose displacement. The effect of the finite body dimensions is also visible in Figure 18.c1 showing increasing differences towards the boundaries of the body. This represents a lower dose obtained with MCNP6 since the air around the body reduces the number of backscattered photons, which is neglected by the TG-43U1 formalism.

The interstitial case also shows significant dose differences when MCNP6 is used with tissue heterogeneities and uniform water. Isodose displacements were obtained up to 1.6 mm and 4.1 mm for the 100% and 50% isodoses, respectively. Inside the 100% isodose the underdose using proper tissue composition is about 5% with differences increasing towards the outer surface of the arm. The effect of the soft tissue composition and density is less than 1%. The bone medium yields displacements of up to 4.0 mm in the 100% isodose at some points behind this material.

5.1.3 Clinical applicability

The simulation efficiency depends on the clinical case with potentially significant differences since the effects of LSTE and geometrical optimization can depend on the case and on the user-defined parameters. The size of the region that is voxelized (Figure 9.d) also influences both efficiency and accuracy.

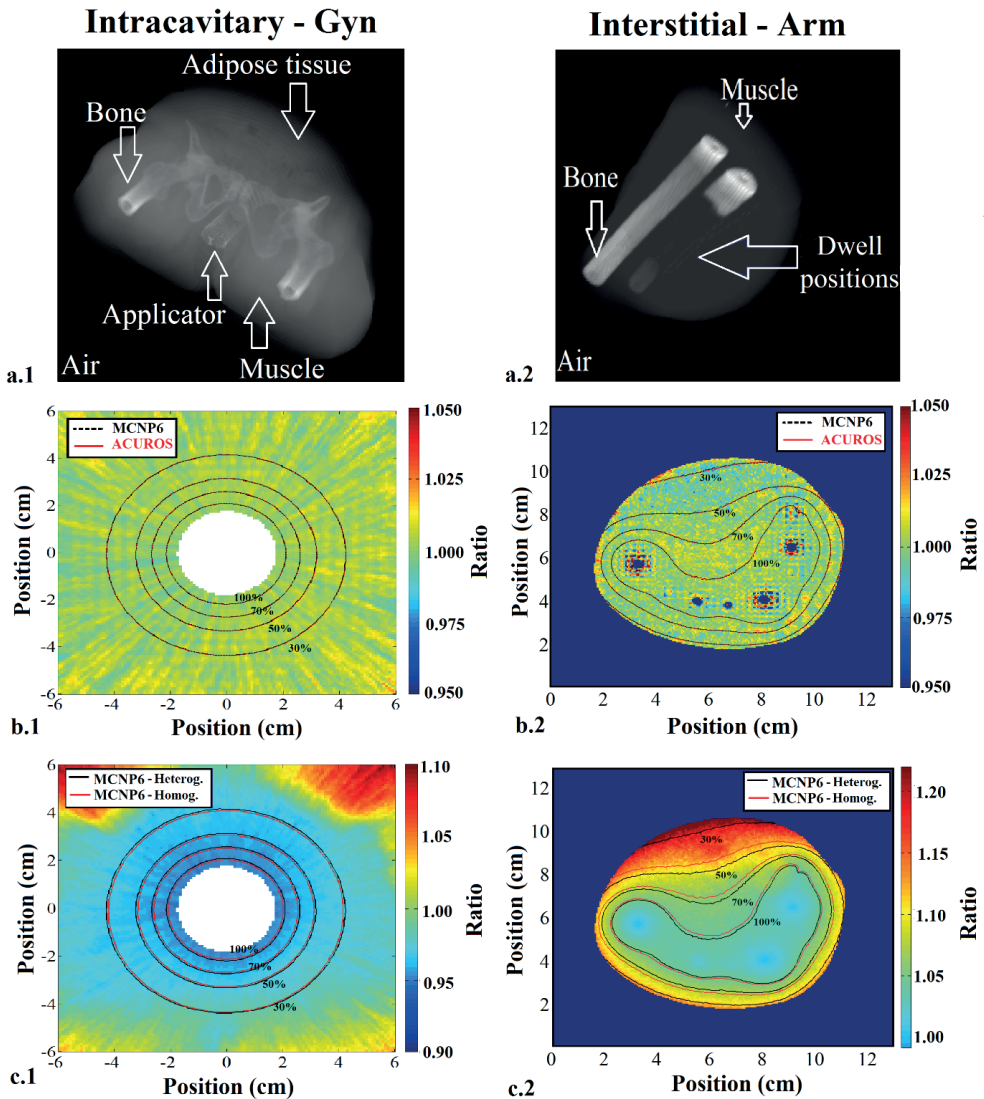


Figure 18. Results for the two patient geometries: the intracavitary gynecological case (left panels) and the interstitial arm case (right panels). **a)** 3D view indicating the assigned materials. **b)** Isodoses and dose ratio ACUROSTM/MCNP6. **c)** Isodoses and dose ratio MCNP6(homogeneous water)/MCNP6(heterogeneous geometry).

Simulations using the track length estimator tally (MCNP6 F6) with the LSTE function disabled required at least 100 times longer calculation times than those performed using FMESH (virtual grid based track length estimator tally) with the LSTE function activated. This result agreed with the LSTE description and was performed only for one case

to estimate the simulation time.¹³⁹ Simulation time for the gynecological case can also be reduced by up to 24% and the RAM memory requirements almost 100 times by defining the voxel phantom and the dose grid size. This can be done interactively with AMIGOBrachy or can simply be accepted from the treatment plan.

The feasibility of clinical implementation was evaluated by simulating the intracavitary case with 6.6×10^6 voxels assigned to specific materials, a dose scoring grid of $100 \times 100 \times 20$ voxels and a dose grid resolution of $(1 \times 1 \times 3)$ mm³. The simulation time necessary to obtain an average dose uncertainty of 2% inside of the 50% isodose region for 5×10^7 particles, using an Intel i7 (2860QM) processor with four cores of 2.5GHz and 8 Gb of RAM memory, is 69 min. On a more powerful Intel Xeon X5650 processor with twelve cores of 2.67GHz and 32 Gb of RAM the simulation time is 27 min, and this reduces to 5 min on a SGI C2112 server (Silicon Graphics International Corporation, Chippewa Falls, USA) consisting of 16 processors with eight cores of 2.4 GHz each.

MC dose calculation should initially be used to evaluate the differences with TG43-U1 treatment plans, providing valuable information regarding heterogeneity corrections. Besides dose evaluation AMIGOBrachy/MCNP6 can be used to calculate the mean photon energy in voxels, which can be useful for energy dependent dosimeter corrections or for studies on relative biological effectiveness.¹⁴⁰

5.2 CAD-Mesh

5.2.1 Water cube

The water cube represented by a MG model of 12 to 191514 elements yielded dose distributions which agreed with those obtained from CSG representation within 1%. Figure 19 shows calculation times for 10^7 primary photons from Geant4 and MCNP6 as a function of the number of elements in the MG. We observed that for MG with less than 10^4 elements Geant4 took approximately 1.5 times longer than MCNP6 with differences up to 3.5 times for the highest number of elements. Calculation times increased with the number of mesh elements for both codes. Above a threshold between 10^4 and 10^5 elements the Geant4 calculation time increased at a greater rate than MCNP6. It is currently not clear to us why Geant4 behaves this way, although it may be due to different tracking algorithms since MCNP6 creates a neighbor list at the beginning of the simulation, which may result in a more

efficient tracking algorithm at a cost of a longer time to process the input files at the beginning of the simulation.

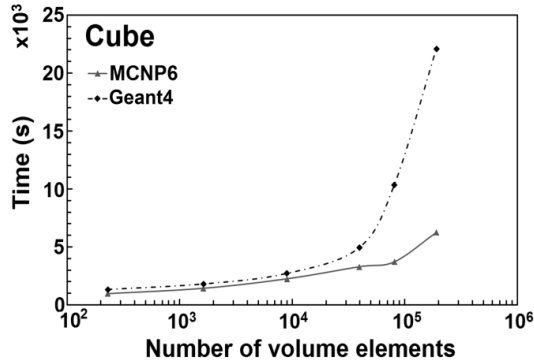


Figure 19. Calculation times in seconds for simulating 10^7 primary photons from an ^{192}Ir source in a water cube represented by a MG with varying number of volume elements.

5.2.2 Idealized APBI applicator

Our initial results showed a dose discrepancy in the region inside the idealized APBI applicator when using MCNP6 which was traced to the loss of photons scattered towards the interior of the balloon (Figure 20a) which caused an underestimation of the dose there. Hollow surfaces or gaps between different mesh parts may be treated as a void cell leading to missing particles since particles going towards this region may be eliminated. In this study this issue was corrected by filling the spherical shell with a mesh water sphere (Figure 20b).

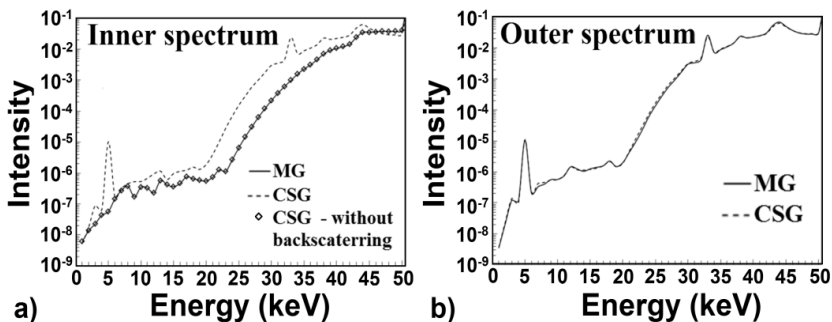


Figure 20. (a) Inside the balloon wall there appears to be a lack of backscatter from the balloon wall and the water beyond it in the MG case. (b) However, the photon spectra directly outside the balloon agree between MG and CSG.

Figure 21 presents the results for the 50 kV point source located at the origin of the idealized APBI balloon applicator. We observe agreement within 1% for the majority of the voxels between MG (using 4472 elements) and CSG representations of the geometry in Geant4 as well as good agreement between Geant4 and MCNP6 when using MG in both codes. Similar agreement was observed when using photon point sources of energies 20, 30, 40, 50 and 100 keV. Changing the number of elements in the MG from 4472 to 17824 and 69408 did not alter the results but yielded calculation times which were ~ 2 , ~ 3 and ~ 8 times longer when using Geant4 compared to the CSG representation.

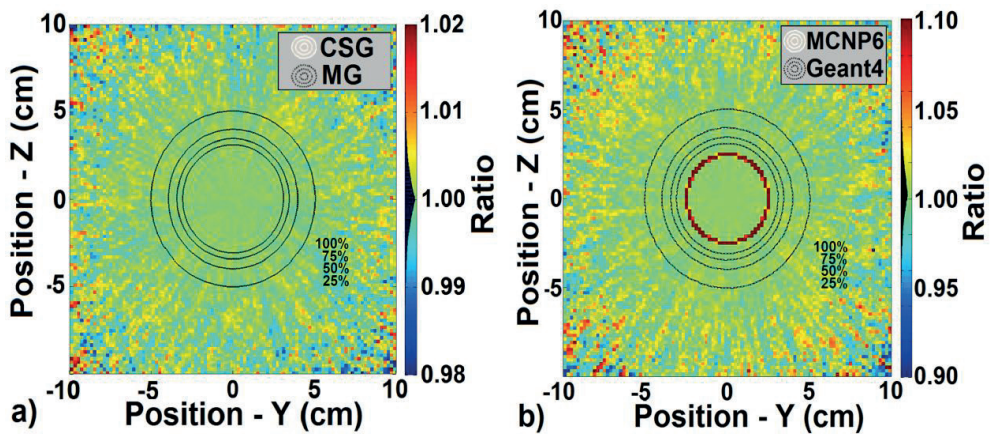


Figure 21. **a)** Dose ratio in an axial slice intersecting the origin from dose distributions obtained with MG and CSG representations of the idealized APBI balloon applicator using Geant4 and a 50 kV photon spectrum. Isodose lines are also presented. **b)** Dose ratio obtained using MG in Geant4 and MCNP6. Dose in the balloon wall was not scored in Geant4 hence the low values of the ratio. Isodoses overlap for (a) and (b) due to the small differences obtained. The first two colour maps show a histogram (black) of the distribution of values of the dose ratio over the whole phantom volume.

5.2.3 APBI balloon applicator

Figure 22 presents similar results as above for the irregular APBI balloon applicator defined from TPS contour points representing the balloon geometry during a clinical case irradiation. Agreement within 1% is observed within the 25% isodose surface between Geant4 and MCNP6. The MG contained 5195 tetrahedrons. This irregular balloon cannot be easily modelled using CSG geometries.

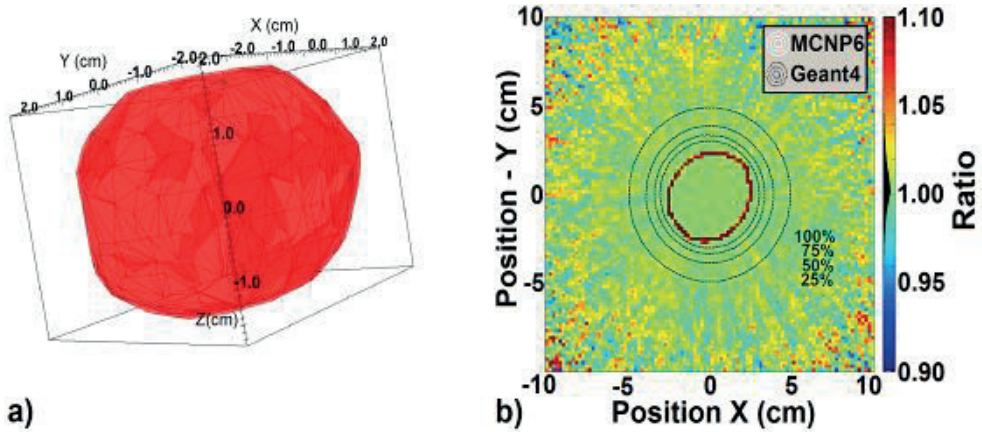


Figure 22. **a)** The MG of the irregular balloon. **b)** Axial plot of dose ratios obtained from MCNP6 and Geant4 using the MG of the balloon and a 50 kV photon point source. Isodose lines are also presented. Dose in the balloon wall was not scored in Geant4 hence the low values of the ratio. The color map shows a histogram (extreme right) of the dose ratio distribution over the whole phantom volume.

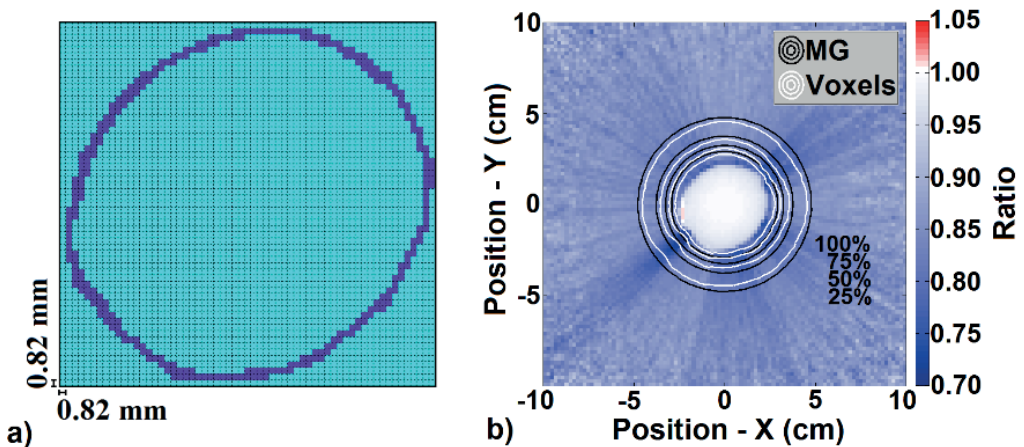


Figure 23. **a)** APBI balloon applicator wall represented by voxels. **b)** Axial dose ratio obtained from MCNP6 using the voxel and MG models of the balloon.

Figure 23 shows a voxelized APBI balloon applicator slice and the dose ratio between the results obtained with voxels and with MG. Differences of up to 30% were observed due to the low geometric accuracy of the voxel model whose resolution exceeds the balloon thickness by a factor of 2 and 5 for the voxel width/height and for the slice thickness, respectively. Moreover, the balloon wall may be represented by more than one voxel

depending on the region. A more accurate model could be obtained with higher resolution voxels, which was not evaluated in this work since irregularly shaped mesh elements provided an optimal geometry representation validated against CGS models.

5.2.4 Shielded HDR vaginal applicator

Figure 24 shows the results of comparing dose distributions obtained from Geant4 and MCNP6 using both MG (two levels of refinement) and CSG representations of the shielded vaginal applicator. In general the agreement between Geant4 and MCNP6 and between MG and CSG are within 1% as shown. When using the MG representation with more elements some artefacts were observed in the dose distribution from MCNP6 (Figure 24c, aft of applicator) which were traced to lost particles in the simulation. With mesh geometries there is a possibility of overlapping tetrahedrons and/or void gaps between the tetrahedrons. A certain degree of overlap is accepted by both codes, however MCNP6 may kill some particles due to complete or substantial overlaps or gaps leading to results as shown in Figure 20. Geant4 prints a track stuck warning and shifts the particle by a small displacement and keeps tracking. We verified that only a low fraction of simulated particles caused track stuck warnings to be printed. No killed track messages were observed in Geant4. In addition, Geant4 warning messages can be used to track the geometry problems as they provide information on the tetrahedron responsible for the stuck track. Stuck tracks were not observed in the CSG model. Increasing the number of elements again caused longer simulation times and may not result in a higher accuracy since higher number of elements does not assure the absence of overlaps or gaps. Figure 25 shows the simulation time for 10^7 primary photons using a different number of elements in the shield for both codes. Again Geant4 requires longer calculation times than MCNP6.

5.2.5 Shielded HDR Fletcher Williamson applicator

Figure 26 presents the result of Geant4 and MCNP6 MG simulations of the shielded Fletcher Williamson applicator. We observed agreement within 1% between the dose ratios of both codes, except for differences up to 8% observed at some points close to the bottom of the applicator and far from the dwell positions.

The agreement observed between MCNP6 and Geant4 MG models was also obtained between a CSG and a MG model obtained for the same applicator with lateral channels

rotated 4.5 degrees to align with the central channel as shown in Figure 27. Most of points are within 1% with maximum difference of 4.1%.

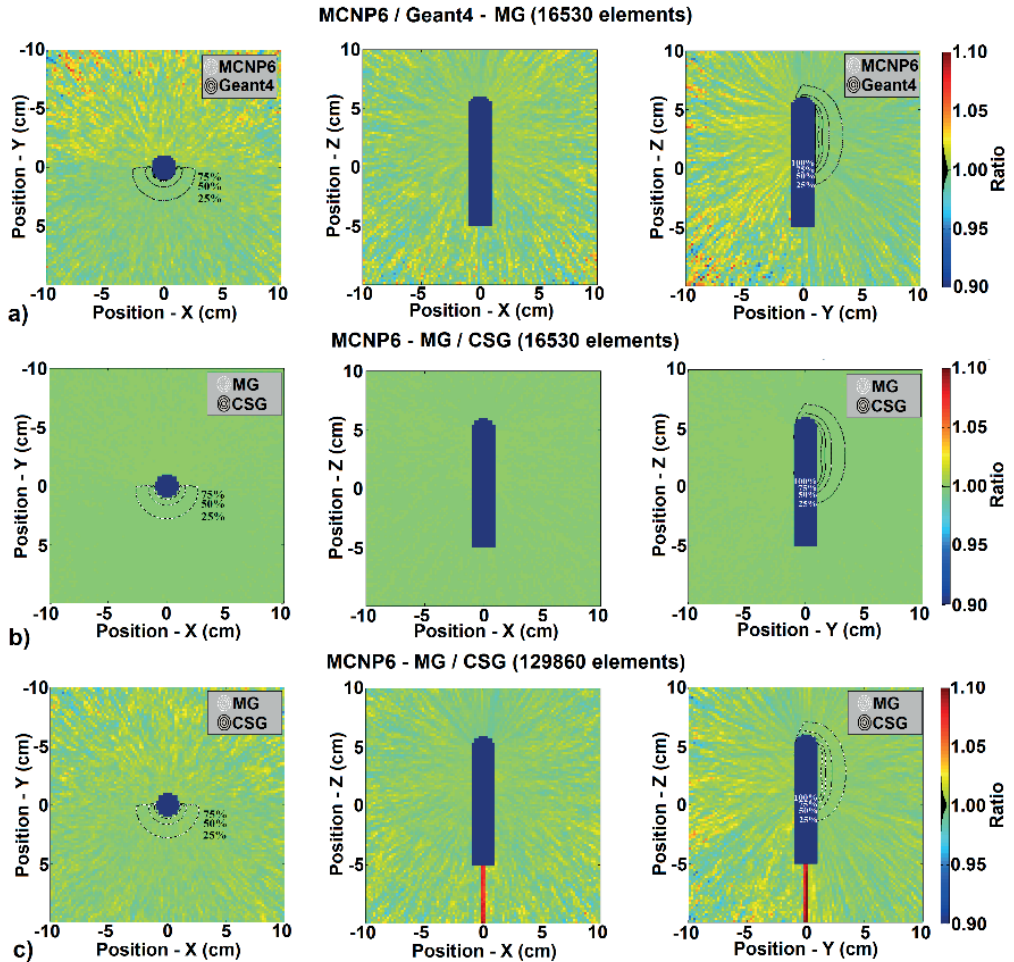


Figure 24. **a)** Dose ratio in central axial, coronal and sagittal slices from Geant4 and MCNP calculations of the dose distribution from the shielded HDR vaginal applicator represented with MG containing 16530 elements. **b)** The dose ratio when representing the applicator with a MG of 16530 elements in MCNP and a CSG representation. Differences are not visible in these figures (**b**) since most of the results are within 0.5% with maximum difference around 1%. **c)** Dose ratio between MG and CSG applicator models in MCNP using 129860 elements for the MG. Isodoses inside of the applicator were not shown.

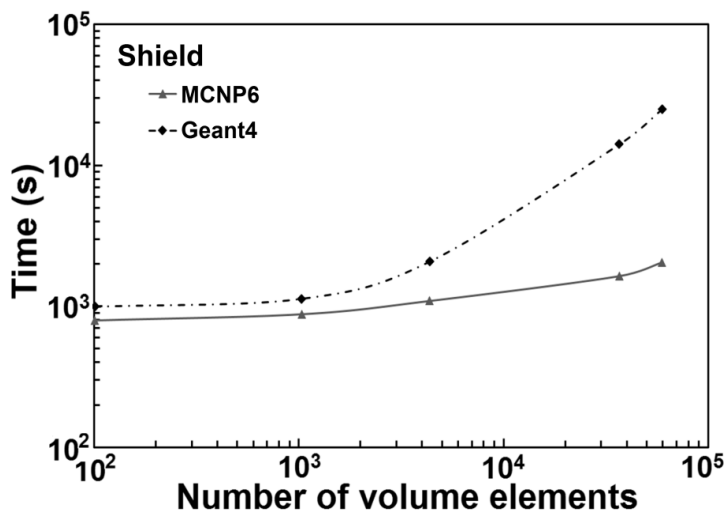


Figure 25. Calculation times in seconds for 10^7 primary photons from an ^{192}Ir source with the W shield from the vaginal applicator represented by a MG with varying number of volume elements.

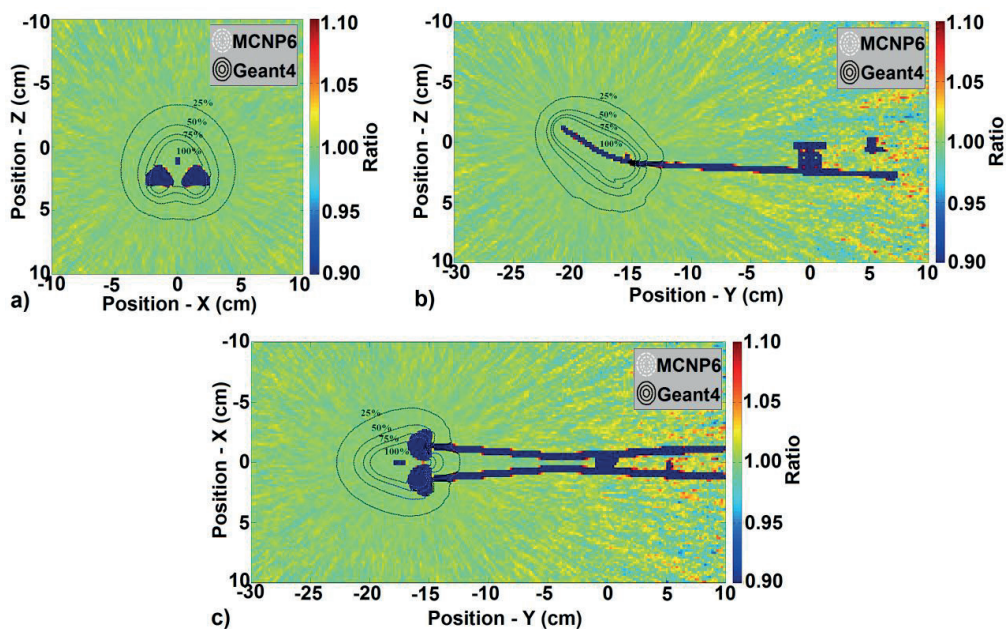


Figure 26. Dose ratios between Geant4 and MCNP6, using MG models. **a)** Axial slice. **b)** Sagittal slice of the dose ratio. **c)** Coronal slice. Isodose lines from both codes are also plotted.

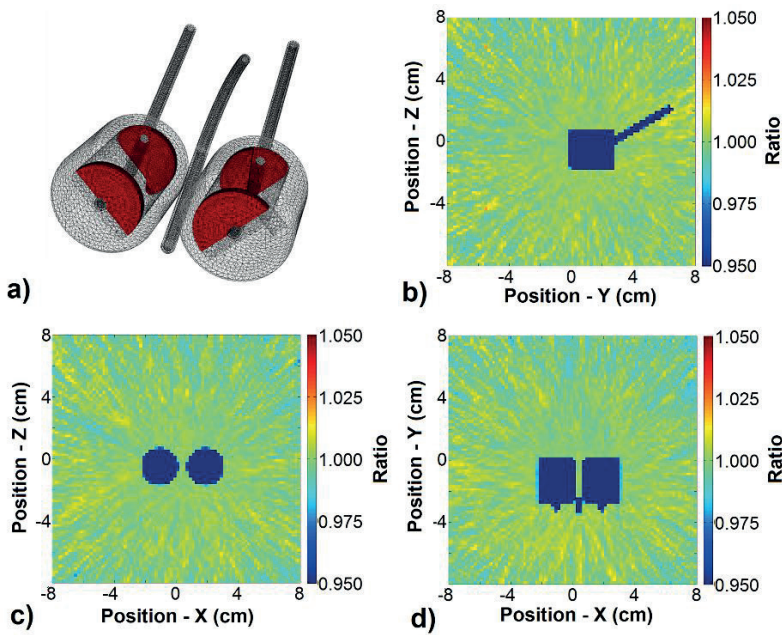


Figure 27. **a)** MG representation of the shielded Fletcher Williamson applicator used for validation purposes. The MG geometry was exported by MCNP6 as an output file ¹¹⁷. Ratio between MCNP6 (CSG) and Geant4 (MG): **b)** sagittal slice of the dose ratio; **c)** axial slice; **d)** coronal slice.

5.3 Dose specification

5.3.1 Mean photon energy

Mean photon energies obtained using segmented tissue compositions and mass densities from a calibrated CT image (phantom III) are shown in two planes of the head and neck geometry in Figure 28 (a-b). Histograms of the number of voxels as function of mean energy were obtained for the three phantom models, considering the whole CT-defined patient volume excluding regions with air (Figure 28.c). The mean photon energy distribution ranges from 222 keV up to 356 keV.

Small differences in mean energy are observed between the three phantoms (Figure 28.c). A mean energy shift towards lower photon energies of approximately 1.3% was observed for the simulation of phantom II compared to phantom I (Figure 28.c) while hardly any difference could be observed between phantoms I and III. Figure 29 shows the local mean photon energy ratios to investigate this further

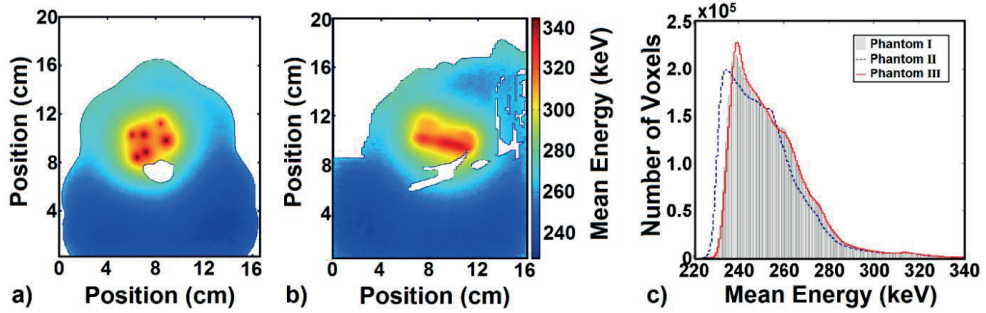


Figure 28. Axial (a) and sagittal (b) spatial distribution of the mean photon energy distribution for the evaluated head and neck case and mean energy–volume histograms (c) for all voxels scored over the whole CT volume, excluding air voxels. Uncertainty $<4\%$ for all voxels (Type A $\pm 1\sigma$).

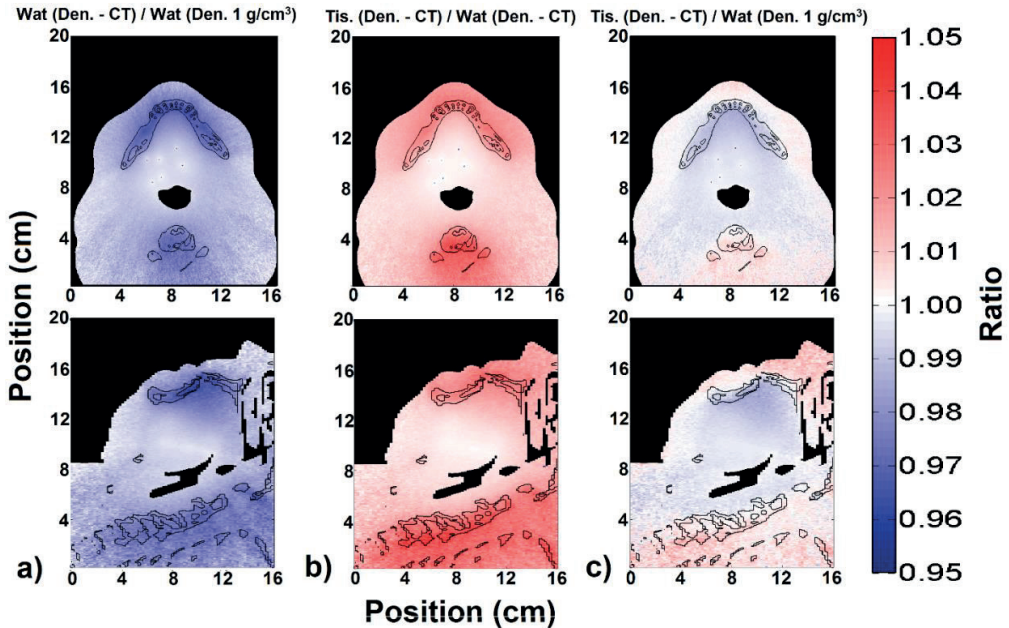


Figure 29. Axial and sagittal view of the mean photon energy ratio: a) phantom II over phantom I. This shows the density effect since both phantoms consist of only water; b) phantom III over phantom II. This shows the composition effect since all voxels have the same mass densities; c) phantom III over phantom I. This shows the atomic number and density effects that approximately compensate each other. Contours in black represent bone tissue.

The phantom II has a mean mass density of $(1.04 \pm 0.03) \text{ g/cm}^3$ ($\pm 1\sigma$), excluding air regions, and a maximum mass density of 2.9 g/cm^3 . Higher mass densities resulted in a shift towards lower energies when compared against phantom I (Figure 29.a). On the other hand, bone chemical composition acts as a photon fluence hardener (due to higher Z components) by the higher preferential absorption of low energy photons due to the photo-electric effect. This can be seen in the regions behind the bone (III) in Figure 29.b, which have higher mean photon energies than the ones obtained using a water (II) with the same mass densities. The photon fluence hardening effect compensates, for this specific case, the effect produced by higher mass densities leading to small mean energy differences between the results obtained for phantoms I and III (Figure 28.c and Figure 29.c).

5.3.2 Photon spectrum

The photon spectrum emitted from the stainless steel source capsule (averaged over all angles of a single source) and the photon spectrum at two evaluated voxels for which the minimum (P13) and the maximum (P9) mean photon energy values were obtained are shown in Figure 30.

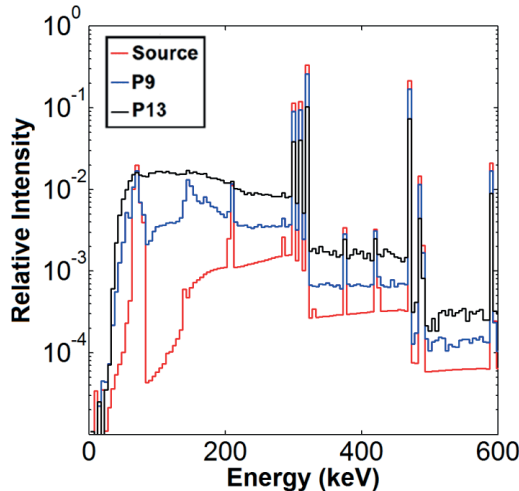


Figure 30. **a)** Photon spectrum emitted from the stainless steel capsule (averaged over all angles of a single source) and at two evaluated voxels, P9 and P13. Values were normalized for the total fluence in their respective voxel and grouped using 5 keV energy bins. Most of the photons from the source are concentrated on the peaks of the spectrum that represent the primary photons. Only values between 0 and 600 keV were displayed to highlight differences in this region.

P9 is inside the target volume at 0.4 cm from the nearest dwell position and at an average distance from the dwell positions of 1.4 cm whilst P13 is at 7.1 cm from the nearest dwell position and at an average distance from the dwell positions of 8.5 cm with a dose rate approximately 45 times smaller than at P9. The photon spectra for P13 obtained with the three phantoms are very similar showing hardly any visible differences in the low energy range due to the higher absorption of low energy photons by bone with phantom III.

5.3.3 CPE conditions

$D_{m,m}$ values obtained using a track length estimation tally show good agreement with values obtained using a pulse height tally with no systematic differences. Therefore, CPE can be assumed and the track-length estimator considered to be accurate for the voxel dimension $0.39 \times 0.39 \times 2.00 \text{ mm}^3$ used here. The mean of the ratio between the dose distribution obtained using F6 and F8, is 1.000 ± 0.013 (1σ) indicating that differences are due to statistical noisy. The maximum simulation uncertainty is $<1\%$, Type A $\pm 1\sigma$, for all values obtained with a track length tally and are up to 4.5% for the pulse height tally. The simulation time for the latter, necessary to obtain uncertainty values equivalent to the ones obtained using track-length scoring, would be around 1000 times longer when including electron transport without variance reduction techniques. All the results described below were obtained using a track length tally.

5.3.4 $D_{m,m}$ and $D_{w,m}$

The results obtained for some tissues (prostate, breast, skin, bladder, cartilage) were not described for brevity since they do not differ significantly from the ones obtained with muscle and adipose tissue.

5.3.4.1 $D_{w,m}$ (SCT)

$D_{w,m}$ (SCT) values were calculated by multiplying the $D_{m,m}$ simulated results by the values shown in Table 3. An energy-spectrum averaged value is a good approach since $(S_{col}/\rho)_w^m$ vary slowly as function of electron energy; for bone it goes from 0.868 up to 0.888 for monoenergetic sources with 20 keV and 300 keV, respectively (Figure 1.b). Such small differences indicate that average values can be employed without significant added uncertainties, see also Figure 1.b.

Table 3. The conversion coefficients from $D_{m,m}$ to $D_{w,m}(SCT)$ obtained using average mass stopping power ratios for some materials evaluated in this study.

	Lung	Adip. Tissue	Muscle	Mandible	Bone	Teeth
$(S/\rho)_w^m$	0.992	1.020	0.992	0.963	0.883	0.853

5.3.4.2 $D_{w,m}(LCT)$

Unlike $D_{w,m}(SCT)$ results, ratios between $D_{m,m}$ and $D_{w,m}(LCT)$ vary significantly with the photon spectrum and hence with position in the patient/phantom, in particular for some materials. Figure 31 shows the ratio between $D_{m,m}$ and $D_{w,m}(LCT)$ obtained for the clinical case. Ratios are approximately constant for adipose tissue and muscle, with a small dependence on the photon spectrum of each voxel. Differences can be significant for regions assigned as bone tissue with dose ratios ranging from 1.00 up to 1.14 (maximum difference observed in a voxel not shown in Figure 31).

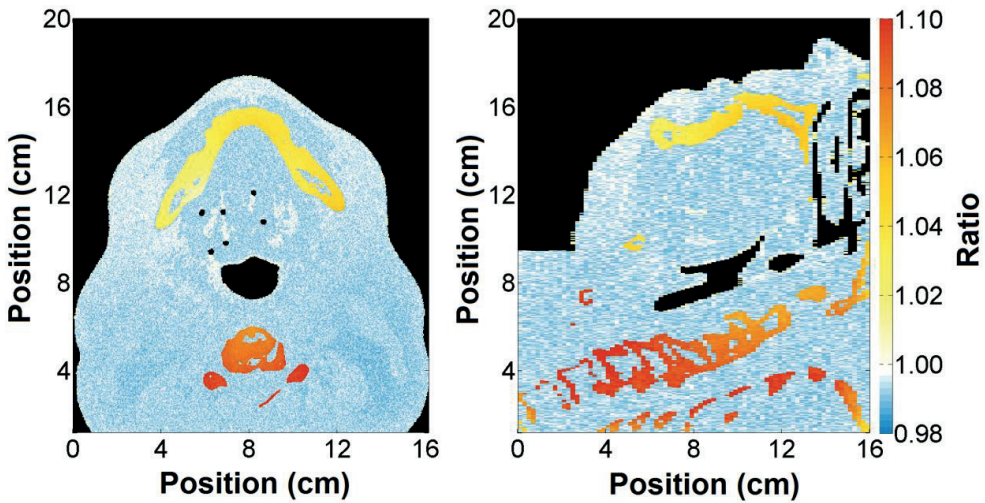


Figure 31. Ratio ($D_{m,m} / D_{w,m}(LCT)$) obtained using a track length estimator tally. Uncertainty $<1\%$ for all points inside of the CT volume (Type A $\pm 1\sigma$). Regions with air were excluded.

Variations in the photon spectrum may lead to differences between $D_{m,m}$ and $D_{w,m}(LCT)$ for the same material of up to $>15\%$, as shown in Table 4 while for $D_{m,m}$ and $D_{w,m}(SCT)$ the ratios are nearly invariant (see Table 1 and Figure 1b). Different phantom models for the same patient also lead to small differences, due to the slightly smaller low photon energy intensities for phantom III. Although differences in the photon spectrum are

not clearly visible for the voxel P13, the ratio $D_{m,m}$ and $D_{w,m}(LCT)$ for bone is 1.121, 1.142 and 1.106 for phantoms I, II and III, respectively.

Table 4. Ratio between $D_{m,m}$ and $D_{w,m}(LCT)$ obtained with the photon spectrum and with the mean photon energy scored (phantom III) for the 25 evaluated voxels (Figure 14). The minimum and the maximum values of each column are underscored. Mandible corresponds to mandible spongiosa from ICRP Report 110¹²⁹. Uncertainty is <1% for all dose ratios (Type A $\pm 1\sigma$). $D_{m/w}$ indicates $D_{m,m}/D_{w,m}$ -LCT.

Point	MeanE. (keV)	Adip. Tissue		Muscle		Mandible		Bone		Teeth	
		$D_{m/w}$	$D_{m/w}$	$D_{m/w}$	$D_{m/w}$	$D_{m/w}$	$D_{m/w}$	$D_{m/w}$	$D_{m/w}$	$D_{m/w}$	$D_{m/w}$
		Spec.	MeanE	Spec.	MeanE	Spec.	MeanE	Spec.	MeanE	Spec.	MeanE
1	268	0.995	0.999	0.991	0.991	1.009	0.985	1.041	0.968	1.069	0.968
2	266	0.994	0.999	0.991	0.991	1.010	0.985	1.045	0.969	1.075	0.970
3	268	0.995	0.999	0.991	0.991	1.009	0.985	1.042	0.968	1.071	0.968
4	274	0.994	1.000	0.991	0.991	1.010	0.984	1.045	0.964	1.075	0.964
5	267	0.994	0.999	0.991	0.991	1.010	0.985	1.046	0.968	1.076	0.969
6	277	0.995	1.000	0.991	0.991	1.007	0.983	1.035	0.963	1.061	0.962
7	280	0.995	1.000	0.991	0.991	1.005	0.983	1.029	0.961	1.053	0.959
8	295	0.996	1.000	0.991	0.991	1.001	0.980	1.015	0.953	1.033	0.948
9	<u>323</u>	<u>0.998</u>	<u>1.001</u>	0.991	0.991	<u>0.994</u>	<u>0.979</u>	<u>0.990</u>	<u>0.947</u>	<u>0.999</u>	<u>0.940</u>
10	300	0.996	1.001	0.991	0.991	1.002	0.979	1.017	0.950	1.036	0.944
11	263	0.993	0.999	0.991	0.991	1.015	0.986	1.064	0.971	1.101	0.972
12	244	0.991	0.999	0.991	0.991	1.025	0.989	1.096	0.982	1.144	0.988
13	<u>239</u>	<u>0.990</u>	<u>0.998</u>	0.991	0.991	<u>1.027</u>	<u>0.990</u>	<u>1.106</u>	<u>0.985</u>	<u>1.158</u>	<u>0.992</u>
14	276	0.995	1.000	0.991	0.991	1.006	0.984	1.031	0.963	1.055	0.962
15	268	0.995	0.999	0.991	0.991	1.009	0.985	1.042	0.968	1.071	0.968
16	282	0.996	1.000	0.991	0.991	1.004	0.982	1.024	0.960	1.046	0.958
17	265	0.994	0.999	0.991	0.991	1.012	0.985	1.054	0.970	1.087	0.971
18	281	0.995	1.000	0.991	0.991	1.006	0.983	1.033	0.961	1.058	0.959
19	271	0.994	1.000	0.991	0.991	1.011	0.984	1.050	0.966	1.081	0.966
20	283	0.995	1.000	0.991	0.991	1.007	0.982	1.034	0.959	1.060	0.957
21	265	0.993	0.999	0.991	0.991	1.016	0.985	1.068	0.970	1.106	0.971
22	267	0.994	0.999	0.991	0.991	1.014	0.985	1.059	0.968	1.094	0.969
23	245	0.992	0.999	0.991	0.991	1.023	0.989	1.090	0.981	1.137	0.987
24	246	0.992	0.999	0.991	0.991	1.023	0.989	1.089	0.981	1.135	0.986
25	240	0.991	0.999	<u>0.992</u>	0.991	1.026	0.990	1.100	0.984	1.150	0.991

The ratio between $D_{m,m}$ and $D_{w,m}(LCT)$ values obtained using the full photon spectrum and the mean photon energy, as a function of the mean photon energy in each one of the 25 selected voxels (Table 4), is shown in Figure 32. The ratio between $D_{m,m}$ and

$D_{w,m}(\text{SCT})$ is approximately constant and was added for illustrative purposes. The ratio $D_{w,m}(\text{SCT})/D_{m,m}$ for teeth is approximately 0.853 whilst the value of $D_{w,m}(\text{LCT})/D_{m,m}$ is up to 1.158 which represents the largest difference observed for the evaluated points.

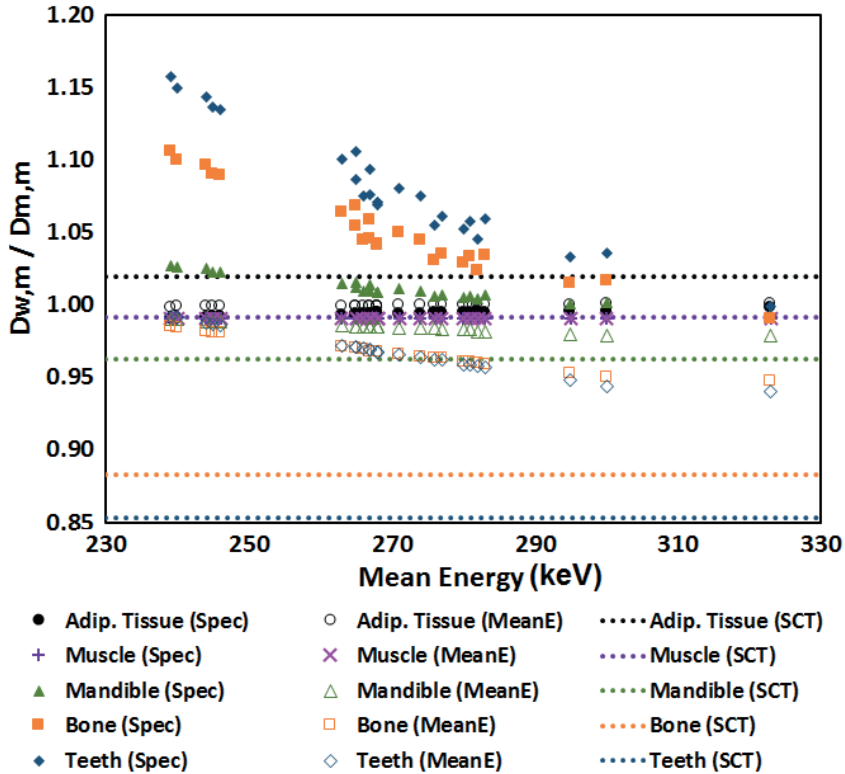


Figure 32. Ratio between $D_{m,m}$ and $D_{w,m}(\text{LCT})$ values presented in table 2. Values obtained using SCT, dotted lines, were added.

The ratio between $D_{m,m}$ and $D_{w,m}(\text{LCT})$ varies considerably over the patient volume for some materials due to the photon fluence softening (energy decrease) with distance from the source that increases the number of low energies photons for which values $(\mu_{en}/\rho)_W^m$ are more relevant. The contribution from low energy photons to the total dose is more relevant in some regions (Figure 33), with less than 6% of the total dose coming from energies less than 100 keV for all materials at P9. This fraction increases for all materials at P13 reaching up to 17.6% of the total dose for teeth. Muscle, adipose tissue, and water showed a similar behavior with the dose contribution from photons with energies lower than 100 keV increasing around 3.5 percentage points between P9 and P13 whilst it increased 5.7, 9.9 and 11.6 percentage points for mandible spongiosa, bone and teeth, respectively.

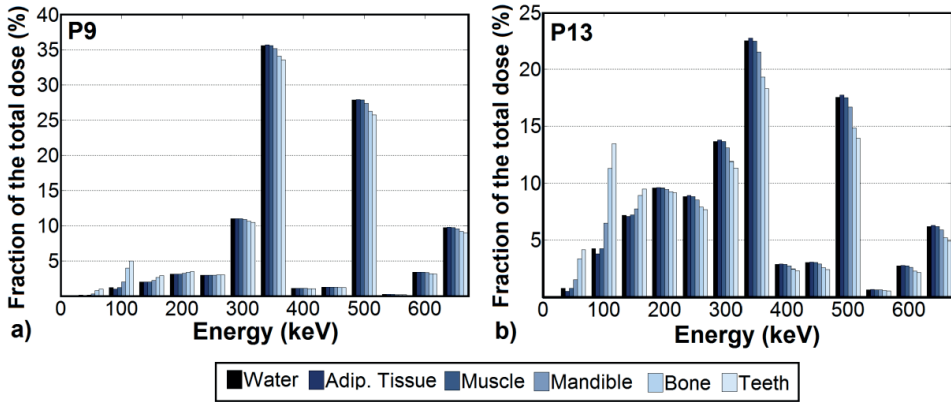


Figure 33. Contribution of various parts of the photon spectrum to the total dose at two evaluated voxels, P9 and P13. Photons with energies greater than 650 keV contribute less than 0.3% of the total dose. Uncertainty $<1\%$ for the total dose (Type A $\pm 1\sigma$).

5.3.5 Discussion

The mean photon energies illustrate the effect of the different phantom models employed for the same patient due to beam softening or hardening (Figure 29). Mean photon energy differences due to the three different phantoms adopted are within $\pm 5\%$ and would not result in significant differences in conversion factors between $D_{m,m}$ and $D_{w,m}$ (LCT) for the mean energy range (226-356 keV). However, these values should not be employed to obtain conversion factors between $D_{m,m}$ and $D_{w,m}$ (LCT) since mean photon energy values may lead to wrong results (Table 4) for some tissues (e.g. mandible spongiosa, bone and teeth).

The correct tissue and mass density assignment is relevant since small differences in the low energy photon intensities can lead to significant differences in the $D_{m,m}$ and $D_{w,m}$ (LCT) values for some materials (Figure 31). Although tissue segmentation is necessary to obtain $D_{w,m}$ values, a simpler approach using a water phantom with densities from CT (phantom II) may provide results on $D_{w,m}$ (LCT) and $D_{m,m}$ in the case of soft tissues similar to those obtained using tissue proper composition (phantom III). The three different phantoms produced very similar photon spectra. The mean of the ratios between $D_{w,w - \text{phantom II}}$ and $D_{w,w - \text{phantom III}}$ is 0.9980 ± 0.0002 (1σ) within the CT volume. A similar approach used for high energy (4-18 MV) photon beams showed that water with relative electron mass

densities of tissues produces $D_{w,w}$ values much closer to $D_{m,m}$ values obtained with MC codes than values converted using mass stopping-power ratios³⁰. This result is associated to Compton scattering, which is the dominant mode of interaction for EBRT energies and depends mainly on the electronic density of materials³⁰. For the ^{192}Ir photon spectrum Compton scattering is the most frequent interaction type for all human tissues at most of the energies encountered in the current patient geometry. However, the percentage of low energy photons may be more significant in some regions (Figure 33) increasing the occurrence of photoelectric effect for which tissue composition (high atomic number materials e.g. bone and teeth) is relevant. It explains the small differences between $D_{w,m}$ and $D_{m,m}$ (LCT) for soft tissues in all regions and differences varying with the photon spectrum at each voxel for some tissues as bone and teeth (Table 4).

Different approaches (SCT or LCT) can lead to equivalent results or relevant differences in $D_{w,m}$. The SCT and LCT approaches are almost equivalent for some tissues as muscle for which the conversion factors is 0.992 (SCT – Table 3) and 0.991 (LCT – Table 4). However, differences are significant for some tissues as adipose tissue and bone (Figure 34). Conversion factors for adipose tissues (LCT) range from 0.990 to 0.998 whilst the SCT conversion factor is 1.020 so the ratio (LCT/SCT) is between 0.97 and 0.98 depending on the photon spectrum. The ratio between conversion factors (LCT/SCT) for bone shows wider range ranging from 1.13 up to 1.28 and up to 1.36 for teeth. Large differences observed for some tissues (mandible spongiosa, bone and teeth) are expected since $(\mu_{en}/\rho)_w^m$ is greater than 1 (for low energy photons) for these materials whilst $(S/\rho)_w^m$ is less than 1 for the same materials (Figure 1). These differences make it essential to compare dose distributions with the same reporting quantity, which must be taken into account for different treatment modalities. SCT is commonly employed in EBRT and the LCT adoption for brachytherapy would lead to dose differences due to the reporting quantity. In head and neck cases, dose to the bony mandible is often of interest as this is considered an organ at risk. Great caution in which dose quantity is reported and how to compare dose values with earlier clinical experience is of the utmost importance in this and similar cases.

The correct tissue segmentation is necessary to calculate correction factors between $D_{m,m}$ and $D_{w,m}$ since miss-assignments can lead to differences, e.g. assignment of muscle to adipose tissue voxels leads to a 3% difference and even higher differences for bone or a few other tissues (SCT - Table 3). Therefore, converting $D_{m,m}$ into $D_{w,m}$ involves additional uncertainties.

Cavity theory based conversion factors are also relevant for experimental dosimetry. The signal from a detector depends on the absorbed dose to the detector material which may need to be taken into account if a detector has been calibrated for $D_{w,w}$ in another beam quality than that used for measurements (like calibration in ^{60}Co or 6 MV which is recommended in TG43^{1,2} for measurements around brachytherapy sources). The effect of different photon spectra on the dosimeter is also a relevant issue and was the subject of several studies with different dosimeters, e.g. termoluminescent dosimeters (TLD)^{96, 141, 142}, due to their intrinsic response, and MOSFETs^{127, 143, 144}, due their composition. Differences around 100 keV in the mean photon energies due to medium attenuation for a ^{192}Ir source can represent an over response around 60% for MOSFET dosimeters.¹⁴⁴ The MOSFET detector is of interest for clinical routine measurements due to convenience in handling and their fast, direct reading results. The problem of their large energy-dependence could be overcome by scoring the photon energy spectrum at the dosimeter positions during in-vivo measurements (similar to the 25 reference points evaluated in this study), thus accounting for all dwell positions, different densities and tissue composition. This way, more accurate energy correction factors would be obtained for energy dependent dosimeters.

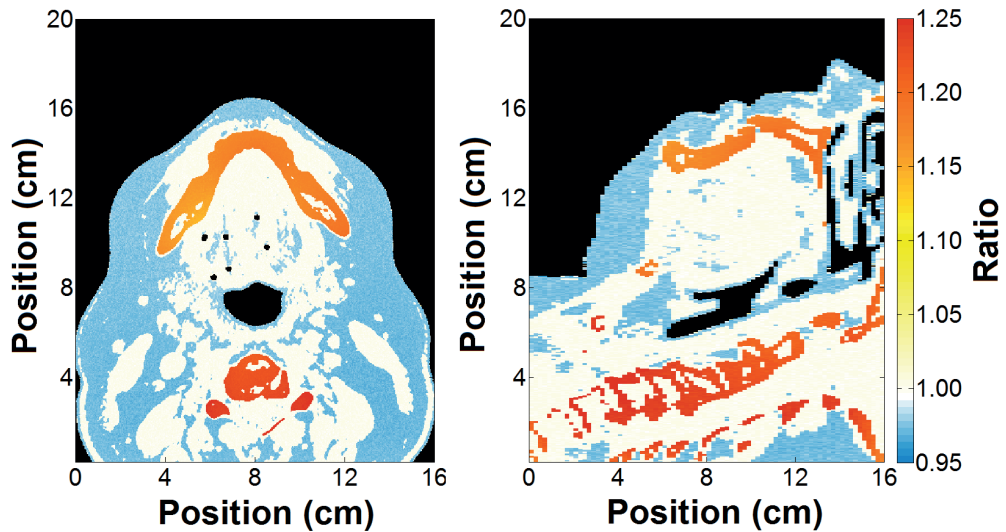


Figure 34. Ratio between conversion coefficients ($D_{w,m}(\text{LCT}) / D_{w,m}(\text{SCT})$). Uncertainty $<1\%$ for all points inside of the CT volume (Type A $\pm 1\sigma$).

5.4 Transit dose

5.4.1 Methodology validation

The discrete approximation for the source position while travelling was compared against a uniform distribution using a point source resulting in a maximum difference of 0.6% and 0.06% when using a resolution of 100 μm and 10 μm , respectively. The higher step resolution has been adopted to ensure that the methodology would not interfere with the final result. Once the spatial resolution was defined the transit dose component was calculated with the analytical method (Eq. 1) and simulated with MC techniques for a 10 cm long linear catheter considering a source air-kerma strength of 40700 U, as shown in Table 5.

The simulation results were validated by the analytical method showing small differences due to rounded numbers when processing the TPS data, due to the simulation uncertainty component Type A ($k=1$) of approximately 1% and due to the simplified approach which considers only the inverse square distance law. The transit dose component is proportional to the square root of the acceleration, i.e. the square root of the acceleration ratio of the microSelectron source (113 cm/s^2 – Ref. 46) and the Varian GammaMed Plus HDR source (55 cm/s^2 – Ref. 43) is 1.43, which is the same as the ratio between the respective transit doses obtained independently employing both accelerations. Moreover, an approximation of the transit dose component can be obtained by comparing the time the source spends traveling inside of the applicator and the total dwell time. For instance, for this applicator with 41 dwell positions, inter-dwell distance of 0.25 cm and a total dwell time of 76.0 s the dwell dose at the reference point is 510 cGy, while the transit time ($|a| = 113 \text{ cm/s}^2$) is 4.25 s and the transit dose is 28.5 cGy, which is approximately 6% of the total dwell time and 6% of the dwell dose. Adding one more parallel catheter with the same number of dwell position at the opposite side equidistantly of the reference point, for the same prescription dose the total dwell time would remain the same, but the transit time would double (it is independent of total dose).

Figure 35 shows the last two steps of the validation process: a) the MC probability ($P(x)$) is proportion to the time at each position and its inverse ($1/P(x)$) equal to the source instantaneous speed of each discrete source position. Values were compared against the analytical speed calculation (Figure 35.a and Figure 35.b) to validate the source speed profile calculate by the MATLAB algorithm; b) the dose distribution considering only the transit component was exported as DICOM images to BrachyVisionTM allowing a visualization of the applicator and its dwell positions over the transit dose distribution (Figure 35.c). This

figure shows that the transit dose distribution for a uniform accelerated movement follows the applicator geometry and has a higher dose deposition near the dwell positions, due to the source slowing down.

Table 5. Transit dose for a reference point orthogonal to the catheter’s longitudinal axis and positioned at 0.5 cm from its center (Figure 15.a). The values were calculated analytically (An) and simulated (MC) extracting the information from a treatment plan created with BrachyVision™. The underlined speeds were obtained considering a uniform accelerated movement for an acceleration of 113 cm/s² (Nucletron⁴⁶) and 55 cm/s² (Varian⁴³).

Inter-dwell distance (cm)											
0.25			0.5			1			2		
<i>v</i>	Dose (cGy)		<i>v</i>	Dose (cGy)		<i>v</i>	Dose (cGy)		<i>v</i>	Dose (cGy)	
(cm/s)	An.	MC	(cm/s)	An.	MC	(cm/s)	An.	MC	(cm/s)	An.	MC
60.0	2.5	2.5	60.0	2.5	2.5	60.0	2.5	2.5	60.0	2.5	2.5
30.0	5.0	5.0	30.0	5.0	5.0	30.0	5.0	5.0	30.0	5.0	5.0
* 2.7	30.5	30.5	3.8	22.5	22.5	5.3	17.0	17.0	7.5	12.9	12.9
<u>2.7</u>	30.1	30.0	<u>3.8</u>	22.0	22.1	<u>5.3</u>	16.7	16.6	<u>7.5</u>	10.7	10.6
** 2.2	38.0	38.5	3.1	28.3	28.3	4.4	21.2	21.2	6.2	16.4	16.4
<u>2.2</u>	43.1	43.0	<u>3.1</u>	31.5	31.6	<u>4.4</u>	23.9	23.9	<u>6.2</u>	15.3	15.2

*values obtained with an average return speed of 23.8 cm/s.

**values obtained with an average return speed of 16.6 cm/s.

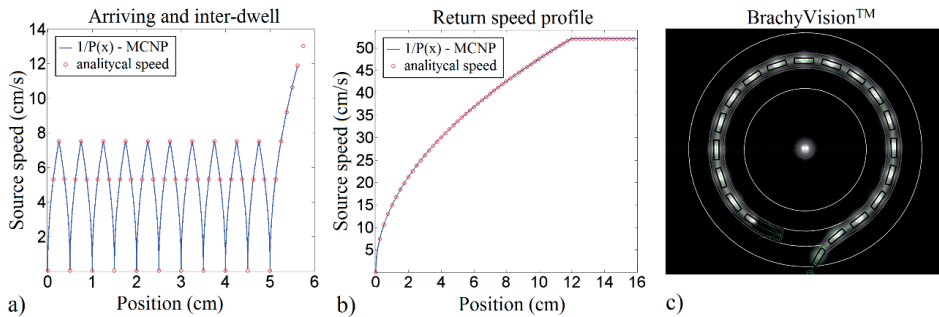


Figure 35. a) Source instantaneous speed, derived from the source trajectory and dwell positions, for each discrete source position compared against analytical calculation for the source approaching the first dwell position at 5 cm and moving between the dwell positions (right to left) up to the last dwell position that was defined as the origin; b) instantaneous speed validation for the source coming back to the safe; c) BrachyVision™ ring applicator showing the dwell positions (black boxes) superimposed over a transit dose distribution without the dwell dose component.

5.4.2 Studied cases

The studied cases simulated using a uniform acceleration of 113 cm/s^2 (ref. 46) are presented below and possible differences due to the speed profiles are discussed in section 3.3.

5.4.2.1 Gynecological cases

Case a with one central catheter has an average transit dose of 3.7 cGy or approximately $(0.5 \pm 0.1)\%$ of the dwell dose at the dose prescription points showing a more homogenous dose ratio due to the symmetry of the case. The time correction was applied with an average dwell time reduction of 0.16 s per dwell position reducing the transit dose component to approximately $(-0.1 \pm 0.1)\%$ of the dose at the prescription points.

The transit dose component for case b with 4 catheters varies according to the body regions and can be seen in Figure 36 where the transit dose considering the instantaneous speed shows a symmetrical behavior due to the uniformly distributed dwell positions while the dwell dose is higher on the right hand side of the applicator as can be seen by the isodoses in the Figure 36.a, which are a bit shifted to the right side.

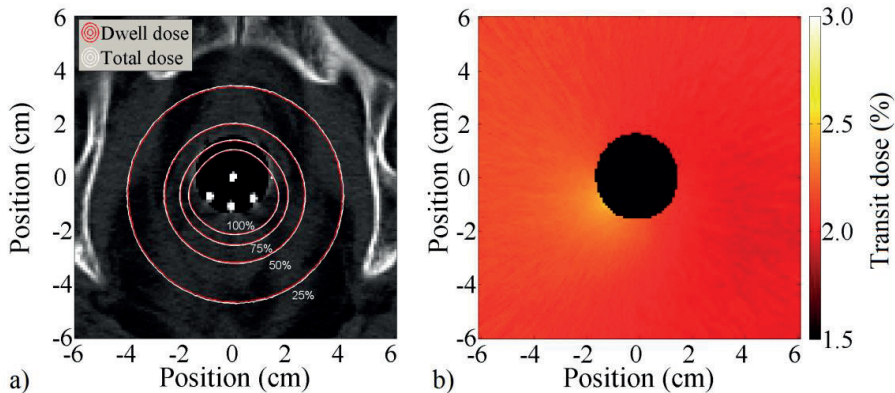


Figure 36. Gynecological case b (transverse plane): a) isodoses obtained considering the dwell dose and the total dose, which corresponds to the transit dose added to the dwell dose distribution; b) transit dose component as a percentage of the dwell dose without dwell time corrections. The dose inside of the applicator (black circle) was not scored.

The mean transit dose for case b is $(1.8 \pm 0.2)\%$ of the dose at the prescription points, reaching 28.4 cGy using the instantaneous speed approach ($|a| = 113 \text{ cm/s}^2$). A dwell time

correction calculated using equation 5 resulted in an average dwell time reduction of 0.13 s per dwell position reducing the mean transit dose component effect to less than 0.1% of the dwell dose at the dose prescription points. The proposed time correction is the same for both gynecological cases since they employ the same inter-dwell distance and this reduces the transit dose component by approximately a factor of 4 for these cases. The dwell and transit dose are around 5% higher when assigning proper material compositions compared to using an infinite water medium (TG43-U1 formalism),^{1, 2} but it does not affect the dose ratio. However, the dose difference is up to 7% at the prescriptions points when the TG43-U1 formalism is compared to the results obtained with proper material compositions and taking the transit dose into account together; this is mainly due to the air gap inside of the applicator.

5.4.2.2 Prostate case

The transit dose component for prostate case c reaches up to 20% or 1.8 Gy at some regions that present several catheters closer to each other (Figure 37) with an average transit dose component (Figure 37.b) of 1.1 Gy or (11.1±0.5)% of the dwell dose inside of the prostate including the dose to the urethra. The regions outside the prostate are mainly composed of soft tissues and show differences within 1% when proper tissue densities and composition are employed, which does not have a significant impact on the dose distribution when compared against a uniform water medium and makes no difference in the transit dose ratio. Figure 37.c shows the dose ratio with the dwell time correction, with an average difference 3.3 times lower than without correction, although the correction applied creates regions with dose differences between -5% and 6% at specific regions.

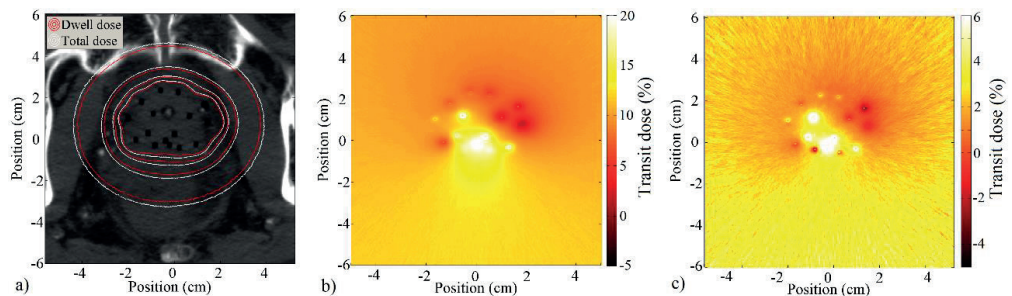


Figure 37. Prostate case c (transverse plane): **a**) isodoses in a CT slice with source catheters indicated as black holes and with the prostate contour approximately equal to the innermost isodose contour; **b**) the ratio in percentage between the transit dose and the dwell dose; **c**) the

ratio in percentage between the corrected transit dose and the dwell dose. Figures b and c are shown using different scales.

Prostate case d (Figure 38.a) has an average transit dose component (Figure 38.b) of $(3.8 \pm 0.2)\%$ inside prostate. Applying the dwell time correction reduced more than 2.9 times the transit dose effect inside of the prostate (Figure 38.c), but with some regions inside the prostate showing differences up to 2.7% at specific points.

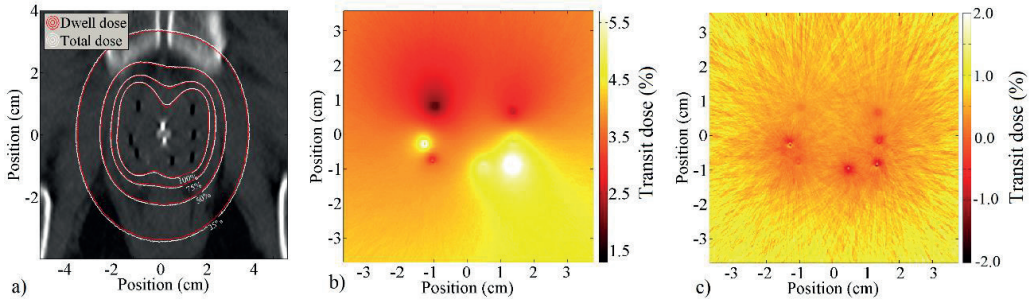


Figure 38. Prostate case d (transverse plane): a) Isodoses over a CT slice with the catheters corresponding to the boundaries of the prostate contour; b) transit dose percentage compared against the dwell dose. c) corrected transit dose percentage compared against the dwell dose. Figures b and c are shown using different scales.

5.4.3 Speed profile effects

The transit dose evaluated using some speed profiles based on literature data is presented in Table 6 for gynecological and prostate cases. The gynecological cases were evaluated considering the prescription points since the target contour was not available whilst the prostate cases were evaluated using the prostate contour to obtain the average dose inside of the volume.

5.4.4 Dwell time correction

The mean transit dose percentage over the volume can be estimated by calculating the total transit time of the source inside of the catheter and the total dwell time, as presented in Table 7. This is equivalent to the transit dose percentage averaged within the whole volume. The transit time was calculated considering an acceleration of $|a| = 77 \text{ cm/s}^2$ to compare the time correction adopted in this study with those obtained using equation 4 (Ref. 42).

Table 6. Transit dose component for the studied cases considering speed profiles based on literature data in absolute dose and in percentage of the dwell dose. The average speed of 2.7 cm/s (gynecological cases) and 3.8 cm/s (prostate cases) were obtained with an acceleration of 113 cm/s² for an inter-dwell distance of 2.5 mm (gynecological cases) and 5 mm (prostate cases).

Studied Cases				
	Average transit dose at the prescription points (cGy) / (%)		Average transit dose within the prostate volume (cGy) / (%)	
	Gynecological		Prostate	
	case a	case b	case c	case d
v = 50 cm/s	0.4 / <0.1	3.0 / 0.2	13.7 / 1.4	10.2 / 0.6
v = 30 cm/s	0.7 / 0.1	5.0 / 0.3	22.8 / 2.3	17.0 / 1.0
v = 2.7/3.8 cm/s	4.1 / 0.6	31.0 / 2.0	115.0 / 11.7	64.8 / 4.1
a=113 cm/s²	3.7 / 0.5	28.4 / 1.8	108.8 / 11.1	60.3 / 3.8
a=77 cm/s²	4.5 / 0.6	34.4 / 2.2	131.8 / 13.4	73.1 / 4.6
a=55 cm/s²	5.3 / 0.7	40.7 / 2.6	155.9 / 15.9	86.4 / 5.4

Table 7. Transit time for the studied cases considering a uniform acceleration of $|a| = 77$ cm/s² including the time correction applied. The mean transit dose was obtained considering the whole CT volume.

	Total dwell time (s)	Total transit time (s)	Time correction (s)		Transit time (%)	*Mean transit dose (%)	**Mean transit dose (%)
			This study	Palmer ⁴²			
case a	414.4	2.2	2.7	3.3	0.5	0.5	-0.1
case b	555.8	12.5	12.8	19.7	2.3	2.3	<0.1
case c	200.9	27.8	19.4	20.1	13.8	13.8	4.1
case d	232.2	12.4	8.7	9.0	5.3	5.6	1.9

*without time correction.

**with time correction.

5.4.5 Discussion

The transit dose component is case specific ranging from negligible ($\leq 0.5\%$) for a gynecological case with one catheter up to 13.8% for the average transit dose within the whole CT volume for a prostate case considering a uniform acceleration $|a| = 77$ cm/s². These observed differences were also dependent on the evaluated region since the dwell dose is higher near the target volume and negligible far away from it. The transit dose component may represent the majority of the delivered dose in some regions far away from the target.

The gynecological case with one catheter employed prescription points at 0.5 cm from the surface of the applicator which is 2.25 cm away from the dwell positions resulting in long dwell times which leads to a negligible transit dose component relative to the dwell dose. However, the transit component may not be negligible for other similar cases. For instance, the transit component for the gynecological case with four catheters is approximately 4 times higher than the first case due to the number of catheters. Even larger differences were observed between the intracavitary and the interstitial prostate cases since the latter modality has much lower dwell times than the gynecological cases due to the proximity of the treated region. Moreover, the evaluated prostate cases use several catheters (up to 16) which, in general, results in longer travel times leading to a more significant transit dose component.

Significant dose differences were also observed between the interstitial cases. The prostate case d was performed using a more uniform catheter and dwell position distribution inside the prostate and with less than half the number of catheters and dwell positions than in case c. Due to these differences the transit dose component inside the prostate volume in case d is approximately 3 times lower than in case c. Differences between the cases can be easily visualized by comparing the source travel time and the total dwell time presented in Table 7, which also provides an estimative of the average transit dose.

Although an estimative of the average transit dose can be obtained using the relationship between travel and dwell times, a uniform acceleration results in transit dose hot spots near the dwell positions and lower transit doses in between them leading to a complex transit dose distribution. This complexity level depends on the speed profile, number of catheters, dwell positions and their spatial distribution. These factors associated with a limited number of dwell positions do not allow a full transit dose compensation just by reducing the dwell time. This approach may lead to cold and hot spots since the time correction necessary to reduce the transit dose near the dwell positions may result in an underdose in other regions. Nevertheless, the applied dwell time corrections reduced considerably the transit dose component for our cases and produced more homogeneous distributions when using an accurate speed profile (Figure 37).

Tenfold differences can be observed between the speed scenario for the microSelectron (an average speed of 50 cm/s) and the worst scenario (uniform acceleration of $|a| = 55 \text{ cm/s}^2$) for all cases. The average transit dose inside the prostate volume obtained using an average or instantaneous variable speed with the same acceleration value were equivalent. However, these approaches lead to different transit dose distributions since the

transit dose near the dwell positions is much higher using the latter approach due to the source slowing down near the dwell positions.

The source travel time between the dwell positions is the main component of the transit dose within the target volume, which was the main interest in this study. However, when the acceleration is assumed uniform for the transit dose calculation a maximum source speed should be defined, otherwise the source could attain unrealistic speeds when exiting from the safe or returning to it. This study used 52 cm/s as the maximum source speed; different speed values showed no significant difference for the transit dose component for the studied cases due to the assumed trajectory length. These trajectories imported from the treatment plan have limited lengths since they cover mainly the region with dwell positions due to its clinical relevance. The source, in general, does not reach its maximum speed close to the target; this happens only over a few centimeters far away from the target volume.

5.5 Speed measurements

Figure 39.a shows the average speed ($\bar{v}_{0.2}$) for the average of 6 measurements, consisting of 3 arrival profiles and 3 return profiles. Video 1 shows an example of the measurements with one dwell position at the end of the trajectory. There is no continuous slowing down since the motor stops instantaneously at the dwell position causing source oscillations around it. No differences were seen for the arrival and return source speed profile due to the source stopping when arriving at a dwell position and accelerating from rest when returning to the safe. This is because the source acceleration is high and average speeds were obtained over 0.2 cm reducing the differences in the speed profile near the dwell position. The only exception was noted for one point at 0.5 cm from the dwell position for which the arrival and return speed values were added in Figure 39.a.

Video 2 shows the source movement described in Figure 39.b with $\bar{v}_{0.2}$ values obtained for six dwell positions equally spaced between 0 and 5 cm. The source speed appears to exhibit a periodicity. The labelled points in Figure 39.b refer to the following phases: (1) source accelerating after leaving the dwell position; (2) source reaches maximum speed; (3) source decelerates reaching the lowest speed around 0.5 cm from the dwell position; (4) source accelerating again; (5) Source reaches a high speed just before dwelling.

The source stops at non-programmed positions for less than (0.005 ± 0.001) s, which can be seen in video 2. However, Figure 39.b does not show zero source speed at non-programmed dwell positions since only averaged $\bar{v}_{0.2}$ values are shown. The speed variation appears to reduce

with larger distances as can be observed in video 3 that shows the source movement between two consecutive dwell positions, at 0 and 5 cm, also depicted in Figure 39.c.

According to the manufacturer, to compensate for the transit time the afterloader reduces the dwell time at each dwell position with the time spent in travelling to it, to a maximum of 0.1 s. The measured mean value of this correction is (0.06 ± 0.03) s, which is in good agreement with Wong et al.⁴⁴, (0.07 ± 0.01) s. The time correction was measured for 43 dwell positions going from (0.030 ± 0.007) s up to (0.096 ± 0.037) s for inter-dwell distance of 0.25 and 2.5 cm, respectively. In addition, we verified that the source spends up to (0.026 ± 0.005) s oscillating around the dwell positions after the motor stops (video 4). The amplitude of the oscillation depends on the inter-dwell distance which is 0.08 cm for the source arriving at the first dwell-position, 0.15 cm for 0.25 cm inter-dwell distance (video 4), 0.05 cm for 0.5 and 1 cm inter dwell distances and 0.08 cm for 2.5 and 5 cm inter dwell distances.

The source step size of the afterloader is either 0.25, 0.50 or 1.00 cm. This did not cause measurable differences for inter-dwell source speed profiles for 0.25, 0.50, 1.00, 2.50 and 5.00 cm inter-dwell distances. On the other hand, the speed profiles depend on the inter-dwell distance following non-uniform movements. Table 8 shows the average speed obtained in this work compared against literature data.

Table 8. Average source speed over the inter-dwell length for inter-dwell distances of 0.25, 0.50, 1.00, 2.50 and 5.00 cm. Uncertainty values were not available for all the references. All the values were obtained for a Nucletron afterloader (Elekta Brachytherapy, Veenendaal, the Netherlands), however, the model may change.

Inter-dwell distance (cm)	This work (cm/s)	Wong⁴⁴ (cm/s)	Sahoo*⁴⁵ (cm/s)	Bastin⁴⁷	Houdek¹⁴⁵
0.25	32.8 ± 2.7	5.4 ± 2.3	-	23.0	22.7
0.50	45.8 ± 2.6	7.2 ± 1.6	33.3	25.5	27.1
1.00	34.9 ± 0.9	23.3 ± 7.3	50.0	-	30.3
2.50	32.3 ± 0.3	-	-	-	-
5.00	32.0 ± 0.2	-	43.5	-	33.1

*Transit time measurement uncertainty is up to 100% for inter-dwell distances less than 1.00 cm and between 9% and 26% for larger distances.⁴⁵

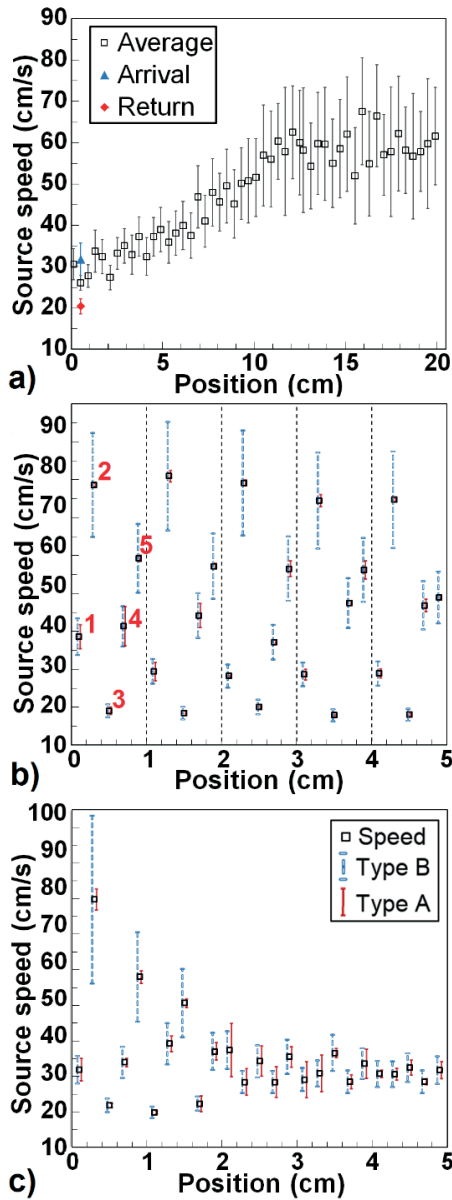


Figure 39. **a)** Source speed profile for the source arriving at the first dwell position (0 cm) and returning to the safe. Uncertainties Type A and Type B are almost equivalent so only Type B component is shown. **b)** $\bar{v}_{0.2}$ values were obtained for six dwell positions equally spaced between 0 and 5 cm (vertical dotted lines). **c)** $\bar{v}_{0.2}$ values were obtained for the source movement between two dwell positions, at 0 cm and 5 cm. Figures **b)** and **c)** use the same notation with Type A and Type B uncertainty components indicated. The source speeds at the dwell positions were not considered, therefore figures do not show speed values equal to zero.

5.5.1 Transit dose

The differences between the absolute dose values obtained using OncentraTM and MCNP6 were less than 1% for the points evaluated, which is about of the same magnitude as the simulation uncertainty (<0.5%). However, the speed profile presents uncertainties up to 21% that can lead to transit dose uncertainties of the same order in some regions.

The transit dose due to the source arriving, moving between the dwell positions, returning to the safe, and the total transit dose can be seen in Figure 40.a1 and Figure 40.b1. These represent the cases described in Figure 39.b and Figure 39.c, respectively. The maximum transit dose is 43 mGy for both cases, however, the component due to the inter-dwell movement is smaller for the case with 6 dwell positions Figure 40.a.1. The dose reduction applied (dwell time correction) to compensate the transit dose and the corrected dose are shown for both cases in Figure 40 (**bottom**).

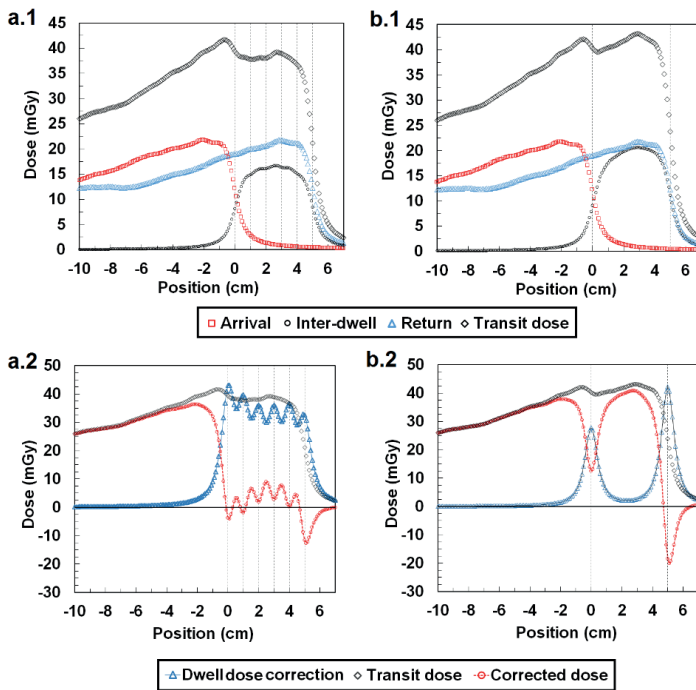


Figure 40. Transit dose components (**top**) for a case with six dwell positions equally spaced between 0 and 5 cm (**a**) and for a case with two dwell positions (**b**), at 0 cm and 5 cm. The dose reduction (dwell dose correction) applied to compensate the transit dose and the corrected dose are shown for both cases (**bottom**). Dwell positions are indicated with vertical dotted lines.

The dose reduction due to the dwell time correction applied by the manufacturer was obtained with a 0.073 s dwell time for the first position (0 cm) and dwell times between 0.047 and 0.052 s for the other dwell positions (Figure 40.a2 / video 2). The case with 2 dwell positions (Figure 40.b2 / video 3) was simulated with 0.056 s dwell time for the first position and 0.085 s for the last position. The correction applied by the manufacturer compensates for the transit dose between the dwell positions for 1 cm inter-dwell distance leading to a smaller transit dose and even to underdoses near the last dwell position (Figure 1.b1). The corrected dose obtained with a 5 cm inter-dwell distance shows that the dwell time reduction compensates the transit dose only near the dwell positions and also leads to underdose near the end of the trajectory. The maximum overdose after the dwell time correction was 41 mGy, which is within 1.4% for commonly prescribed doses (3-10 Gy/fraction)¹⁴⁶.

5.5.2 Discussion

The periodic speed variations seem to be independent of the inter-dwell distance. For example, the speed profile for 1 cm inter-dwell distance (Figure 39.b) is similar to the speed profile of the first centimeter obtained with 5 cm inter-dwell distance (Figure 39.c). Moreover, the speed profile obtained with 5 cm inter-dwell distance was used to obtain average speeds for the first 0.25, 0.50, 1.00 and 2.50 cm of the source trajectory. All values obtained are equivalent to the average speed profiles obtained for equivalent inter-dwell distances (Table 8) within uncertainties. The highest average speed for the 0.5 cm inter-dwell distance occurs due to the absence of non-programmed dwell positions for this inter-dwell distance. In addition, the source reaches the maximum speed (Figure 39.b and 2.c) within 0.5 cm inter-dwell distance and does not reach it for a 0.25 cm inter-dwell distance, which also explains a higher average speed for the 0.5 cm than for 0.25 cm inter-dwell distance.

The complex behavior of the source movement, including very short stops at non-programmed positions, was also observed for another afterloader by Wojcicka et al.⁴³ One possible explanation for the observed variations could be attributed to a motor warm-up since the amplitude of speed oscillations reduces with distance (Figure 39.c). It can also be due to wire spring or another mechanical property of the equipment, which was not evaluated in this study.

The periodic speed variations may explain differences obtained in the literature as source speed varies significantly with source position. Studies performed with a video camera with a lower frame rate or detectors at fixed positions would not have the required

spatial/temporal resolution to observe these effects. This explanation does not apply for integration methods, which may indicate that differences can be due to high uncertainties and/or different behaviors between each piece of equipment or their models. This highlighted the importance of including transit dose component measurements in quality assurance (QA) tests since low speed sources can lead to high transit doses.^{50, 146} Williamson et al. also described a simple methodology to measure source speed using an ionization chamber and how to estimate the transit dose that can be employed for QA tests.¹⁴⁶

The transit dose does not seem to be significant for the obtained speed profiles. A previous study showed that the transit dose with average speed of 30 cm/s (close to values measured in this study) would result in transit doses up to 0.3% and 2.3% of the prescribed dose for a gynecological and a prostate case.⁵⁰ These values were obtained without any dwell time correction so the real impact of the transit dose would be even smaller.⁵⁰ On the other hand, our results show that the transit dose is not uniformly distributed and that the transit dose for dwell positions far apart (Figure 40.b2) were not fully corrected showing over and underdoses. The dwell time correction applied by the manufacturer is more efficient for smaller inter-dwell distances (Figure 40.b1). Additional dwell positions do not increase the transit dose due to the instantaneous source stop and fast acceleration leading to high average speed even for small inter-dwell distances.

Our findings do not apply for sources with lower acceleration or following uniform accelerated movements^{42, 43, 46} for which additional dwell positions would increase the transit time due to the source slowing down and accelerating from rest near the dwell positions.⁵⁰ The impact of the number of the dwell positions may be relevant if the average speed depends on the inter-dwell distance, which should be evaluated for each source since the transit effect may be more relevant for slower sources.

Transit dose could also be taken into account at the treatment planning stage, instead of attempting to correct for it during radiation delivery.

CONCLUSIONS

Chapter 6

6 CONCLUSIONS

Obtained results are relevant for HDR brachytherapy treatment planning. Although not clinically available, most subjects described in this thesis can be assessed using AMIGOB rady that offers a user-friendly interface providing resources to perform dose calculations based on MC simulation. It takes into account the body geometry, tissue composition and applicator attenuation as recommended by TG-186. The studied cases show good agreement with ACUROS™ with some under and overdosing compared to TG-43U1 based dose with differences around 5% within the target volume and up to 25% within the evaluated regions. AMIGOB rady can improve the accuracy of the dose distribution through a more accurate applicator representation and/or a more accurate dose calculation algorithm that can handle tissue composition. Currently, low energy EBS for which tissue composition is highly significant can also be simulated using the developed interface. Moreover, AMIGOB rady can import applicators in the CAD format and includes metal needles that are not present in the ACUROS™ applicator database.

CAD mesh features are applicable to Geant4 and MCNP6 MC codes, which allow the modelling of complex brachytherapy applicator geometries in MC simulations, as an alternative to CSG representations. Results were validated using simple cases allowing CSG representation. For complex applicators, which do not allow straightforward CSG modelling such as the shielded Fletcher Williamson applicator, we validated the MG method using a modified model. For the realistic APBI balloon applicator, which has an irregular geometry that precludes easy modelling with CSG, we have observed good agreement between MCNP6 and Geant4. The use of MG generally entails a computation efficiency penalty compared to simulation times for CSG with the same code, for the cases evaluated in this work. However, simulation times depend on the Monte Carlo code and on the simulation setup with MG being faster than CSG for some cases in the literature.¹⁴⁷ Strategies such as scoring a phase space at the surface of applicators could be employed to minimize the impact of this penalty. The methods presented here can be used in the validation process of treatment planning systems or to evaluate modifications to applicator design. The MG method should also be equally useful in modelling other complex radiotherapy devices in external beam radiotherapy with photons, electrons or light ions.

The AMIGOB rady/MCNP6 capability to score $D_{m,m}$ and $D_{w,m}$, mean-energy and source spectrum is an important feature. For HDR brachytherapy with the ^{192}Ir isotope the photon spectrum changes considerably inside the patient as function of distance to implant and depending on the patient/phantom material composition. The low energy photon

contribution to the total dose is higher in regions away from the implant. The results obtained show that differences between $D_{m,m}$ and $D_{w,m}$ (SCT or LCT) can be negligible (<1%) for some tissues as muscle and significant for other tissues with differences up to 14% for bone in the evaluated head and neck case. The dose conversion approach (SCT or LCT) leads to significant differences since materials with $(\mu_{en}/\rho)_w^m$ greater than 1 may have $(S/\rho)_w^m$ less than 1 or vice versa (Figure 1). Therefore differences between conversion factors (LCT and SCT) are up to 28% for bone and 36% for teeth. It is essential that brachytherapy studies explicitly mention which dose reporting quantity has been used ($D_{m,m}$, $D_{w,m}$ (LCT), or $D_{w,m}$ (SCT)). Of extra importance is to be aware that in some materials and locations, the difference between $D_{w,m}$ (LCT), $D_{w,m}$ (SCT) and $D_{m,m}$ are substantial.

Finally, transit dose component due to the source movement can be assessed once the speed profiles are well know. The transit dose for ^{192}Ir HDR brachytherapy treatments can be significant reaching more than 1.8 Gy (worst case scenario without include dwell time corrections) and representing up to 20% of the dwell dose for the a specific region of the prostate case analyzed in this study. The transit dose was found to be more significant for the interstitial cases analyzed since they have lower dwell times due to de proximity between the dwell positions and the tissue. The simple approach adopted here to reduce the transit dose component is approximately equivalent to the one adopted by Palmer et al.¹⁰ reducing significantly the transit dose component. Although the literature data shows a wide spread in reported values for the source speed profile, the source speed seems to be low enough to produce significant effects in the dose distribution, which should be taken into account.^{8,9,10,13} A high speed camera allowed a detailed determination of the source movement for a Nucletron source, which can be clearly visualized with the videos available online. The dwell time correction applied by the manufacturer (Figure 40) may lead to doses, averaged over the volume, equivalent to the planned doses since the transit time between the dwell positions may be fully compensated reducing the dwell times. This depends on the distances between dwell positions, though. However, the transit dose distribution is not uniform and, ideally, should be considered during treatment planning to optimize the dose distribution. The transit dose correction may be greater than the transit dose leading to underdose at some regions (Figure 40). This issue increases in importance for slower moving brachytherapy sources.

The main subjects evaluated in this study are relevant for brachytherapy treatment planning and have the potential to improve treatment accuracy. Although not clinically available, many of the issues described in here can be assessed with AMIGOBrachy, coupled with a MC code.

FUTURE PERSPECTIVES

Chapter 7

7 FUTURE PERSPECTIVES

Relevant advances have been made in several issues to improve brachytherapy, which show the effort of different research groups to publish around 1000 papers per year (PubMed^{††} - 21 January 2015), with the term ‘brachytherapy’, between 2012 and 2014. Moreover, efforts are also related with image segmentation, imaging techniques, artifacts corrections and other issues that may not appear in the search since brachytherapy may not be mentioned due to the general application of these topics. However, much still need be done to make recent advances clinically available and to move further with unexplored issues.

Some relevant issues that need further investigations were pointed out along this thesis and summarized below.

- Although MBDCAs algorithms are available, dwell times are calculated using TG-43U1 since ACUROSTM, ACE and MC codes are not fast enough to perform dose optimizations. Therefore, MBDCAs are used clinically only for dose recalculations. Technical efforts are necessary to improve both computational power and software efficiency.
- Dosimetry for brachytherapy is a complex issue due to the sharp dose gradient being disregarded for several clinical centers due to the large uncertainties. Measurements, including in-vivo dosimetry, are highly important to detect source misplacements or dose miscalculation. To reduce experimental uncertainty some issues should be considered: dosimeters energy dependence must be carefully evaluated for low energies; real time positioning system should be employed.
- Source speed profiles should be characterized for several afterloads since differences in the literature are significant and can lead to negligible or highly significant transit doses. Currently, it is unclear the reason between such large differences in the speed profile, however, this thesis demonstrates that it can lead to non-uniform dose distribution and that more accurate corrections are necessary.
- Dose report quantities ($D_{w,m}$ and $D_{m,m}$) obtained using SCT or LCT differs significantly and are patient specific due to the energy dependence of results obtained using LCT. More studies are necessary to define standards allowing comparison between results obtained in different centers.

^{††} <http://www.ncbi.nlm.nih.gov/pubmed/>

Significant advances are expected within the next few years that will lead to much more accurate treatment planning system capable of handle tissue composition, transit dose component and applicators during optimization. Dosimetry improvements and real time measurements will follow these advances since accurate experimental validation of such accurate treatments plans seems to be a logical next step.

LIST OF PUBLICATIONS

8 LIST OF PUBLICATIONS

8.1 Published articles

F. Ballester, J. Vijande, A.C. Tedgren, D. Granero, A. Haworth, R. Smith, F. Mourtada, **G.P. Fonseca**, K. Zourari, P. Papagiannis, F.A Siebert, M.J. Rivard, R. S. Sloboda, R.M. Thomson, F. Verhaegen, Y. Ma, L. Beaulieu, "A generic high-dose-rate Ir-192 brachytherapy source for evaluation of model-based dose calculations beyond the TG-43 formalism," *Med Phys* **42**(6), 3048 (2015)

G.P. Fonseca, A.C. Tedgren, B. Reniers, J. Nilsson, M. Person, H. Yoriyaz, F. Verhaegen, "Dose specification for ¹⁹²Ir high dose rate brachytherapy in terms of dose to water in medium and dose to medium in medium" *Phys Med Biol* **60**, 4565-4579 (2015)

G.P. Fonseca, R.S. Viana, M. Podesta, R.A. Rubo, C.P. de Sales, B. Reniers, H. Yoriyaz, F. Verhaegen, "HDR (¹⁹²)Ir source speed measurements using a high speed video camera," *Med Phys* **42**, 412 (2015)

G.P. Fonseca, G. Landry, S. White, M. D'Amours, H. Yoriyaz, L. Beaulieu, B. Reniers, F. Verhaegen, "The use of tetrahedral mesh geometries in Monte Carlo simulation of applicator based brachytherapy dose distributions," *Phys Med Biol* **59**, 5921-5935 (2014).

G.P. Fonseca, B. Reniers, G. Landry, S. White, M. Bellezzo, P.C.G. Antunes, C.P. de Sales, E. Weltman, H. Yoriyaz, F. Verhaegen, "A medical image-based graphical platform—Features, applications and relevance for brachytherapy," *Brachytherapy* **13**, 632-639 (2014)

S. White, G. Landry, **G. P. Fonseca**, R. W. Holt, T. W. Rusch, L. Beaulieu, F. Verhaegen, B. Reniers, "Comparison of TG-43 and TG-186 in breast irradiation using a low energy electronic brachytherapy source", *Med. Phys.* 41(6), pp. 061701 (2014)

G.P. Fonseca, G. Landry, B. Reniers, P. C. G Antunes, H. Yoriyaz, F. Verhaegen, "The contribution from transit dose for ¹⁹²Ir HDR brachytherapy treatments", *Phys. Med. Biol.* **59**, 1831-1844 (2014)

G. P. Fonseca, R. A. Rubo, R. A. Minamisawa, G. R. dos Santos, P. C. G. Antunes, H. Yoriyaz, "Determination of transit dose profile for a ¹⁹²Ir HDR source", *Med. Phys.* **40**(5), pp. 051717-1: 051717-8 (2013)

8.2 Conferences

G. P. Fonseca, J. Luvizotto, T. S. Coelho, P.C.G. Antunes, P. T. D. Siqueira, H. Yoriyaz. “Brachytherapy dose measurements in heterogeneous tissues” XIV International Symposium on Solid State Dosimetry, Cusco, Peru, 2014.

G. P. Fonseca, B. Reniers, J. Nilsson, M. Persson, A. C. Tedgren, H. Yoriyaz, F. Verhaegen, “Monte Carlo Simulation of HDR Ir-192 Brachytherapy Cancer Treatments”. ABS (American Brachytherapy Society) Annual Meeting. San Diego, USA, 2014.

G. P. Fonseca, J. Luvizotto, P. C. G. Antunes, H. Yoriyaz, “Dose Measurements for an Ir-192 Source Using Mosfets, Radiochromic Films, TLDs and Heterogeneous Tissues”. ABS (American Brachytherapy Society) Annual Meeting. San Diego, USA, 2014.

G.P. Fonseca, P.C.G. Antunes, B. Reniers, H. Yoriyaz, F. Verhaegen. “A brachytherapy model-based dose calculation algorithm – AMIGOBrachy”. International Nuclear Atlantic Conference, Recife, Brazil, 2013.

G. Landry, **G.P. Fonseca**, S. Enger, M. d’Amours, S. White, B. Reniers, L. Beaulieu, F. Verhaegen, The use of tetrahedral meshes and layered mass geometry in Geant4 brachytherapy applications, Bordeaux, France, 2013.

G.P. Fonseca, B. Reniers, F. Verhaegen, H. Yoriyaz. “Impact of heterogeneities in a gynecological cancer treatment using a HDR Ir-192 source”. 2ND ESTRO forum, GENEVA, Switzerland, 2013.

G. P. Fonseca, H. Yoriyaz, P. C. G. Antunes, P. T. D. Siqueira, R. Rubo, R. A. Minamisawa, L. A. Ferreira, “Characterization of HDR Ir-192 source for 3D planning system” International Nuclear Atlantic Conference – INAC, Belo Horizonte, Brazil, 2011.

**CURRICULUM
VITAE**

9 CURRICULUM VITAE

Born in Itapeva, Brazil, Gabriel Paiva Fonseca obtained a degree in physics from University of São Paulo (USP) in 2007. He developed interest for Monte Carlo methods in medical physics performing several experiments with linear accelerators and brachytherapy sources using several dosimeters to benchmark calculated results. A master degree in medical physics was obtained in 2010 developing scattering plates to increase the treatment field of a linear accelerator to perform total skin irradiations. In 2011 he started a Ph.D in Brazil under supervision Prof. Dr Hélio Yoriyaz joining Maastricht (Maastricht University (MU) – the Netherlands) research team in 2012 under supervision of Prof. Dr. Frank Verhaegen. He concluded his double Ph.D, USP and MU, in 2015 performing research activities in both countries Brazil and the Netherlands.

Main research subjects:

- Monte Carlo methods;
- Medical images (CT and MRI);
- Brachytherapy treatment planning systems;
- Experimental dosimetry using TLDs, MOSFETs and films;
- Patient specific dose calculations.

REFERENCES

10 REFERENCES

- ¹ R. Nath, L.L. Anderson, G. Luxton, K.A. Weaver, J.F. Williamson, A.S. Meigooni, "Dosimetry of interstitial brachytherapy sources: recommendations of the AAPM Radiation Therapy Committee Task Group No. 43. American Association of Physicists in Medicine," *Med Phys* **22**, 209-234 (1995).
- ² M.J. Rivard, B.M. Coursey, L.A. DeWerd, W.F. Hanson, M.S. Huq, G.S. Ibbott, M.G. Mitch, R. Nath, J.F. Williamson, "Update of AAPM Task Group No. 43 Report: A revised AAPM protocol for brachytherapy dose calculations," *Med Phys* **31**, 633-674 (2004).
- ³ G. Landry, B. Reniers, L. Murrer, L. Lutgens, E.B. Gulp, J.P. Pignol, B. Keller, L. Beaulieu, F. Verhaegen, "Sensitivity of low energy brachytherapy Monte Carlo dose calculations to uncertainties in human tissue composition," *Med Phys* **37**, 5188-5198 (2010).
- ⁴ S.M. Hsu, C.H. Wu, J.H. Lee, Y.J. Hsieh, C.Y. Yu, Y.J. Liao, L.C. Kuo, J.A. Liang, D.Y. Huang, "A study on the dose distributions in various materials from an Ir-192 HDR brachytherapy source," *PLoS One* **7**, e44528 (2012).
- ⁵ L. Beaulieu, A. Carlsson Tedgren, J.F. Carrier, S.D. Davis, F. Mourtada, M.J. Rivard, R.M. Thomson, F. Verhaegen, T.A. Wareing, J.F. Williamson, "Report of the Task Group 186 on model-based dose calculation methods in brachytherapy beyond the TG-43 formalism: current status and recommendations for clinical implementation," *Med Phys* **39**, 6208-6236 (2012).
- ⁶ G.P. Fonseca, B. Reniers, G. Landry, S. White, M. Bellezzo, P.C.G. Antunes, C.P. de Sales, E. Weltman, H. Yoriyaz, F. Verhaegen, "A medical image-based graphical platform—Features, applications and relevance for brachytherapy," *Brachytherapy* **13**, 632-639 (2014).
- ⁷ G. Landry, M.J. Rivard, J.F. Williamson, F. Verhaegen, "Monte Carlo Methods and Applications for Brachytherapy Dosimetry and Treatment Planning," in *Monte Carlo Techniques in Radiation Therapy*, edited by J. Seco, F. Verhaegen (2013), pp. 125-143.
- ⁸ S.A. White, G. Landry, G.P. Fonseca, R. Holt, T. Rusch, L. Beaulieu, F. Verhaegen, B. Reniers, "Comparison of TG-43 and TG-186 in breast irradiation using a low energy electronic brachytherapy source," *Med Phys* **41**, 061701 (2014).
- ⁹ K.A. Gifford, J.L. Horton, T.A. Wareing, G. Failla, F. Mourtada, "Comparison of a finite-element multigroup discrete-ordinates code with Monte Carlo for radiotherapy calculations," *Phys Med Biol* **51**, 2253-2265 (2006).
- ¹⁰ L. Petrokokinos, K. Zourari, E. Pantelis, A. Moutsatsos, P. Karaiskos, L. Sakelliou, I. Seimenis, E. Georgiou, P. Papagiannis, "Dosimetric accuracy of a deterministic radiation transport based ¹⁹²Ir brachytherapy treatment planning system. Part II: Monte Carlo and experimental verification of a multiple source dwell position plan employing a shielded applicator," *Med Phys* **38**, 1981-1992 (2011).
- ¹¹ S.A. Lloyd, W. Ansbacher, "Evaluation of an analytic linear Boltzmann transport equation solver for high-density inhomogeneities," *Med Phys* **40**, 011707 (2013).
- ¹² A. Carlsson Tedgren, A. Ahnesjo, "Optimization of the computational efficiency of a 3D, collapsed cone dose calculation algorithm for brachytherapy," *Med Phys* **35**, 1611-1618 (2008).
- ¹³ M.J. Rivard, J.L. Venselaar, L. Beaulieu, "The evolution of brachytherapy treatment planning," *Med Phys* **36**, 2136-2153 (2009).
- ¹⁴ A. Ahnesjo, "Collapsed cone convolution of radiant energy for photon dose calculation in heterogeneous media," *Med Phys* **16**, 577-592 (1989).

- 15 A. Carlsson Tedgren, A. Ahnesjo, "The collapsed cone superposition algorithm applied to scatter dose calculations in brachytherapy," *Med Phys* **27**, 2320-2332 (2000).
- 16 G.P. Fonseca, G. Landry, S. White, M. D'Amours, H. Yoriyaz, L. Beaulieu, B. Reniers, F. Verhaegen, "The use of tetrahedral mesh geometries in Monte Carlo simulation of applicator based brachytherapy dose distributions," *Phys Med Biol* **59**, 5921-5935 (2014).
- 17 G.P. Fonseca, G. Landry, B. Reniers, A. Hoffmann, R.A. Rubo, P.C. Antunes, H. Yoriyaz, F. Verhaegen, "The contribution from transit dose for (192)Ir HDR brachytherapy treatments," *Phys Med Biol* **59**, 1831-1844 (2014).
- 18 J.K. Mikell, A.H. Klopp, M. Price, F. Mourtada, "Commissioning of a grid-based Boltzmann solver for cervical cancer brachytherapy treatment planning with shielded colpostats," *Brachytherapy* **12**, 645-653 (2013).
- 19 A. Carlsson Tedgren, A. Ahnesjo, "Accounting for high Z shields in brachytherapy using collapsed cone superposition for scatter dose calculation," *Med Phys* **30**, 2206-2217 (2003).
- 20 H. Afsharpour, G. Landry, M. D'Amours, S. Enger, B. Reniers, E. Poon, J.-F. Carrier, F. Verhaegen, L. Beaulieu, "ALGEBRA: ALgorithm for the heterogeneous dosimetry based on GEANT4 for BRachytherapy," *Physics in Medicine and Biology* **57**, 3273 (2012).
- 21 E. Poon, Y. Le, J.F. Williamson, F. Verhaegen, "BrachyGUI: an adjunct to an accelerated Monte Carlo photon transport code for patient-specific brachytherapy dose calculations and analysis," *Journal of Physics: Conference Series* **102**, 012018 (2008).
- 22 M.J. T. Goorley, T. Booth, F. Brown, J. Bull, L. J. Cox, J. Durkee, J. Elson, M. Fensin, R. A. Forster, J. Hendricks, H. G. Hughes, R. Johns, B. Kiedrowski, R. Martz, S. Mashnik, G. McKinney, D. Pelowitz, R. Prael, J. Sweezy, L. Waters, T. Wilcox, T. Zukaitis, "Initial MCNP6 Release Overview," *Radiation Transport and Protection* **180**, 298-315 (2012).
- 23 K.A. Gifford, J.L. Horton, E.F. Jackson, T.R. Steger, M.P. Heard, F. Mourtada, A.A. Lawyer, G.S. Ibbott, "Comparison of Monte Carlo calculations around a Fletcher Suit Delclos ovoid with radiochromic film and normoxic polymer gel dosimetry," *Med Phys* **32**, 2288-2294 (2005).
- 24 J. Markman, J.F. Williamson, J.F. Dempsey, D.A. Low, "On the validity of the superposition principle in dose calculations for intracavitary implants with shielded vaginal colpostats," *Med Phys* **28**, 147-155 (2001).
- 25 K.J. Weeks, "Monte Carlo dose calculations for a new ovoid shield system for carcinoma of the uterine cervix," *Med Phys* **25**, 2288-2292 (1998).
- 26 M.J. Price, K.A. Gifford, J. Horton, A. Lawyer, P. Eifel, F. Mourtada, "Comparison of dose distributions around the pulsed-dose-rate Fletcher-Williamson and the low-dose-rate Fletcher-Suit-Delclos ovoids: a Monte Carlo study," *Physics in Medicine and Biology* **51**, 4083 (2006).
- 27 J.F. Williamson, "Dose calculations about shielded gynecological colpostats," *Int J Radiat Oncol Biol Phys* **19**, 167-178 (1990).
- 28 S. Agostinelli, J. Allison, K. Amako, J. Apostolakis, H. Araujo, P. Arce, M. Asai, D. Axen, S. Banerjee, G. Barrand, F. Behner, L. Bellagamba, J. Boudreau, L. Broglia, A. Brunengo, H. Burkhardt, S. Chauvie, J. Chuma, R. Chytrcek, G. Cooperman, G. Cosmo, P. Degtyarenko, A. Dell'Acqua, G. Depaola, D. Dietrich, R. Enami, A. Feliciello, C. Ferguson, H. Fesefeldt, G. Folger, F. Foppiano, A. Forti, S. Garelli, S. Giani, R. Giannitrapani, D. Gibin, J.J.G. Cadenas, I. Gonzalez, G.G. Abril, G. Greeniaus, W. Greiner, V. Grichine, A. Grossheim, S. Guatelli, P. Gumplinger, R.

- Hamatsu, K. Hashimoto, H. Hasui, A. Heikkinen, A. Howard, V. Ivanchenko, A. Johnson, F.W. Jones, J. Kallenbach, N. Kanaya, M. Kawabata, Y. Kawabata, M. Kawaguti, S. Kelner, P. Kent, A. Kimura, T. Kodama, R. Kokoulin, M. Kossov, H. Kurashige, E. Lamanna, T. Lampen, V. Lara, V. Lefebure, F. Lei, M. Liendl, W. Lockman, F. Longo, S. Magni, M. Maire, E. Medernach, K. Minamimoto, P.M. de Freitas, Y. Morita, K. Murakami, M. Nagamatu, R. Nartallo, P. Nieminen, T. Nishimura, K. Ohtsubo, M. Okamura, S. O'Neale, Y. Oohata, K. Paech, J. Perl, A. Pfeiffer, M.G. Pia, F. Ranjard, A. Rybin, S. Sadilov, E. Di Salvo, G. Santin, T. Sasaki, N. Savvas, Y. Sawada, S. Scherer, S. Seil, V. Sirotenko, D. Smith, N. Starkov, H. Stoecker, J. Sulkimo, M. Takahata, S. Tanaka, E. Tcherniaev, E.S. Tehrani, M. Tropeano, P. Truscott, H. Uno, L. Urban, P. Urban, M. Verderi, A. Walkden, W. Wander, H. Weber, J.P. Wellisch, T. Wenaus, D.C. Williams, D. Wright, T. Yamada, H. Yoshida, D. Zschesche, "Geant4-a Simulation Toolkit," *Nuclear Instruments & Methods in Physics Research Section a-Accelerators Spectrometers Detectors and Associated Equipment* **506**, 250-303 (2003).
- 29 T. Goorley, M. James, T. Booth, F. Brown, J. Bull, L.J. Cox, J. Durkee, J. Elson, M. Fensin, R.A. Forster, J. Hendricks, H.G. Hughes, R. Johns, B. Kiedrowski, R. Martz, S. Mashnik, G. McKinney, D. Pelowitz, R. Prael, J. Sweezy, L. Waters, T. Wilcox, T. Zukaitis, "Initial MCNP6 release overview," *Radiation Transport and Protection* **180**, 298-315 (2012).
- 30 C.M. Ma, J. Li, "Dose specification for radiation therapy: dose to water or dose to medium?," *Phys Med Biol* **56**, 3073-3089 (2011).
- 31 I.J. Chetty, B. Curran, J.E. Cygler, J.J. DeMarco, G. Ezzell, B.A. Faddegon, I. Kawrakow, P.J. Keall, H. Liu, C.M. Ma, D.W. Rogers, J. Seuntjens, D. Sheikh-Bagheri, J.V. Siebers, "Report of the AAPM Task Group No. 105: Issues associated with clinical implementation of Monte Carlo-based photon and electron external beam treatment planning," *Med Phys* **34**, 4818-4853 (2007).
- 32 M.J. Rivard, L. Beaulieu, F. Mourtada, "Enhancements to commissioning techniques and quality assurance of brachytherapy treatment planning systems that use model-based dose calculation algorithms," *Med Phys* **37**, 2645-2658 (2010).
- 33 G. Landry, B. Reniers, J.-P. Pignol, L. Beaulieu, F. Verhaegen, "The difference of scoring dose to water or tissues in Monte Carlo dose calculations for low energy brachytherapy photon sources," *Med Phys* **38**, 1526-1533 (2011).
- 34 A. Carlsson Tedgren, G.A. Carlsson, "Specification of absorbed dose to water using model-based dose calculation algorithms for treatment planning in brachytherapy," *Phys Med Biol* **58**, 2561-2579 (2013).
- 35 H.H. Liu, P. Keall, W.R. Hendee, "Dm rather than Dw should be used in Monte Carlo treatment planning," *Med Phys* **29**, 922-924 (2002).
- 36 R.M. Thomson, A.C. Tedgren, J.F. Williamson, "On the biological basis for competing macroscopic dose descriptors for kilovoltage dosimetry: cellular dosimetry for brachytherapy and diagnostic radiology," *Phys Med Biol* **58**, 1123-1150 (2013).
- 37 L. Lindborg, M. Hultqvist, A. Carlsson Tedgren, H. Nikjoo, "Lineal energy and radiation quality in radiation therapy: model calculations and comparison with experiment," *Phys Med Biol* **58**, 3089-3105 (2013).
- 38 S.A. Enger, A. Ahnesjo, F. Verhaegen, L. Beaulieu, "Dose to tissue medium or water cavities as surrogate for the dose to cell nuclei at brachytherapy photon energies," *Phys Med Biol* **57**, 4489-4500 (2012).
- 39 M.J. Berger, J.H. Hubbell, S.M. Seltzer, J. Chang, J.S. Coursey, R. Sukumar, D.S. Zucker, "XCOM: Photon Cross Section Database (version 1.3)," (NIST, Gaithersburg, MD, 2005).

- 40 M.J. Berger, Coursey, J.S., Zucker, M.A., and Chang, J, "ESTAR, PSTAR, and
ASTAR: Computer Programs for Calculating Stopping-Power and Range Tables for
Electrons, Protons, and Helium Ions (version 1.2.3)," (National Institute of Standards
and Technology, Gaithersburg, MD., 2005).
- 41 G.P. Fonseca, R.A. Rubo, R.A. Minamisawa, G.R. dos Santos, P.C. Antunes, H.
Yoriyaz, "Determination of transit dose profile for a (192)Ir HDR source," *Med Phys*
40, 051717 (2013).
- 42 A. Palmer, B. Mzenda, "Performance assessment of the BEBIG MultiSource high
dose rate brachytherapy treatment unit," *Phys Med Biol* 54, 7417-7434 (2009).
- 43 J.B. Wojcicka, R. Yankelevich, F. Trichter, D.P. Fontenla, "Comparison of the transit
dose components and source kinematics of three high dose rate afterloading systems,"
Med Dosim 24, 61-65 (1999).
- 44 T.P. Wong, W. Fernando, P.N. Johnston, I.F. Bubb, "Transit dose of an Ir-192 high
dose rate brachytherapy stepping source," *Phys Med Biol* 46, 323-331 (2001).
- 45 N. Sahoo, "Measurement of transit time of a remote after-loading high dose rate
brachytherapy source," *Med Phys* 28, 1786-1790 (2001).
- 46 R.A. Minamisawa, R.A. Rubo, R.M. Seraide, J.R. Rocha, A. Almeida, "Direct
measurement of instantaneous source speed for a HDR brachytherapy unit using an
optical fiber based detector," *Med Phys* 37, 5407-5411 (2010).
- 47 K.T. Bastin, M.B. Podgorsak, B.R. Thomadsen, "The transit dose component of high
dose rate brachytherapy: direct measurements and clinical implications," *Int J Radiat
Oncol Biol Phys* 26, 695-702 (1993).
- 48 R. Das, J. Venselaar, "Standard Technology in Brachytherapy," in *Comprehensive
Brachytherapy: Physical and Clinical Aspects*, edited by J. Venselaar, A.S. Meigooni,
D. Baltas, P.J. Hoskin (CRC Press, 2012).
- 49 T.E. Booth, J.T. Goorley, A. Sood, F.B. Brown, H.G. Hughes, J.E. Sweezy, J.S. Bull,
R. Martz, A. Zukaitis, R.A. Forster, R.E. Prael, R.C. Little, M.C. White, M.B. Lee, H.
Trellue, S.M. Girard, "MCNP—A General Monte Carlo N-Particle Transport Code -
Volume I: Overview and Theory," (2003).
- 50 G.P. Fonseca, G. Landry, B. Reniers, A. Hoffmann, R.A. Rubo, P.C.G. Antunes, H.
Yoriyaz, F. Verhaegen, "The contribution from transit dose for 192 Ir HDR
brachytherapy treatments," *Physics in Medicine and Biology* 59, 1831-1834 (2014).
- 51 G.P. Fonseca, R.S. Viana, M. Podesta, R.A. Rubo, C.P. de Sales, B. Reniers, H.
Yoriyaz, F. Verhaegen, "HDR (192)Ir source speed measurements using a high speed
video camera," *Med Phys* 42, 412 (2015).
- 52 H. Becquerel, P. Curie, "Action physiologique des rayons du radium," *Vol. C.R. T 132*
(Académie des Sciences, Paris, 1901), pp. 1289–1291.
- 53 D. H, P. Bloch, "Note sur le traitement du lupus érythémateux par des applications de
radium," *Ann. Dermatol. Syphil* 2, 986-988 (1901).
- 54 M. Cleaves, "Radium: with a preliminary note on radium rays in the treatment of
cancer," *Med Rec* 64, 601-606 (1903).
- 55 R. Abbe, "Notes on the physiologic and therapeutic action of radium," *Wash. Med
Ann* 2 (1904).
- 56 J.W. Morton, "Treatment of cancer by the x-ray, with remarks on the use of radium,"
Int J Surg 14, 289-300 (1903).
- 57 R. Barakat, M.E. Randall, M. Markman, *Principles and Practice of Gynecologic
Oncology*, 5 ed. (Lippincott Williams & Wilkins, Philadelphia, 2009).
- 58 R. Abbe, "The use of radium in malignant disease," *Lancet* 2, 524-527 (1913).
- 59 U.K. Henschke, "A technique for permanent implantation of radioisotopes,"
Radiology 68, 256 (1957).

- 60 U.K. Henschke, "Interstitial implantation in the treatment of primary bronchogenic carcinoma," *A. J. Roentgenol.* **79**, 981-987 (1958).
- 61 M. Brucer, "Therapeutic potentialities of radioisotopes," *Merck Rep* **61**, 9-15 (1952).
- 62 J.F. Williamson, "Brachytherapy technology and physics practice since 1950: a half-century of progress," *Phys Med Biol* **51**, R303-325 (2006).
- 63 T. Palmqvist, A. Dybdahl Wanderas, A.B. Langeland Marthinsen, M. Sundset, I. Langdal, S. Danielsen, I. Toma-Dasu, "Dosimetric evaluation of manually and inversely optimized treatment planning for high dose rate brachytherapy of cervical cancer," *Acta Oncol* **53**, 1012-1018 (2014).
- 64 D.Y. Han, M.J. Webster, D.J. Scanderbeg, C. Yashar, D. Choi, B. Song, S. Devic, A. Ravi, W.Y. Song, "Direction-modulated brachytherapy for high-dose-rate treatment of cervical cancer. I: theoretical design," *Int J Radiat Oncol Biol Phys* **89**, 666-673 (2014).
- 65 I. Thibault, M.C. Lavallee, S. Aubin, N. Laflamme, E. Vigneault, "Inverse-planned gynecologic high-dose-rate interstitial brachytherapy: clinical outcomes and dose-volume histogram analysis," *Brachytherapy* **11**, 181-191 (2012).
- 66 B.R. Thomadsen, J.F. Williamson, M.J. Rivard, A.S. Meigooni, "Anniversary paper: past and current issues, and trends in brachytherapy physics," *Med Phys* **35**, 4708-4723 (2008).
- 67 D.C. Medich, M.A. Tries, J.J. Munro, 2nd, "Monte Carlo characterization of an ytterbium-169 high dose rate brachytherapy source with analysis of statistical uncertainty," *Med Phys* **33**, 163-172 (2006).
- 68 R. Guerrero, J.F. Almansa, J. Torres, A.M. Lallena, "Dosimetric characterization of the (60)Co BEBIG Co0.A86 high dose rate brachytherapy source using PENELOPE," *Phys Med* **30**, 960-967 (2014).
- 69 W.J. Meredith, "Radiotherapeutic physics: V. Dosage control in interstitial gamma-ray therapy," *Br. J. Radiol* **24**, 380-384 (1951).
- 70 N. Suntharalingam, E.B. Podgorska, H. T'olli, "Brachytherapy: Physical and Clinical Aspects," (International Atomic Energy Agency, Vienna) (2005).
- 71 E.H. Quimby, "The calculation of dosage in interstitial radium therapy," *Am. J. Roentgenol., Radium Ther. Nucl. Med* **70**, 739-740 (1953).
- 72 J.F. Williamson, "The Sievert integral revisited: evaluation and extension to 125I, 169Yb, and 192Ir brachytherapy sources," *Int J Radiat Oncol Biol Phys* **36**, 1239-1250 (1996).
- 73 J.F. Williamson, "Monte Carlo-based dose-rate tables for the Amersham CDCS.J and 3M model 6500 137Cs tubes," *Int J Radiat Oncol Biol Phys* **41**, 959-970 (1998).
- 74 W.M. Butler, W.S. Bice, Jr., L.A. DeWerd, J.M. Hevezi, M.S. Huq, G.S. Ibbott, J.R. Palta, M.J. Rivard, J.P. Seuntjens, B.R. Thomadsen, "Third-party brachytherapy source calibrations and physicist responsibilities: report of the AAPM Low Energy Brachytherapy Source Calibration Working Group," *Med Phys* **35**, 3860-3865 (2008).
- 75 R.E.P. Taylor, G. Yegin, D.W.O. Rogers, "Benchmarking BrachyDose: Voxel based EGSnrc Monte Carlo calculations of TG-43 dosimetry parameters," *Med Phys* **34**, 445-457 (2007).
- 76 R.E. Taylor, D.W. Rogers, "EGSnrc Monte Carlo calculated dosimetry parameters for 192Ir and 169Yb brachytherapy sources," *Med Phys* **35**, 4933-4944 (2008).
- 77 G.M. Daskalov, E. Loffler, J.F. Williamson, "Monte Carlo-aided dosimetry of a new high dose-rate brachytherapy source," *Med Phys* **25**, 2200-2208 (1998).
- 78 K.R. Russell, A.K. Tedgren, A. Ahnesjo, "Brachytherapy source characterization for improved dose calculations using primary and scatter dose separation," *Med Phys* **32**, 2739-2752 (2005).

- 79 Y. Yu, L.L. Anderson, Z. Li, D.E. Mellenberg, R. Nath, M.C. Schell, F.M. Waterman, A. Wu, J.C. Blasko, "Permanent prostate seed implant brachytherapy: report of the American Association of Physicists in Medicine Task Group No. 64," *Med Phys* **26**, 2054-2076 (1999).
- 80 H.H. Holm, N. Juul, J.F. Pedersen, H. Hansen, I. Stroyer, "Transperineal 125iodine seed implantation in prostatic cancer guided by transrectal ultrasonography," *J Urol* **130**, 283-286 (1983).
- 81 M. Riccabona, J. Hammer, A. Schorn, "[Percutaneous, perineal, ultrasound-controlled implantation of 125iodine in prostatic cancer: technics, report of initial experiences and comparison with the retropubic method of implantation]," *Urologe A* **26**, 15-21 (1987).
- 82 J.C. Blasko, P.D. Grimm, H. Ragde, "Brachytherapy and Organ Preservation in the Management of Carcinoma of the Prostate," *Semin Radiat Oncol* **3**, 240-249 (1993).
- 83 H. Jiang, J. Seco, H. Paganetti, "Effects of Hounsfield number conversion on CT based proton Monte Carlo dose calculations," *Med Phys* **34**, 1439-1449 (2007).
- 84 J.F. Williamson, S. Li, S. Devic, B.R. Whiting, F.A. Lerma, "On two-parameter models of photon cross sections: Application to dual-energy CT imaging," *Med Phys* **33**, 4115-4129 (2006).
- 85 G. Landry, B. Reniers, P.V. Granton, B. van Rooijen, L. Beaulieu, J.E. Wildberger, F. Verhaegen, "Extracting atomic numbers and electron densities from a dual source dual energy CT scanner: experiments and a simulation model," *Radiother Oncol* **100**, 375-379 (2011).
- 86 G. Landry, P.V. Granton, B. Reniers, M.C. Ollers, L. Beaulieu, J.E. Wildberger, F. Verhaegen, "Simulation study on potential accuracy gains from dual energy CT tissue segmentation for low-energy brachytherapy Monte Carlo dose calculations," *Phys Med Biol* **56**, 6257-6278 (2011).
- 87 D. Fontanarosa, S. Pesente, F. Pascoli, D. Ermacora, I.A. Rumeileh, F. Verhaegen, "A speed of sound aberration correction algorithm for curvilinear ultrasound transducers in ultrasound-based image-guided radiotherapy," *Phys Med Biol* **58**, 1341-1360 (2013).
- 88 M. Bazalova, L. Beaulieu, S. Palefsky, F. Verhaegen, "Correction of CT artifacts and its influence on Monte Carlo dose calculations," *Med Phys* **34**, 2119-2132 (2007).
- 89 C. Xu, F. Verhaegen, D. Laurendeau, S.A. Enger, L. Beaulieu, "An algorithm for efficient metal artifact reductions in permanent seed," *Med Phys* **38**, 47-56 (2011).
- 90 M. Yazdi, L. Gingras, L. Beaulieu, "An adaptive approach to metal artifact reduction in helical computed tomography for radiation therapy treatment planning: experimental and clinical studies," *Int J Radiat Oncol Biol Phys* **62**, 1224-1231 (2005).
- 91 D. Xia, J.C. Roeske, L. Yu, C.A. Pelizzari, A.J. Mundt, X. Pan, "A hybrid approach to reducing computed tomography metal artifacts in intracavitary brachytherapy," *Brachytherapy* **4**, 18-23 (2005).
- 92 M. Gaudreault, B. Reniers, G. Landry, F. Verhaegen, L. Beaulieu, "Dose perturbation due to catheter materials in high-dose-rate interstitial (192)Ir brachytherapy," *Brachytherapy* **13**, 627-631 (2014).
- 93 K.A. Gifford, J.L. Horton, Jr., E.F. Jackson, T.R. Steger, 3rd, M.P. Heard, F. Mourtada, A.A. Lawyer, G.S. Ibbott, "Comparison of Monte Carlo calculations around a Fletcher Suit Delclos ovoid with radiochromic film and normoxic polymer gel dosimetry," *Med Phys* **32**, 2288-2294 (2005).
- 94 Z. Tian, Y.J. Graves, X. Jia, S.B. Jiang, "Automatic commissioning of a GPU-based Monte Carlo radiation dose calculation code for photon radiotherapy," *Phys Med Biol* **59**, 6467-6486 (2014).

- 95 Y.S. Yeom, J.H. Jeong, M.C. Han, C.H. Kim, "Tetrahedral-mesh-based computational human phantom for fast Monte Carlo dose calculations," *Phys Med Biol* **59**, 3173-3185 (2014).
- 96 A.A. Nunn, S.D. Davis, J.A. Micka, L.A. DeWerd, "LiF:Mg,Ti TLD response as a function of photon energy for moderately filtered x-ray spectra in the range of 20-250 kVp relative to ^{60}Co ," *Med Phys* **35**, 1859-1869 (2008).
- 97 R.S. Viana, G.A. Agasthya, H. Yoriyaz, A.J. Kapadia, "3D element imaging using NSECT for the detection of renal cancer: a simulation study in MCNP," *Phys Med Biol* **58**, 5867-5883 (2013).
- 98 A.E. Nahum, "Water/air mass stopping power ratios for megavoltage photon and electron beams," *Physics in Medicine and Biology* **23**, 24 (1978).
- 99 A.E. Nahum, M. Kristensen, "Calculated response and wall correction factors for ionization chambers exposed to ^{60}Co gamma rays," *Med Phys* **9**, 925-927 (1982).
- 100 D.W.O. Rogers, "How accurately can EGS4/PRESTA calculate ion-chamber response?," *Med Phys* **20**, 319-323 (1993).
- 101 D.W. Rogers, "Fifty years of Monte Carlo simulations for medical physics," *Phys Med Biol* **51**, R287-301 (2006).
- 102 J. Baró, J. Sempau, J.M. Fernández-Varea, F. Salvat, "PENELOPE: An algorithm for Monte Carlo simulation of the penetration and energy loss of electrons and positrons in matter," *Nuclear Instruments and Methods in Physics Research Section B: Beam Interactions with Materials and Atoms* **100**, 31-46 (1995).
- 103 S. Jan, G. Santin, D. Strul, S. Staelens, K. Assie, D. Autret, S. Avner, R. Barbier, M. Bardies, P.M. Bloomfield, D. Brasse, V. Breton, P. Bruyndonckx, I. Buvat, A.F. Chatziioannou, Y. Choi, Y.H. Chung, C. Comtat, D. Donnarieix, L. Ferrer, S.J. Glick, C.J. Groiselle, D. Guez, P.F. Honore, S. Kerhoas-Cavata, A.S. Kirov, V. Kohli, M. Koole, M. Krieguer, D.J. van der Laan, F. Lamare, G. Largeron, C. Lartzien, D. Lazaro, M.C. Maas, L. Maigne, F. Mayet, F. Melot, C. Merheb, E. Pennacchio, J. Perez, U. Pietrzyk, F.R. Rannou, M. Rey, D.R. Schaart, C.R. Schmidlein, L. Simon, T.Y. Song, J.M. Vieira, D. Visvikis, R. Van de Walle, E. Wieers, C. Morel, "GATE: a simulation toolkit for PET and SPECT," *Phys Med Biol* **49**, 4543-4561 (2004).
- 104 V. Krishaswamy, "Calculation of the dose distribution about californium-252 needles in tissue," *Radiology* **98**, 155-160 (1971).
- 105 L.L. Meisberger, R.J. Keller, R.J. Shalek, "The effective attenuation in water of the gamma rays of gold 198, iridium 192, cesium 137, radium 226, and cobalt 60," *Radiology* **90**, 953-957 (1968).
- 106 A. Kirov, J.F. Williamson, A.S. Meigooni, Y. Zhu, "TLD, diode and Monte Carlo dosimetry of an ^{192}Ir source for high dose-rate brachytherapy," *Phys Med Biol* **40**, 2015-2036 (1995).
- 107 R.K. Valicenti, A.S. Kirov, A.S. Meigooni, V. Mishra, R.K. Das, J.F. Williamson, "Experimental validation of Monte Carlo dose calculations about a high-intensity ^{192}Ir source for pulsed dose-rate brachytherapy," *Med Phys* **22**, 821-829 (1995).
- 108 J.F. Williamson, "Comparison of measured and calculated dose rates in water near I-125 and Ir-192 seeds," *Med Phys* **18**, 776-786 (1991).
- 109 J.F. Williamson, H. Perera, Z. Li, W.R. Lutz, "Comparison of calculated and measured heterogeneity correction factors for ^{125}I , ^{137}Cs , and ^{192}Ir brachytherapy sources near localized heterogeneities," *Med Phys* **20**, 209-222 (1993).
- 110 H. Perera, J.F. Williamson, Z. Li, V. Mishra, A.S. Meigooni, "Dosimetric characteristics, air-kerma strength calibration and verification of Monte Carlo simulation for a new Ytterbium-169 brachytherapy source," *Int J Radiat Oncol Biol Phys* **28**, 953-970 (1994).

- 111 R.K. Das, D. Keleti, Y. Zhu, A.S. Kirov, A.S. Meigooni, J.F. Williamson, "Validation of Monte Carlo dose calculations near 125I sources in the presence of bounded heterogeneities," *Int J Radiat Oncol Biol Phys* **38**, 843-853 (1997).
- 112 P. Papagiannis, E. Pantelis, P. Karaiskos, "Current state of the art brachytherapy treatment planning dosimetry algorithms," *Br J Radiol* **87**, 20140163 (2014).
- 113 J.T. Goorley, M.R. James, T.E. Booth, F.B. Brown, J.S. Bull, L.J. Cox, J.W.J. Durkee, J.S. Elson, M.L. Fensin, R.A.I. Forster, J.S. Hendricks, H.G.I. Hughes, R.C. Johns, B.C. Kiedrowski, R. Martz, R. L., S.G. Mashnik, G.W. McKinney, D.B. Pelowitz, R.E. Prael, J.E. Sweezy, L.S. Waters, T. Wilcox, A.J. Zukaitis, "Initial MCNP6 Release Overview - MCNP6 version 1.0," (2013).
- 114 ICRU Radiation Quantities and Units, Report 33 of the International Commission on Radiation Units and Measurements (Bethesda, MD) (1980).
- 115 C.M. Baglin, "Nuclear Data Sheets for A = 192," *Nuclear Data Sheets* **113**, 1871-2111 (2012).
- 116 C.G.a.J.-F. Remacle, "Gmsh: a three-dimensional finite element mesh generator with built-in pre- and post-processing facilities," *International Journal for Numerical Methods in Engineering* **79**, 1309-1331 (2009).
- 117 R.L. Martz, "The MCNP6 Book On Unstructured Mesh Geometry: User's Guide," (2012).
- 118 F. Ballester, D. Granero, J. Perez-Calatayud, C.S. Melhus, M.J. Rivard, "Evaluation of high-energy brachytherapy source electronic disequilibrium and dose from emitted electrons," *Med Phys* **36**, 4250-4256 (2009).
- 119 R. Wang, X.A. Li, "Dose characterization in the near-source region for two high dose rate brachytherapy sources," *Med Phys* **29**, 1678-1686 (2002).
- 120 M.J. Rivard, S.D. Davis, L.A. DeWerd, T.W. Rusch, S. Axelrod, "Calculated and measured brachytherapy dosimetry parameters in water for the Xofigo X-Ray Source: an electronic brachytherapy source," *Med Phys* **33**, 4020-4032 (2006).
- 121 J.F. Williamson, "Monte Carlo evaluation of kerma at a point for photon transport problems," *Med Phys* **14**, 567-576 (1987).
- 122 M.J. Berger, J.S. Coursey, M.A. Zucker and J. Chang, "ESTAR, PSTAR, and ASTAR: Computer Programs for Calculating Stopping-Power and Range Tables for Electrons, Protons, and Helium Ions," (Version 1.2.3) (Gaithersburg, MD: NIST) (2005).
- 123 ICRU "Stopping Powers for Electrons and Positrons," Report 37, (international Commission on Radiation units and Measurements, Bethesda, MD) (1984).
- 124 S.A. Enger, G. Landry, M. D'Amours, F. Verhaegen, L. Beaulieu, M. Asai, J. Perl, "Layered mass geometry: a novel technique to overlay seeds and applicators onto patient geometry in Geant4 brachytherapy simulations," *Phys Med Biol* **57**, 6269-6277 (2012).
- 125 C.M. Poole, I. Cornelius, J.V. Trapp, C.M. Langton, "A CAD interface for GEANT4," *Australasian Physical & Engineering Sciences in Medicine* **35**, 329-334 (2012).
- 126 C.M. Poole, I. Cornelius, J.V. Trapp, C.M. Langton, "Fast Tessellated Solid Navigation in GEANT4," *Nuclear Science, IEEE Transactions on* **59**, 1695-1701 (2012).
- 127 V.O. Zilio, O.P. Joneja, Y. Popowski, A. Rosenfeld, R. Chawla, "Absolute depth-dose-rate measurements for an 192Ir HDR brachytherapy source in water using MOSFET detectors," *Med Phys* **33**, 1532-1539 (2006).
- 128 A. Fogliata, G. Nicolini, A. Clivio, E. Vanetti, L. Cozzi, "Dosimetric evaluation of Acuros XB Advanced Dose Calculation algorithm in heterogeneous media," *Radiation Oncology* **6**, 82 (2011).

- 129 ICRP, "Adult Reference Computational Phantoms. ICRP Publication 110," Ann. ICRP **39** (2) (2009).
- 130 J. Perez-Calatayud, D. Granero, F. Ballester, "Phantom size in brachytherapy source dosimetric studies," Med Phys **31**, 2075-2081 (2004).
- 131 D. Liu, E. Poon, M. Bazalova, B. Reniers, M. Evans, T. Rusch, F. Verhaegen, "Spectroscopic characterization of a novel electronic brachytherapy system," Phys Med Biol **53**, 61-75 (2008).
- 132 M.J. Rivard, S.D. Davis, L.A. DeWerd, T.W. Rusch, S. Axelrod, "Calculated and measured brachytherapy dosimetry parameters in water for the Xofigo Axxent X-Ray Source: an electronic brachytherapy source," Med Phys **33**, 4020-4032 (2006).
- 133 L. Petrokokkinos, K. Zourari, E. Pantelis, A. Moutsatsos, P. Karaiskos, L. Sakelliou, I. Seimenis, E. Georgiou, P. Papagiannis, "Dosimetric accuracy of a deterministic radiation transport based ¹⁹²Ir brachytherapy treatment planning system. Part II: Monte Carlo and experimental verification of a multiple source dwell position plan employing a shielded applicator," Med Phys **38**, 1981-1992 (2011).
- 134 D. Thain, T. Tannenbaum, M. Livny, "Distributed computing in practice: the Condor experience: Research Articles," Concurr. Comput. : Pract. Exper. **17**, 323-356 (2005).
- 135 G.P. Fonseca, B. Reniers, G. Landry, S. White, M. Bellezzo, P.C. Antunes, C.P. de Sales, E. Welteman, H. Yoriyaz, F. Verhaegen, "A medical image-based graphical platform-Features, applications and relevance for brachytherapy," Brachytherapy (2014).
- 136 C.S. Calcina, A. de Almeida, J.R. Rocha, F.C. Abrego, O. Baffa, "Ir-192 HDR transit dose and radial dose function determination using alanine/EPR dosimetry," Phys Med Biol **50**, 1109-1117 (2005).
- 137 "Planning system manual, ONCENTRA®MasterPlan v3.3 Physics and Algorithms," Report No. 192.718ENG-04.
- 138 ICRP, "Report on the Task Group on Reference Man," Ann. ICRP **23** (1975)
- 139 T. Goorley, "MCNP5 Tally Enhancements for Lattices," Los Alamos, NM: National Laboratory (2004).
- 140 B. Reniers, D. Liu, T. Rusch, F. Verhaegen, "Calculation of relative biological effectiveness of a low-energy electronic brachytherapy source," Phys Med Biol **53**, 7125-7135 (2008).
- 141 A.C. Tedgren, A. Hedman, J.E. Grindborg, G.A. Carlsson, "Response of LiF:Mg,Ti thermoluminescent dosimeters at photon energies relevant to the dosimetry of brachytherapy (<1 MeV)," Med Phys **38**, 5539-5550 (2011).
- 142 J.L.G. Massillon, A. Cabrera-Santiago, R. Minniti, M. O'Brien, C.G. Soares, "Influence of phantom materials on the energy dependence of LiF:Mg,Ti thermoluminescent dosimeters exposed to 20-300 kV narrow x-ray spectra, ¹³⁷Cs and ⁶⁰Co photons," Phys Med Biol **59**, 4149-4166 (2014).
- 143 C. Ehringfeld, S. Schmid, K. Poljanc, C. Kirisits, H. Aiginger, D. Georg, "Application of commercial MOSFET detectors for in vivo dosimetry in the therapeutic x-ray range from 80 kV to 250 kV," Phys Med Biol **50**, 289-303 (2005).
- 144 B. Reniers, G. Landry, R. Eichner, A. Hallil, F. Verhaegen, "In vivo dosimetry for gynaecological brachytherapy using a novel position sensitive radiation detector: feasibility study," Med Phys **39**, 1925-1935 (2012).
- 145 P.V. Houdek, J.G. Schwade, X. Wu, V. Pisciotta, J.A. Fiedler, C.F. Serago, A.M. Markoe, A.A. Abitbol, A.A. Lewin, P.G. Braunschweiger, et al., "Dose determination in high dose-rate brachytherapy," Int J Radiat Oncol Biol Phys **24**, 795-801 (1992).
- 146 J.F. Williamson, G.A. Ezzell, A. Olch, B.R. Tomadsen, "Quality Assurance for High Dose Rate Brachytherapy," in *High Dose Rate Brachytherapy: A Textbook*, edited by S. Nag (Futura Pub Co), pp. 147-212 (1994)

- ¹⁴⁷ Y.S. Yeom, J.H. Jeong, M.C. Han, C.H. Kim, "Tetrahedral-mesh-based computational human phantom for fast Monte Carlo dose calculations," *Physics in Medicine and Biology* **59**, 3173 (2014).

**VALORIZATION
ADDENDUM**

11 VALORIZATION ADDENDUM

Brachytherapy has been under continuous development for more than a century now, improved outcomes result from increased accuracy in radiation delivery. Currently, the conventional water based dose formalism, TG-43U1, is being replaced with more accurate models. However, important technical challenges need to be overcome before a definitive clinical implementation of the recently developed technologies can be realised. Some of these aspects were evaluated in this thesis, aiming to provide knowledge and resources to move towards more accurate treatment plans and radiation dose delivery.

This study was performed in two countries, Brazil and the Netherlands, in collaboration with hospitals from Sweden and Belgium. It demonstrates an international interest in brachytherapy and the potential application of the acquired knowledge.

11.1 Innovation

This thesis aims to improve brachytherapy treatment and can be divided into four specific novel subjects.

11.1.1 Model Based Dose Calculation Algorithm

AMIGOBBrachy (A Medical Image-based Graphical platfOrm - Brachytherapy module) is software developed to create an efficient and powerful user-friendly graphical interface, needed to integrate clinical treatment plans with MC simulations. It does this by providing the main resources required to process and edit images, import and edit treatment plans, as well as set MC simulation parameters. It is the first software to provide all these functionalities combined with the capability to import and verify treatment plans created with commercial TPS (Treatment Planning System) through MC calculations. In addition, AMIGOBBrachy can account for source movement, calculate different dose reporting quantities, mean energy and photon energy spectrum. All of these features are not currently available in typical clinical practice.

11.1.2 CAD-Mesh geometries

The modelling of complex brachytherapy applicators can be suboptimal when using voxel based geometry, due to the sub-voxel dimensions of specific components. In addition,

applicator modelling using constructive solid geometry can be tedious, and may not allow complete fidelity or may be highly impractical, as is the case for deformable balloon applicators employed in accelerated partial breast irradiation (APBI).

Some modelling limitations can be avoided with CAD-Mesh geometries that can be imported by recent versions of general purpose MC codes. This thesis is the first study to evaluate CAD-Mesh models of brachytherapy applicators through MC simulations. Moreover, it is the most accurate method to model deformable applicators (APBI balloon applicator – item 4.3) available thus far.

11.1.3 Dose specification

Dose reporting quantities are especially relevant since the transition from the TG-43U1 formalism to more accurate dose calculation algorithms will make both $D_{m,m}$ and $D_{w,m}$ quantities available in typical clinical practice very soon. Differences between dose reporting in terms of $D_{m,m}$ and $D_{w,m}$ have been discussed in the literature with arguments in favor and against both quantities. However, this is the first study to show how differences in the photon energy spectrum inside of the patient can affect the relation between $D_{m,m}$ and $D_{w,m}$ for different tissues. This study can substantially contribute to future judgements regarding which quantity should be adopted as the standard in clinical practice.

11.1.4 Transit dose

The dose component due to source movement inside of the patient is, surprisingly, not well known. It is dependent upon the source speed profile which is not well established, with reported differences of up to a factor 10 (depending on the measurement methodology). Such large differences in the speed values lead to either negligible or highly significant transit doses, which was assessed for clinical cases for the first time in this thesis. These results indicate the importance to perform more accurate source speed profile measurements, which were conducted in this study for one afterloader model. Speed profiles were obtained using a high speed video camera capable of recording up to 960 fps leading to the most accurate source speed values available to date.

11.2 Clinical relevance

Patient safety is a priority for medical treatments with hospitals and research centers working exhaustively to improve the actual treatment conditions. However, brachytherapy is particularly prone to treatment errors, due to the lack of integrated imaging in the treatment room, coupled with the high dose gradients employed in the vicinity of radiosensitive healthy tissues and due to simplified dose calculation models. Furthermore, treatment plans obtained from commercial TPS are not commonly verified using alternative methods such as Monte Carlo. There is both a significant risk to underdose the tumor, and to overdose the healthy tissues.

The software developed, AMIGOBrachy (items 4.2 and 5.1), has a user friendly interface that can be readily adopted in clinical practice as an auxiliary dose calculation engine. It would provide an independent validation method with the possibility to account for applicators, tissues composition and densities. The clinical cases evaluated with AMIGOBrachy/MCNP6 show under and overdosing compared to TG-43U1 (item 4.2.4). The results obtained prompted the replacement of hollow cylindrical applicators at one hospital, due to a 5% target overdose concern in gynaecological cases. It was the first direct clinical application of this thesis and illustrates how treatment accuracy can be improved, sometimes, by adopting simple measures.

Finally, we provide a novel method to simulate deformable brachytherapy applicators (APBI balloon applicator – item 4.3) that cannot be modelled with conventional analytical geometry. The CAD-Mesh feature is also an alternative to model rigid brachytherapy applicators and may be a suitable option when the applicator model is provided by the manufacturer. Although the effect of the applicator can be significant (item 5.2), it is currently not taken into account by TPS based on the TG-43U1 formalism.

11.3 Societal relevance

The scientific findings discussed in this thesis can significantly improve dose calculation accuracy and provide relevant information that can be related to RBE effects and patient outcome. Therefore, in the short term, treatment plans can be more accurate by accounting for applicators, tissue composition, densities and other treatment complexities. In the longer term, different dose reporting quantities and mean energy or the energy spectrum can be assessed and related to patient outcomes once more data on these quantities becomes available.

Brachytherapy is widely employed worldwide due to good outcomes. However, the technology currently available can move the current standards towards even better outcomes. If translated into clinical practice, the developments achieved in this thesis would provide a significant contribution to this process.

Significant efforts were made to incorporate scientific advances into AMIGOBrachy so that they are available to the radiotherapy community. The study of different dose reporting quantities is an example of such an effort. Additionally, a physical discussion with quantitative values for dose reporting quantities were provided for a clinical case, the capability to score these quantities are part of AMIGOBrachy and can be used for any clinical case.

11.4 Commercial relevance

AMIGOBrachy may become part of a commercial product in the near future which would lead to revenue in the form of royalties, professional support service and training courses.

